Quantitative evaluation for functions and appearance of human skin tissue using reflectance spectroscopy

（反射分光法を用いた皮膚の機能と見え方の定量評価に関する研究）

2014.9

Graduate School of Bio-applications & Systems Engineering

Tokyo University of Agriculture & Technology

東京農工大学大学院

生物システム応用科学府

生物システム応用科学専攻

Kenichiro Yoshida

吉田　健一郎

Table of Contents

1. Introductory remarks

1.1. Researches on inspection of skin with visible light

Changes in functions and configuration of living tissues by pathological changes are related to optical properties of tissues. Optical methodology, especially with visible reflected light, has the characteristic of non-invasive nature. Therefore, many studies are conducted for evaluations of optical properties of tissues *in vivo* with visible light. Especially, in the case of skin, the observation is easier than that of other tissues. In the field of dermatology, ocular inspection is recognized as an important diagnostic method. However, ocular inspection depends on the skill and experience of individuals, and quantitative. These problems can be resolved by quantifying optical properties. With the quantitative measurement and analysis of reflectance spectrum, even slight difference is distinguishable, which is sometimes not detectable with human eye. Therefore, reflectance spectroscopy has been gathered great attention in the field of skin diagnosis.

The optical characteristic of skin is useful not only for the estimation of internal states, but for the estimation of appearance of human skin. Skin is easy to be observed, and comes into sight regardless of whether one likes it or not. Therefore, the optical properties of skin is important in terms of aesthetic point of view also. In fact, some

kind of skin diseases pose serious problems in appearance rather than in function. The understanding of skin optics is also important in realizing natural appearance of prosthesis. Moreover, the quantification of skin appearance is important in the field of cosmetics, too. In the case of computer graphics, the quantification of skin appearance is effective in achieving a realistic portrayal.

The reflected light from skin consists of components which reflect at skin surface (surface reflection) and which penetrate into skin and re-emerge after scattering and absorption (internal reflection) (Fig. 1-1). The angular distribution of intensity of surface reflection depends on surface profile and refractive index of skin. In general, the reflectance of surface reflection is independent of wavelength in the range of visible light, and the surface reflection characterizes the texture such as gloss or matte in appearance. The relation between surface reflection and the condition of superficial layer of skin can be connected intuitively. Typical causes that influence the surface reflection are sebum secretion and desquamation, which are obvious reasons that affect the appearance. However, it is difficult to correlate the surface reflection and the inner conditions.

On the other hand, internal reflection is strongly affected by the optical properties of skin internal tissue. The penetrated light will be scattered and attenuated according to the scattering and absorption coefficients of skin. The internal reflection depends on wavelength, because those coefficients depends on wavelength. Especially, the chromophores in skin such as melanin, oxygenated hemoglobin, and deoxygenated hemoglobin have particular absorbance spectra, which characterize the skin appearance. Moreover, internal reflection characterizes not only skin color but also skin translucency, which is indispensable for natural-looking of skin. Translucency is the degree of lateral

spread of re-emerged light, which is higher-level characteristics of materials. The translucency has a gradating effect on surface asperity and color unevenness. The translucency is expressed with point spread function (PSF).

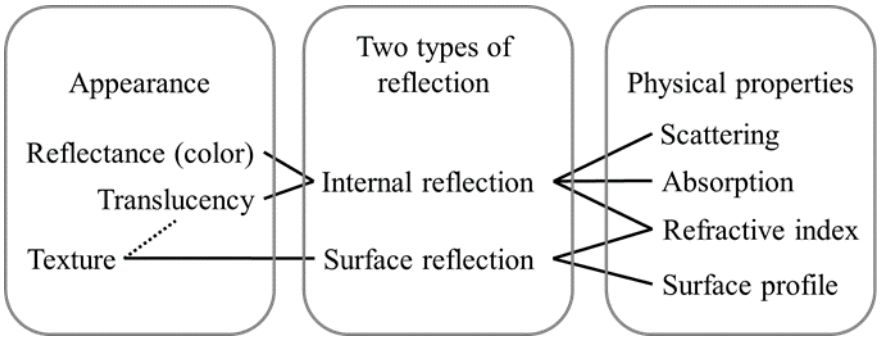

Fig. 1-1 Overview of the relationships between physical properties and appearance in reflection.

In what follows, the historical background of skin model for light reflection and chromophore estimation in skin, then the background of the studies in the dissertation are described.

1.1.1. Background of skin model for light reflection

For the quantitative evaluation of function, configuration and appearance of skin, the light propagation in skin must be modeled mathematically. The quantitative distribution of light intensity in scattering media can be described from the solution of Chandrasekhar's radiative transfer equation [1] as:

$$\frac{dI(\mathbf{r},\mathbf{s})}{ds} = -(\mu_a + \mu_s)I(\mathbf{r},\mathbf{s}) + \frac{\mu_a + \mu_s}{4\pi}\int_{4\pi} p(\mathbf{s},\mathbf{s}')I(\mathbf{r},\mathbf{s}')d\Omega', \tag{1-1}$$

where $I(\mathbf{r},\mathbf{s})$ is the intensity per unit solid angle at target location **r** in the direction **s** (**s** is the directional unit vector), μ_a and μ_s are the absorption coefficient and scattering

coefficient of medium, respectively. $p(\mathbf{s},\mathbf{s}')$ is the scattering phase function, representing scattering contribution from the direction $\mathbf{s}$ to $\mathbf{s}'$, and $d\Omega'$ is the solid angle. The first term on the right-hand side of Eq. 1-1 represents the loss in $I(\mathbf{r},\mathbf{s})$ per unit length in direction $\mathbf{s}$ due to absorption and scattering. The second term describes the gain in $I(\mathbf{r},\mathbf{s})$ per unit length in direction $\mathbf{s}$ due to scattering from other scattered light $I(\mathbf{r},\mathbf{s}')d\Omega'$ (i.e. light intensity confined in the elemental solid angle $d\Omega'$) from direction $\mathbf{s}'$.

This integro-differential equation expresses the rate of change in the intensity of a narrow incident light beam as a function of the optical properties of the medium involved. Although the radiative transfer theory gives a more adequate description of the distribution of light intensity in the optically turbid medium than does any other model, the general analytic solution is not known yet. However, there are some approximate analytical theories or numerical method in the following.

1. Beer-Lambert method (B-L method).

Originally, Beer-Lambert law (Sec. 2.2.2) is the law for the absorption of transmitted light in material without scattering. However, the law is applied to skin by simplifying the optical properties. Three layer model of epidermis, dermis and fat from upper layer is assumed. In the skin model, no scattering occurs in epidermis and dermis, and light is reflected at the interface between dermis and fat layer. Light is absorbed by melanin in epidermis and oxygenated and deoxygenated hemoglobin in dermis. The mathematical background is described in Sec. 2.3.1.

2. Modified Beer-Lambert method (modified B-L method).

With B-L method, estimation is easily achieved, however, the assumption of no

scattering in epidermis and dermis is differ substantially from the actual condition. To improve the problem, modified B-L method is developed. In the method, the light scattering in epidermis and dermis bring the changes in path length, which depend on the wavelength. The mathematical background is briefly described in Sec. 2.3.2.

3. Kubelka-Munk Theory.

The Kubelka-Munk theory has been widely used to determine the absorption and scattering coefficients of turbid media. This theory considers the two opposite fluxes, and can be employed when the scattering is significantly dominant over the absorption. This model is not accurate for forward-directed scattering and complicated geometric media such as a biological tissue because the isotropic scattering is assumed in this theory. The mathematical background is described in Sec. 2.3.3.

4. Diffusion approximation.

The diffusion approximation is obtained by considering the lowest-order approximation of the expansion in spherical harmonics of the radiative transfer equation. The diffusion approximation can be solved for homogeneous diffusing media for different boundary conditions such as infinitely extended medium, semi-infinite slab, finite slab, cylinder, and sphere. Theoretical studies of light propagation in the multiple scattering media based on the diffusion approximation have been published by Ishimaru [2] and Furustu [3]. The solutions obtained well describe photon propagation when the distance of a detector from the source is larger than about 10 transport mean free paths. The mathematical background is described in Sec. 2.3.4.

5. Adding doubling method

The basic concept is similar to Kubelka-Munk theory, however, the angular distribution is considered. The scattering and absorption properties and refractive index also

considered in the method. The details of the method is described in Chapter 6.

6. Monte Carlo method.

The Monte Carlo method provides a physical simulation of photon propagation in a scattering medium. The model assumes a non-deterministic, stochastic nature for high scattering and absorption of individual photon [4, 5]. By using a random number generating routine, the trajectories of emitted photons are chosen according to the statistical rules relevant for photon propagation through the medium. The trajectory of any emitted photon is followed until it exits from the scattering medium or it arrives at the detector. The Monte Carlo method allows a full-dimensional description of photon propagation and the actual scattering properties of tissue can be taken into account in the simulation. The parameters of a scattering coefficient, absorption coefficient, and scattering phase function are usually required in this method. The Monte Carlo method requires the long computational time for reliable results. The mathematical background is described in Sec. 2.3.5.

7. White Monte Carlo simulation.

White MCS (WMCS) is the method, in which reflectance of a model without absorption is calculated in advance, and that the reflectance of a model with absorption is derived from the pre-calculated data later. The method utilizes B-L law which indicate that the absorbance can be calculated if the path length is known. The method is described in details in Chapter 6.

Various techniques based on the light propagation model mentioned above have been studied and reported for measuring the optical properties of tissue *in vivo*. They are roughly classified into the time-resolved measuring technique and the spatially resolved

measuring technique. An outline of these types is briefly described in the following.

i. Time-Resolved Measuring Technique

When an ultrashort light pulse (a few picoseconds long) is incident on the scattering medium such as tissues, the received pulse backscattered from, or transmitted thorough the medium is a few seconds long. This temporal spreading of a light pulse is called the temporal spreading function (TPSF) [6], and depends on the optical properties of the medium. Therefore, the TPSF can be used to acquire the absorption and scattering coefficients of tissues. The use of a source emitting ultrashort pulse (picosecond, femtosecond) and an ultrafast detector such as a streak camera makes possible a direct measurement of the TPSF of the received pulse, which is known as the time-resolved measurement. Chance *et al.* [7] have reported the usefulness of the time-resolved technique for measuring the oxygenation state in the brain. Delpy *et al.* [8], Wilson *et al.* [9], and Nomura *et al.* [10] also utilized the time-resolved technique for measuring the optical properties of tissue. Patterson *et al.* [11] investigated the behavior of light in tissue by using the time-dependent diffusion approximation, whereas Hasegawa *et al.* [12] and Delpy *et al.* [8] employed the Monte Carlo method to analyze the time-resolved transmittance. Jacques [13] described light irradiance at various time intervals after impingement of femtosecond and picosecond light pulses using the Monte Carlo method.

ii. Spatially Resolved Measuring Technique

When a narrow photon beam is incident on the homogeneous scattering medium, the radial dependence of backscattered light depends on the optical properties of the medium. The spatially resolved technique is based on this radial dependence of the diffuse reflectance from the scattering medium. Different physical models have been used to determine expressions for the dependence of the diffuse reflectance on radial distance

from the incident point of light. Groenhuis *et al.* [14, 15] utilized the diffusion theory to derive the Green's function for photon fluence resulting from an isotropic point source at depth in a semi-infinite tissue as an infinite sum of modified Bessel functions. Shmitt *et al.* [16] extended this approach to express the radial reflectance from a multi-layered tissue such as the skin. Wilson *et al.* [17] proposed the use of the relative reflectance curve to determine the tissue optical properties. Farrell *et al.* [18] conducted the spatially resolved measurement of diffuse reflectance by using the multiple fiber-optic detectors in contact with the tissue surface at varying distances from the source. To avoid the pressure due to the contact probe, Bolt and ten Bosch [19, 20] introduced an alternative technique based on a remote, non-contact, video camera detector (video reflectometry). Jacques *et al.* [21] used this technique to measure the *ex vivo* tissue. Results obtained from the similar instrumentations have also been reported by Splinter *et al.* [22], Dogariu and Asakura [23], and Kienle *et al.* [24].

1.1.2. Background of skin chromophore estimation

Spectrophotometry over a broad range from visible to near-infrared wavelength is a common method to measure the reflectance spectra of tissue. Diffey *et al.* [25] have studied the vasoconstriction and erythema by using the numerical indices derived from the reflectance spectra of human skin. Dawson *et al.* [26] utilized the reflectance spectrophotometry for measurement of human skin tissue to characterize the spectral properties with B-L method. Harrison *et al.* [27] also measured the oxygen saturation and concentration of hemoglobin in the human skin tissue during the tuberculin reaction by using the numerical indices based on the reflectance spectra. Marchesini *et al.* [28, 29] and Wallace *et al.* [30] have studied the method to discriminate between benign and

malignant lesion in the skin tissue by using features of reflectance spectra of human skin. Shimada *et al.* [31-33] reported a method for predicting absorption spectra of skin tissue using the multiple regression analysis based on the modified B-L method.

Empirical method aided by MCS is the method that combine advantage of B-L method and MCS. As mentioned, B-L method does not take into account the effect of scattering. The modified B-L method partially take into account some effects of scattering, however, they are not fully considered. On the other hand, MCS consider almost all effects of scattering, however, the calculation time of MCS is very long which is crucial for some applications. In the empirical method aided by MCS, tentative chromophore concentrations are derived with Beer-Lambert method beforehand, and actual chromophore concentrations are calculated from the relation between the tentative and actual chromophore concentrations. The relationships are calculated with MCS in advance. This method is described in Chapter 3 where this method is the base of the study.

As the other spectral analysis, chemometrics have been studied for evaluating the chromophores in the skin tissue. Tsumura *et al.* [34] proposed a method using the independent component analysis of color images for visualizing spatial distributions of melanin and hemoglobin in the human skin.

1.1.3. Background of individual studies in the dissertation

Shading-derived artifacts in skin chromophore imaging (Chap. 3)

The concentrations of chromophores in skin provide important information for making a diagnosis, and images can provide additional information, such as the size of a lesion, that aid visual understanding. Multiple regression analysis based on the Beer-Lambert

(B-L) law [26] is a simple way to correlate the chromophore concentrations with the reflectance of skin. Although the implementation is easy, the model is quite different from actual conditions, and it leads to inconsistencies between the actual and the fitted spectrums [31, 35, 36].

In order to fully account for the effect of scattering in the estimation of chromophore concentrations, several methods have been considered; these include methods based on random work theory [37], Kubelka-Munk theory [38], a support vector machine [39], and an empirical method aided by a Monte Carlo simulation (MCS) [40, 41]. Although scattering effects are fully considered in these methods, the methods are susceptible to shading-derived errors caused by the incomplete estimation of the irradiance [37-39]. This is a serious problem for the visual understanding and quantitative evaluation of the chromophore imaging. Here, 'shading' is the spatial distribution of irradiance. Shading results from the incident angle of the light, the spectral radiant intensity of the light source, and the distance from the light source. If the actual irradiance on the surface of a subject is lower than the estimate, then the apparent reflectance decreases and the chromophore concentrations will be overestimated; this tends to occur on the fringe areas of the subject. Therefore, for a precise calibration of reflectance, besides the radiant intensity distribution of the light, the shape of the subject also must be assessed (unless the areas of interest are limited to small, flat areas in which the irradiance can be fully assessed) [40]. The problem with shading is common among methods that consider nonlinear scattering effects in imaging [42].

Several studies have attempted to correct for the shading effect. In these studies, the shape of each subject was measured [43, 44] or the curvature effect was otherwise extracted [37] and taken into account. However, these approaches require hardware

modifications and additional measurements or else assumptions about the shapes of the samples.

Refractive index measurement (Chap. 4)

Methods for measuring skin refractive index (RI) can be broadly categorized into two kinds based on their measurement area and depth. One class of methods measure the average RI between two interfaces (e.g., the upper and lower surfaces of the epidermis); they utilize the difference between the physical and optical distances between the interfaces [45-47]. The other class of measurements measure the RI of an area close to a surface and utilize the relationship between the incident angle and the reflectance [48-54]. In the case of *in vivo* measurements of skin, the measurement depth is important because the amount of water varies dramatically with depth and it generates a gradient in the RI with depth [55, 56]. In evaluating the behavior of light at air–skin interface, the latter class of measurements is more appropriate since the ratio of surface reflection to interior reflection is sensitive to the RI ratio at the interface [57-59].

The ultimate goal of our research is to measure *in vivo* the RI of a superficial area of a cornified layer. However, since this is difficult, most studies have performed *ex vivo* measurements of slices of skin [52-54]. The main source of difficulty of *in vivo* measurements is undulations in the skin surface [60]. RI measurements generally require precisely measuring the reflectance as a function of the incident angle at the interface between a prism and a sample. Consequently, a flat sample surface is needed to ensure good contact between the prism and the sample. Hence, some modification is required to apply this method to samples with rough surfaces. In some studies, the sample was pressed against the prism by applying a high pressure to achieve good contact [53, 54]. However, this method is not suitable for *in vivo* measurements. Another

significant problem of *in vivo* measurements is their long acquisition times. This is inconvenient for the subject. Furthermore, the skin conditions will change over time since the water content will vary due to occlusions. Due to these difficulties, almost all previous studies performed *ex vivo* measurements of skin slices. This results in other problems. First, this method is destructive. In addition, after being cut off, skin will dry out since its water supply is disrupted; this will change its RI [57, 61]. To make the conditions of samples close to those living skin or to increase the contact area, other studies have used saline [52-54] or high-RI immersion oil [61]. However, various kinds and amounts of liquid are applied and these factors will affect the RI. Therefore, *in vivo* measurements are desirable for evaluating the RI under different conditions and for different individuals.

Translucency measurement (Chap. 5)

Translucency is an important factor in giving skin a natural appearance, and can also provide clues as to the internal condition of the skin. Given the importance of translucency, numerous studies have been performed on this parameter in the fields of medicine [18, 21, 62, 63], cosmetics [64, 65], and computer graphics [66, 67]. In the field of cosmetics, one of the important goals is the improvement of skin appearance in daily life. In the field of medicine, the same can be said for cases where esthetic problems are a major concern. In such cases, the interest is in small variations in factors encountered during daily life (such as changes due to external stimuli like ultraviolet radiation, skin-care activities, or aging) as influences on appearance. The important issue is measuring translucency as an eventual lateral spread of reflected light and relating such measurements to appearance.

Most previous studies, however, have mainly discussed the standard optical

properties of average human skin, with few studies attempting to assess individual differences or variations during daily life. Generally, translucency can be evaluated by calculating the absorption coefficient and effective scattering coefficient [21, 67, 68] or the effective attenuation coefficient [66, 68] from a measured point spread function (PSF). One frequently used measurement configuration is the linear fiber array method, which involves a single optical fiber for light incidence and multiple optical fibers for light measurement lined up in a single row with the edges adjacent [66, 69]. Another proposed configuration is video reflectometry measurement (VRM), which involves focusing light on the measurement surface through a system of lenses and using a camera to acquire images of the returning light [21, 62, 64, 67, 70]. Such conventional methods for translucency measurement need to detect weak signals from points adjacent to the incident point, thus requiring detection over a wide dynamic range and strict shielding from stray light from the environment and the incident point. In addition, given skin unevenness, point sources of light can be affected by the location of incidence. The instruments and protocols for measurement therefore tend to be elaborate to respond to these challenges.

Rapid calculation of diffuse reflectance (Chap. 6)

The reflectance of skin noninvasively provides information about the inner conditions, such as the scattering coefficients, absorption coefficients, and chromophore concentrations [71]. When deriving this information, a Monte Carlo simulation (MCS) has often been used as the standard [72-79], since a MCS precisely follows the behavior of each photon that is scattered from or absorbed in a medium, and the range of scattering and absorption coefficients to which it can be applied is not limited. In addition, a MCS can be applied easily to arbitrary multilayered structures. A multilayered structure is

unavoidable when evaluating the reflectance of skin, which consists of an epidermis that contains melanin and an underlying dermis that contains hemoglobin. Because of its high reliability, a MCS is often used to evaluate approximation methods [72-79], although it has a high computation time. In a MCS, a large number of photons are generated, and each photon numerically propagates through the skin model following designated probabilities of scattering and absorption; from a statistical analysis of these results, the reflectance and other physical quantities are then calculated. Increasing the number of photons increases the precision of the MCS, but it also increases the calculation time, which may become too long to be used for the inverse problem, imaging, or interactive tools. A sufficiently short calculation time is crucial for those applications, since it is necessary to calculate the reflectance many times.

Several studies have attempted to reduce the time required to calculate the reflectance while keeping the results equivalent to those of an MCS [75-77, 79, 80]. These studies were based on a method known as white MCS (WMCS) [75] or single MCS [76, 77, 79], which were primarily developed for solving time-domain problems [75-77, 79]. The WMCS is based on the Beer-Lambert (B-L) law, which states that the absorbance of photons traveling through a medium along a certain trajectory can be calculated from the path length and the absorption coefficient. The WMCS also utilizes similarity: In a semi-infinite and homogeneous medium without absorption, if μ_s' grows to α times the original condition, then a homothetic trajectory that is $1/\alpha$ times smaller can be associated with the original one [75, 76]. With similarity, we only need to calculate the MCS one time without absorption, and then for any absorption and scattering coefficient of the medium, we can derive a histogram for the path length and determine the spatial distribution of reflectance in the time domain. Not apply only to semi-infinite and

homogeneous media, a WMCS can be applied to an arbitrary composite structure composed of multiple media if the path length in each medium can be calculated for each trajectory [78, 80]. However, in such cases, similarity cannot be fully utilized, and the application range for a certain precalculated data set is limited. For a multilayered structure like skin, the optical path-length matrix method (OPLM) has been developed [78]. In the OPLM, a MCS is used to determine the path lengths for each photon in the epidermis and in the dermis; this is recorded on a two-dimensional histogram. The absorption coefficient is determined, and the reflectance is then calculated from the two-dimensional histogram by using the B-L law [78]. Although this method works with a multilayer model, if we want to change any of the scattering coefficients or the thickness of any of the layers, we must recalculate everything.

1.2. Motivation

Internal reflection depends on the optical properties such as refractive index, scattering coefficient, and absorption coefficient, and these optical properties are determined by tissue structure and distribution of chromophores. The values and the wavelength dependencies vary with individuals, regions, and physiological conditions. For the estimation of these properties, several methods have been proposed. However, further improvement is required in the field of skin diagnosis and functional evaluation, in terms of manageability, measuring time, and cost. On another front, light propagation Monte Carlo simulation (MCS) is broadly used as a powerful tool for correlating skin reflectance and optical properties. However, MCS takes enormous time in deriving precise results. The calculation time is so long that it poses a serious practical issues even in off-site

analysis. If we resolve these issues, precise and quick evaluation of the skin appearance and functions become more accessible.

1.3. Synopsis of the dissertation

In Chapter 2, fundamental knowledge related to the studies in the dissertation is described.

In Chapter 3, the method for the reduction of shading related errors in skin chromophore imaging is proposed. Several methods have been proposed for the estimation of chromophore concentrations with skin reflectance until now. The B-L method and modified B-L method are simple but inconsistent with real conditions, therefore many methods have been studied to improve the inconsistency. However, those improved methods raised newly emerged problem of shading-derived artifact in imaging, which comes from the non-linearity introduced to reflect the effect of scattering. It is desirable to satisfy both of the improvement of reflection model and the reduction of shading-derived artifact. We tried to ensure the compatibility between them by improving the compensation formulae in the empirical method aided by MCS.

In Chapter 4, a measuring method for skin refractive index is proposed. Refractive index rules the reflection and transmission at interface of materials. Although refractive index of liquid can be easily derived, deriving that of solid material is extremely difficult mainly due to the unevenness of surface, which is true of human skin. Some methods have been proposed which apply liquid of known refractive index to make a solid material measurable. However, in the case of skin, the contact with liquid itself cause the change of refractive index, and the type of liquid is limited to harmless material. We tried to overcome the issue and to estimate the refractive index of skin *in vivo*.

In Chapter 5, newly developed method for translucency measurement is proposed. Translucency is recognized as an important attribute of skin for natural appearance, which is characterized with PSF. In diffusion approximation, PSF and reflectance are correlated with scattering and absorption coefficients. One of the problem of the method is that two measuring methods for reflectance and PSF use completely different optical configuration. We tried to measure translucency under similar optical configuration to reflectance measurement. In the method, translucency index is derived from reflectances with different illuminated areas. In addition, we tried to derive scattering and absorption coefficients from translucency index and reflectance.

In Chapter 6, a calculation method is proposed, which derive equivalent results to MCS with substantially short calculation time with the combination of white MCS and adding-doubling method. While the photon trajectory of internal reflectance is stochastic and quite complex, MCS is the method to simulate the trajectory faithfully. For this reason, MCS is a powerful tool in estimating inner condition of skin from internal reflection, and often used as an absolute standard and compared with other methods to estimate the correctness of them. The significant problem of MCS is the enormous calculation time, which makes other approximation method still needed and studied. If MCS could be processed in a short time, MCS will be used under various situations. Therefore, we tried to acquire equivalent results to MCS with short time calculations.

2. Fundamental knowledge

2.1. Structure of human skin

The content of this section is mainly based on Ref. 81.

Human skin is placed at the boundary between human body and the outer world. The skin plays important roles for constancy of temperature regulation, sensitive organ, and preventing human body from physical and chemical irritation, and water loss and inrush. While the skin has complex structure to achieve the roles, the structure is generally divided into three layers of epidermis, dermis and subcutaneous adipose beginning at the top.

Epidermis is classified into four layers of basal cell layer, prickle cell layer, granular cell layer, and horny cell layer from the bottom. Epidermal cells, which are born at basal cell layer, are pushed up by ones follow on, then detach from skin after rising to surface. The life of an epidermal cell from born to detachment is called as *turnover*, whose length is about 45 days on average. The cells become flat while they go through prickle cell layer and granular cell layer, then they become extremely flat when they reach horny cell layer. At horny cell layer, the cell form is disappeared and layered structure arise, which prevent from entrance and exit of substances such as water. Horny cell layer is otherwise known as stratum corneum. A major chromophore in epidermis is melanin,

which is created at melanocyte. Melanocyte exists at hair matrix and basal layer, and deliver formed melanin to adjacent basal cell. Melanin is pushed up along with epidermal cells. Melanin is hardly left at horny cell layer, since it is decomposed until it arrives at horny cell layer. Melanin plays an important role of protection against ultraviolet. On the other hand, excess production of melanin causes spot, which poses aesthetic problem.

Dermis is anatomically classified into three layers of papillary layer, subpapillary layer, and reticular layer from the top. In dermis, vascular network including capillary blood vessel is spread, which includes hemoglobin in blood, and it is a principal chromophore in dermis. While the important role of hemoglobin is conveyance of oxygen, the reflectance spectrum depends on the status whether it has oxygen (oxygenated) or not (deoxygenated).

Subcutaneous fat layer stands for adipose tissue between dermis and fascia. The layer stores neutral fat, and has roles of cushion for physical external force, thermal insulation, and heat production. The fat layer does not have notable chromophore.

2.2. Classical optics

2.2.1. Optical phenomena at interface

2.2.1.1. Refractive index

The content of this subsection is mainly based on Ref. 82.

Refractive index is defined as the ratio of light velocity in a material to that in vacuum. In the case that the material is a perfect insulator and the space is charge-free, Maxwell's equation is transformed into the following equation:

$$\begin{cases} \nabla^2\vec{\mathbf{E}} = \varepsilon\mu\dfrac{\partial^2\vec{\mathbf{E}}}{\partial t^2} \\ \nabla^2\vec{\mathbf{H}} = \varepsilon\mu\dfrac{\partial^2\vec{\mathbf{H}}}{\partial t^2} \end{cases} \quad (2\text{-}1)$$

Here, ε and μ are electric permittivity and magnetic permeability, and $\vec{\mathbf{E}}$ and $\vec{\mathbf{H}}$ are electric and magnetic fields. Those equations are differential equations for waves, which indicates $\vec{\mathbf{E}}$ and $\vec{\mathbf{H}}$ are waves whose transmitting velocity v is $1/\sqrt{\varepsilon\mu}$. Assuming electric permittivity and magnetic permeability in vacuum are ε_0 and μ_0, and those in a material are $\varepsilon = \varepsilon_r\varepsilon_0$ and $\mu = \mu_r\mu_0$, respectively, the refractive index of the material *n* becomes $\sqrt{\varepsilon_r\mu_r}$. If the material is not electromagnetic material, $\mu_r = 1$, therefore, $n \simeq \sqrt{\varepsilon_r}$.

Meanwhile, if the material absorb light, expanding refractive index to complex number, the effect of absorption can be expressed as imaginary of the complex refractive index. The electric field of light moving in the *x*-axial direction in a material is expressed as:

$$\vec{\mathbf{E}} = \vec{\mathbf{E}}_0\exp\left(-i\omega\left(t - nx/c\right)\right), \quad (2\text{-}2)$$

with refractive index *n*, when the material does not absorb light, solving Eq. 2-1. Here, ω is the angular velocity and *c* is the light velocity in vacuum. If the refractive index is expanded to complex number and *n* is replaced with $N=n+i\kappa$, the equation become:

$$\vec{\mathbf{E}} = \vec{\mathbf{E}}_0\exp\left(-i\omega\left(t - Nx/c\right)\right) = \vec{\mathbf{E}}_0\exp\left(-\kappa\omega x/c\right)\exp\left(-i\omega\left(t - nx/c\right)\right). \quad (2\text{-}3)$$

This means that the imaginary part of the expanded refractive index stands for absorption. Since the absorption coefficient α is calculated from $I = I_0 \exp(-\alpha x)$ (see Sec. 2.2.2), and light intensity is proportional to $\left|\vec{\mathbf{E}}_0\right|^2$, the relation between κ and α is

$$\alpha = 2\omega\kappa/c = 4\pi\kappa/\lambda. \tag{2-4}$$

2.2.1.2. Reflection and transmission at flat interface

The content of this subsection is mainly based on Ref. 82.

When light passes through an interface between two media with different refractive indices, the light is reflected and refracted at the interface. Assuming the light passes from medium 1 to medium 2, and transmitting velocities are v_1, v_2, refractive indices are n_1, n_2, electric permittivities are $\varepsilon_1 = \varepsilon_{r1}\varepsilon_0$, $\varepsilon_2 = \varepsilon_{r2}\varepsilon_0$, and the magnetic permiabilities are $\mu_1 = \mu_{r1}\mu_0$ and $\mu_2 = \mu_{r2}\mu_0$, respectively, those values can be associated with each other as:

$$v_1 = \frac{1}{\sqrt{\varepsilon_1\mu_1}},\ v_2 = \frac{1}{\sqrt{\varepsilon_2\mu_2}},\ n_1 = \sqrt{\varepsilon_{r1}\mu_{r1}},\ n_2 = \sqrt{\varepsilon_{r2}\mu_{r2}}. \tag{2-5}$$

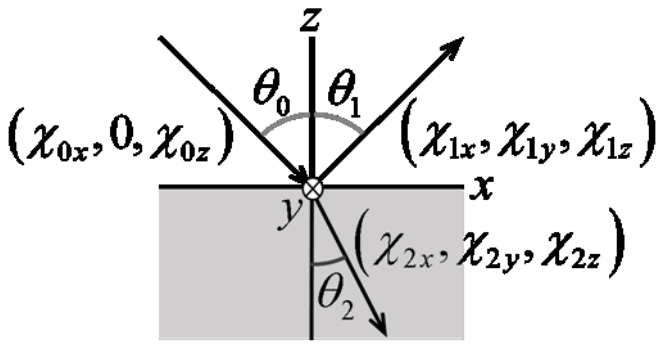

Fig. 2-1 Coordinate system.in Sec. 2.2.1.2

Set the incident point as the origin position, the normal direction as z-axis, and x- and

y-axis so as to make the incidence plane be x-z plane (Fig. 2-1). The unit vectors toward incident, reflected, and refracted directions are expressed as (χ_{0x},0,χ_{0z}), (χ_{1x},χ_{1y},χ_{1z}) and (χ_{2x},χ_{2y}, χ_{2z}), and the incident, reflected, and refracted angle are expressed as θ_0, θ_1 and θ_2. The electric fields of incidence, reflection and refraction are $\vec{\mathbf{E}}$, $\vec{\mathbf{E}}_1$ and $\vec{\mathbf{E}}_2$, and angular velocities are ω, ω_1 and ω_2. Then, the general solutions of Eq. 2-1 become:

$$\vec{\mathbf{E}} = \vec{\mathbf{E}}^0 \sin \omega \left(t - \frac{\chi_{0x} x + \chi_{0z} z}{v_1} \right), \tag{2-6}$$

$$\vec{\mathbf{E}}_1 = \vec{\mathbf{E}}_1^{\,0} \sin \left(\omega_1 \left(t - \frac{\chi_{1x} x + \chi_{1y} y + \chi_{1z} z}{v_1} \right) + \delta_1 \right), \tag{2-7}$$

$$\vec{\mathbf{E}}_2 = \vec{\mathbf{E}}_2^{\,0} \sin \left(\omega_2 \left(t - \frac{\chi_{2x} x + \chi_{2y} y + \chi_{2z} z}{v_2} \right) + \delta_2 \right). \tag{2-8}$$

Here, δ_1, δ_2 is the phase shifts. Since the tangential component of electric field must be equal between both sides of the interface, all of the values of inside of sine must be the same, therefore, the following relationship is derived:

$$\omega = \omega_1 = \omega_2, \tag{2-9}$$

$$\delta_1 = \delta_2 = 0 \, or \, \pi, \tag{2-10}$$

$$\chi_{1y} = \chi_{2y} = 0, \tag{2-11}$$

$$\chi_{0x}/v_1 = \chi_{1x}/v_1 = \chi_{2x}/v_2 . \tag{2-12}$$

These equation indicate that the angular velocity does not change (Eq. 2-9), the phase transition is 0 or π (Eq. 2-10), reflection and refraction is on the incident plane (Eq. 2-11). Eq. 2-12 is transformed to:

$$\sin\theta_1/v_1 = \sin\theta_1'/v_1 = \sin\theta_2/v_2 . \tag{2-13}$$

Then, the following relationship can be derived:

$$\theta_1 = \theta_1', \tag{2-14}$$

$$\frac{\sin\theta_1}{\sin\theta_2} = \frac{v_1}{v_2} = \frac{n_1}{n_2}. \tag{2-15}$$

Eq. 2-14 represents the reflection angle is equal to the incident angle. Eq. 2-15 is Snell's law.

2.2.1.3. Fresnel equation

The content of this subsection is mainly based on Ref. 82.

Since the electric and magnetic field must be equal between both sides of the interface, the boundary condition become:

$$E_x + E_{1,x} = E_{2,x}, \quad E_y + E_{1,y} = E_{2,y} \tag{2-16}$$

$$H_x + H_{1,x} = H_{2,x}, \quad H_y + H_{1,y} = H_{2,y} \tag{2-17}$$

Splitting E into the component parallel to the incident plane $E^{\parallel}$ (p-wave), and that perpendicular to the incident plane $E^{\perp}$ (s-wave), and substituting Eq. 2-6, 2-7, 2-8 to 2-16, the following equations are derived:

$$E^{\parallel}\cos\theta - E_1^{\parallel}\cos\theta = E_2^{\parallel}\cos\theta_2 \tag{2-18}$$

$$E^{\perp} + E_1^{\perp} = E_2^{\perp} \tag{2-19}$$

In the meantime, $\vec{\mathbf{H}} = \sqrt{\varepsilon/\mu}\left(\vec{\mathbf{p}} \times \vec{\mathbf{E}}\right)$ assuming $\vec{\mathbf{p}}$ is the unit vector toward traveling direction. Since $\mu = 1$ except electromagnetic material, following approximation is hold:

$$\sqrt{\frac{\varepsilon}{\mu}} = \sqrt{\frac{\varepsilon_r \varepsilon_0}{\mu_r \mu_0}} \simeq n\sqrt{\frac{\varepsilon_0}{\mu_0}} \quad (2\text{-}20)$$

Therefore, H_x is proportional to nE_y, and H_y is proportional to nE_x. Then, the boundary condition become:

$$n_1\left(E^{\perp} - E_1^{\perp}\right)\cos\theta = n_2 E_2^{\perp}\cos\theta_2, \quad n_1\left(E^{\parallel} + E_1^{\parallel}\right)\cos\theta = n_2 E_2^{\parallel} \quad (2\text{-}21)$$

Then, the following relationship is derived.

$$E_1^{\parallel} = \frac{\tan(\theta - \theta_2)}{\tan(\theta + \theta_2)} E^{\parallel}, \quad E_1^{\perp} = \frac{\sin(\theta - \theta_2)}{\sin(\theta + \theta_2)} E^{\perp} \quad (2\text{-}22)$$

$$E_2^{\parallel} = \frac{2\sin\theta_2\cos\theta}{\sin(\theta + \theta_2)\cos(\theta - \theta_2)} E^{\parallel}, \quad E_2^{\perp} = \frac{2\sin\theta_2\cos\theta}{\sin(\theta + \theta_2)} E^{\perp} \quad (2\text{-}23)$$

These are Fresnel's equation. Here, the energy is proportional to the amplitude. Therefore, the reflectance and transmittance can be derived as:

$$R = \left(\left|E_1^{\perp}\right|^2 + \left|E_1^{\parallel}\right|^2\right)/2, \quad T = \left(\left|E_2^{\perp}\right|^2 + \left|E_2^{\parallel}\right|^2\right)/2 \quad (2\text{-}24)$$

in the case of non-polarized light.

2.2.1.4. Total reflection

The content of this subsection is mainly based on Ref. 82.

When light passes through an interface from a medium of higher refractive index to that of lower refractive index, the refraction angle θ_2 cannot be derived according to Snell's law (Eq. 2-15) for a particular range of θ_1. The maximum angle of θ_1 that can define θ_2 as real number is called as critical angle, and given with the following equation:

$$\theta_c = \sin^{-1}\frac{n_1}{n_2} \quad (2\text{-}25)$$

If the incident angle is larger than θ_c, the light will be totally reflected.

Meanwhile, under this condition, if we think that only incident and reflected light exist, the electric and magnetic fields become discontinuous at the interface of the media, which does not satisfy Maxwell's equations. In fact, the electric and magnetic fields are leaked in the medium of transmitted side as near-field light, which is called as evanescent wave.

In the case of skin, the total reflection will not occur at the time of incidence, but do at the time of exit, since the refractive index of skin is higher than that of air. Therefore, the effect should be considered. On the other hand, total refraction is a useful phenomenon for the high-precision measurement of refractive index.

2.2.1.5. Effective medium approximation

The content of this subsection is mainly based on Ref.83.

If refractive index of medium varies along the light path, the light will scatter and change the direction in general. However, if the size of variation is much smaller than the wavelength of light, the light becomes insensitive to the fluctuation of the refractive index. The light in a composite of materials with several refractive index act like it travels in a homogeneous material with one effective refractive index, assuming the size of mixture is smaller enough than the wavelength. There is an equation to derive an effective refractive index ϵ_{eff}. In the case that an arbitral number of materials are mixed, from an expansion of Lorentz-Lorentz mixing rule, ϵ_{eff} is calculated with the following relationship:

$$\frac{\varepsilon_{eff}-\varepsilon_0}{\varepsilon_{eff}+2\varepsilon_0}=f_1\frac{\varepsilon_1-\varepsilon_0}{\varepsilon_1+2\varepsilon_0}+f_2\frac{\varepsilon_2-\varepsilon_0}{\varepsilon_2+2\varepsilon_0}+\cdots \tag{2-26}$$

Here, f_i is volume fractions. In the case of insulator, the root of ϵ can be considered as refractive index. Easily, the following equation also used:

$$\varepsilon_{eff} = f_1\varepsilon_1 + f_2\varepsilon_2 + \cdots \tag{2-27}$$

However, we should note that those equations does not hold if the interaction between those materials are strong.

In the case of skin, the refractive index of stratum corneum is about 1.5, however, 1.4 is often used for *in vivo* skin. The difference can be explained with the water content of skin, while *in vivo* skin is moist.

2.2.1.6. Scattering on skin surface

Surface reflection on skin is determined by the surface topography and the refractive index around the surface [84]. To analyze the surface reflection, the technique of ray tracing may be effective. Reflection from a certain shape can be simulated assuming a certain configuration of light and shading model. A shape of skin can be measured with a certain 3D digitizer. The topography smaller than the resolution of the digitizer is taken in a shading model such as Torrance-Sparrow model.

2.2.2. Beer-Lambert law

In general, in the case that a certain physical amount decreases by the amount proportional to its quantity, the physical value decreases exponentially. Specifically, attenuation of light intensity against light path length is called as Beer-Lambert law. The differential equation for the condition that light attenuates proportional to the intensity of light itself is as following:

$$dI = -\mu I dx. \tag{2-28}$$

Here, I is the intensity of light, dx is an infinitesimal path length, dI is the amount of

attenuation of light, and μ is the extinction coefficient. It is solved as:

$$I = I_0 \exp(-\mu x). \tag{2-29}$$

The equation can be applied to both of absorption and scattering. μ for absorption is absorption coefficient μ_a, and that for scattering is scattering coefficient μ_s. For the light attenuated by absorption and scattering, the differential equation become:

$$dI = -\mu_s I dx - \mu_a I dx$$

Therefore, defining the extinction coefficient μ_t as $\mu_t=\mu_a+\mu_s$, the differential equation is solved as:

$$I = I_0 \exp(-\mu_t x)$$

2.2.3. Internal scattering of skin

See about light scattering by a spherical particle. Assuming λ as the wavelength, D as the diameter of the particle, and defining the size parameter as $\alpha=\pi D/\lambda$, the scattering under the condition $\alpha\approx 1$ is referred to as Mie scattering, and that under the condition $\alpha \ll 1$ is referred to as Rayleigh scattering. When $\alpha \gg 1$, light acts following geometric optics. Rayleigh scattering explain the scattering by atomic and molecular level. Mie scattering depends on the shape and size (and the distribution of those) of scatterer ,while Rayleigh scattering does not assume the size and shape of scatterer (but $\alpha \ll 1$). Mie theory, which derive the scattering from a perfect sphere, is used to analyze the Mie scattering. Rayleigh scattering is derived as a scattering from harmonic oscillator. In deriving the analytical solutions of those scattering, several assumptions are made. In the calculations of scattering, incident wave is approximated with plane wave, although a photon is localized actually. The derived amplitude is that for the locations far enough

from the scatterer. Therefore, if the next scattering is occurred near the position of the previous scattering, the scattering becomes different from the sum of each scattering.

In the skin model used in the dissertation, scattering coefficient is defined as the sum of the term proportional to λ^{-4} and $\lambda^{-1.5}$, which reflect Rayleigh scattering and Mie scattering, respectively.

2.2.3.1. Mie scattering

The content of this subsection is mainly based on Ref. 85.

Mie scattering stands for the scattering in the case that the wavelength is roughly the size of scatterer. At this region, the wavelength dependency of scattering coefficient is smaller than the case of Rayleigh scattering, which is derived from Mie theory. Meanwhile, Mie theory does not make any assumptions except that the scatterer is a perfect uniform sphere, therefore the derived equations are applicable irrespective of the size of the scatterer.

Assuming the incident light as a plane wave, from the rule that the electric and magnetic fields and their first derivations are continuous at the surface of the sphere, the scattering cross-section and angular distribution are derived. Since the process of the derivation is very complicated, only the results are described here. With polar coordinate, the electromagnetic field of scattered wave by a scatterer becomes:

$$\begin{cases} E_\theta^{(s)} = \dfrac{i\cos\phi}{k^{(I)}r} e^{ik^{(I)}r} S_2(\theta), \\ E_\phi^{(s)} = \dfrac{i\sin\phi}{k^{(I)}r} e^{ik^{(I)}r} S_1(\theta), \end{cases} \tag{2-30}$$

$$\begin{cases} H_{\phi}^{(s)} = \dfrac{ik^{(I)}}{k_2^{(I)}} E_{\theta}^{(s)} = \sqrt{\dfrac{\varepsilon^{(I)}}{\mu^{(I)}}} E_{\theta}^{(s)}, \\ H_{\theta}^{(s)} = -\dfrac{ik^{(I)}}{k_2^{(I)}} E_{\phi}^{(s)} = \sqrt{\dfrac{\varepsilon^{(I)}}{\mu^{(I)}}} E_{\phi}^{(s)}. \end{cases} \tag{2-31}$$

Here, the superscript (s) stands for the components for scattering, the superscript (I) stands for outside of the sphere, and k and k_2 are wave numbers of incident and scattered light, respectively. $S_1(\theta)$ and $S_2(\theta)$ are expressed as following.

$$\begin{cases} S_1(\theta) \equiv \sum_{l=1}^{\infty} \dfrac{2l+1}{l(l+1)} \left\{ a_l \pi_l(\cos\theta) + b_l \tau_l(\cos\theta) \right\} \\ S_2(\theta) \equiv \sum_{l=1}^{\infty} \dfrac{2l+1}{l(l+1)} \left\{ a_l \tau_l(\cos\theta) + b_l \pi_l(\cos\theta) \right\} \end{cases} \tag{2-32}$$

$$\begin{cases} \pi_l(\cos\theta) = P_l^1(\cos\theta) / \sin\theta, \\ \tau_l(\cos\theta) = \dfrac{d}{d\theta} P_l^1(\cos\theta) = -\sin\theta P_l^{1\prime}(\cos\theta). \end{cases} \tag{2-33}$$

$$\begin{cases} {}^{e}B_l = i^{l+1} \dfrac{2l+1}{l(l+1)} \dfrac{k_2^{(I)} k^{(II)} \psi_l'(q) \psi_l(\hat{n}q) - k_2^{(II)} k^{(I)} \psi_l'(\hat{n}q) \psi_l(q)}{k_2^{(I)} k^{(II)} \zeta_l^{(I)\prime}(q) \psi_l(\hat{n}q) - k_2^{(II)} k^{(I)} \psi_l'(\hat{n}q) \zeta_l(q)}, \\ {}^{m}B_l = i^{l+1} \dfrac{2l+1}{l(l+1)} \dfrac{k_2^{(I)} k^{(II)} \psi_l(q) \psi_l'(\hat{n}q) - k_2^{(II)} k^{(I)} \psi_l'(q) \psi_l(\hat{n}q)}{k_2^{(I)} k^{(II)} \zeta_l^{(I)}(q) \psi_l'(\hat{n}q) - k_2^{(II)} k^{(I)} \psi_l(q) \zeta_l^{(I)\prime}(\hat{n}q)}. \end{cases} \tag{2-34}$$

$P_l^m(\cos\theta)$ are associated Legendre polynomials. $\psi_l(\rho) = \rho j_l(\rho)$ and $\zeta_l^{(1)}(\rho) = \rho h_l^{(1)}(\rho)$, where $j_l(\rho)$ and $h_l(\rho)$ are spherical Bessel functions and type 1 spherical Hankel functions. Superscript (II) represents inside of sphere, and $q = k^{(I)} a$. The primes represent the first derivatives. In addition, a_l and b_l are introduced as:

$$\begin{cases} {}^{e}B_l = i^{l+1}\dfrac{2l+1}{l(l+1)}a_l, \\ {}^{m}B_l = i^{l+1}\dfrac{2l+1}{l(l+1)}b_l. \end{cases} \tag{2-35}$$

From the equations above, extinction cross section, scattering coefficient, and absorption coefficient are derived as:

$$C_{ext} = \frac{4\pi}{k^{(I)2}}\mathrm{Re}\{S_2(0)\} = \frac{4\pi}{k^{(I)2}}\sum_{l=1}^{\infty}(2l+1)\mathrm{Re}\{a_l + b_l\}, \tag{2-36}$$

$$C_{sca} \equiv I^{(s)}/I^{(i)} = \frac{2\pi}{k^{(I)2}}\sum_{l=1}^{\infty}(2l+1)\left(|a_l|^2 + |b_l|^2\right), \tag{2-37}$$

$$C_{abs} = C_{ext} - C_{sca}. \tag{2-38}$$

If the particle size distribution is given, the wavelength dependency of scattering is derived with those equations. Here, the exact solution of Mie theory has a sharp angular distribution. However, since scatterers are hardly exact spheres and the particle sizes have distributions, the angular distribution on averaged will not become sharp usually.

2.2.3.2. Rayleigh scattering

The content of this subsection is mainly based on Ref. 82.

Rayleigh scattering stands for the scattering in the case that the size of scatterer is much smaller than wavelength [82]. Rayleigh scattering can be solved with electric dipole model. Here, the derivation of formalism is briefly described. When an electron is bound to an atom by elastic force (with natural frequency ω_0), the motion equation of the electron is:

$$m\frac{d^2x}{dt^2} = -m\omega_0^2 x + e\tilde{E}\exp(i\omega t). \tag{2-39}$$

Substituting $x=\tilde{x}\exp(i\omega t)$ in Eq. 2-39,

$$\tilde{x}=\frac{e\tilde{E}}{m\left(\omega_0^2-\omega^2\right)} \quad \therefore \tilde{p}\equiv e\tilde{x}=\frac{e^2\tilde{E}}{m\left(\omega_0^2-\omega^2\right)}. \tag{2-40}$$

Consider the irradiation from oscillating dipole with moment $p=\tilde{p}e^{i\omega t}$. As described later, the Poynting vector ($\vec{\mathbf{S}}=\vec{\mathbf{E}}\times\vec{\mathbf{H}}$) is given as:

$$S=\frac{\omega^4}{(4\pi)^2\varepsilon_0 c^3 r^2}\left|p_r\times\hat{n}\right|^2\hat{n}, \quad \left(\hat{n}=\frac{\vec{\mathbf{r}}}{r}\right) \ (*) \tag{2-41}$$

Here, p_r is the real part of p. Assuming electric field $\vec{\mathbf{E}}=\vec{\mathbf{E}}_1\cos\omega t+\vec{\mathbf{E}}_2\sin\omega t$, the differential cross-section becomes:

$$p_r=-\frac{e^2}{m\left(\omega_0^2-\omega^2\right)}\left(\vec{\mathbf{E}}_1\cos\omega t+\vec{\mathbf{E}}_2\sin\omega t\right). \tag{2-42}$$

Therefore,

$$S=\frac{e^4}{(4\pi)^2\varepsilon_0 c^3 m^2 r^2}\left(\frac{\omega^2}{\omega_0^2-\omega^2}\right)^2\left(\left(\vec{\mathbf{E}}_1\cos\omega t+\vec{\mathbf{E}}_2\sin\omega t\right)\times\hat{n}\right)^2\hat{n}. \tag{2-43}$$

The integration of Eq. 2-43 over time becomes:

$$\bar{S}=\frac{1}{2}a_0^2 c\varepsilon_0\frac{1}{r^2}\left(\frac{\omega^2}{\omega_0^2-\omega^2}\right)^2\left(\left(\vec{\mathbf{E}}_1\times\hat{n}\right)^2+\left(\vec{\mathbf{E}}_2\times\hat{n}\right)^2\right). \tag{2-44}$$

On the other hand, the Poynting vector of incident plane wave is:

$$S_i=\sqrt{\frac{\varepsilon_0}{\mu_0}}\left(\vec{\mathbf{E}}_1\cos\omega t+\vec{\mathbf{E}}_2\sin\omega t\right)^2\frac{\vec{\mathbf{k}}}{k}. \tag{2-45}$$

Averaging over time,

$$\overline{S_i}=\frac{c\varepsilon_0}{2}\left(E_1^2+E_2^2\right). \tag{2-46}$$

From $d\sigma = Sr^2 d\Omega / \overline{S_i}$, differential cross-section becomes:

$$\frac{d\sigma}{d\Omega} = a_0^{\,2}\left(\frac{\omega^2}{\omega_0^{\,2}-\omega^2}\right)^2 \frac{\left(\vec{\mathbf{E}}_1\times\hat{n}\right)^2+\left(\vec{\mathbf{E}}_2\times\hat{n}\right)^2}{E_1^{\,2}+E_2^{\,2}} \propto \left(\frac{\omega^2}{\omega_0^{\,2}-\omega^2}\right)^2 = \left(\frac{\lambda_0^{\,2}}{\lambda^2-\lambda_0^{\,2}}\right)^2. \tag{2-47}$$

When the size of scatterer is smaller than light wavelength, $\lambda_0 \ll \lambda$, therefore,

$$\frac{d\sigma}{d\Omega} \propto \left(\frac{\lambda_0^{\,2}}{\lambda^2-\lambda_0^{\,2}}\right)^2 \propto \frac{1}{\lambda^4}. \tag{2-48}$$

(*) Derivation of Eq. 2-41

Assume the electric current $I(t)$ of length dl at origin. E and H stand for the electromagnetic field which is generated by current at an arbitral point P. The polar coordinate of P is set to (r, θ, ϕ), and the unit vectors of each element is expressed as $\mathbf{e}_r$, $\mathbf{e}_\theta$, $\mathbf{e}_\phi$. The E and H from current can be solved with electromagnetic potential. Considering the fact that the component which attenuate faster than $1/r$ is negligible at a point far from the source, E and H become:

$$\begin{cases} E = \dfrac{dl}{4\pi\varepsilon_0}\dfrac{1}{c^2 r}\dfrac{\partial}{\partial t} I\left(t-\dfrac{r}{c}\right)\sin\theta\,\mathbf{e}_\varphi, \\ H = \dfrac{dl}{4\pi}\dfrac{1}{cr}\dfrac{\partial}{\partial t} I\left(t-\dfrac{r}{c}\right)\sin\theta\,\mathbf{e}_\varphi. \end{cases} \tag{2-49}$$

Consider the case that the moment of an electric dipole varies as $p = p_0 \exp(i\omega t)$. Since the current can be expressed with $I(t)\,dl = i\omega p_0 \exp(i\omega t)$,

$$\begin{cases} E = -\dfrac{1}{4\pi\varepsilon_0} p_0 \sin\theta \exp\left(i\omega\left(t-r/c\right)\right)\dfrac{\omega^2}{c^2 r}\mathbf{e}_\theta, \\ H = -\dfrac{1}{4\pi} p_0 \sin\theta \exp\left(i\omega\left(t-r/c\right)\right)\dfrac{\omega^2}{cr}\mathbf{e}_\varphi. \end{cases} \tag{2-50}$$

From these equations, Eq. 2-41 is derived.

2.2.3.3. Anisotropy of scattering

Even if the frequency of scattering is the same, the motion of photons on average will vary according to the angular distribution of photons in a single scattering. Therefore, the scattering angular distribution also should be considered as well as the frequency. As an indicator for the angular distribution of a scattering, anisotropy coefficient g is used, which is defined with the following equation:

$$g = \int_0^{\pi} p(\theta)\cos\theta 2\pi \sin\theta d\theta. \tag{2-51}$$

Here, $p(\theta)$ is the angular distribution of photons in a single scattering. In the case of isotropic scattering, g becomes zero, and in the case of total back scattering and that of total forward scattering, g becomes -1 and 1, respectively. In tracing photons numerically, g must be transformed into $p(\theta)$. As a standard angular distribution, Henyey-Greenstein function is used. The form is the following:

$$p(\theta) = \frac{1}{4\pi}\frac{1-g^2}{\left(1+g^2-2g\cos\theta\right)^{3/2}}. \tag{2-52}$$

This equation holds the following relationships:

$$\int_0^{\pi} p(\theta)2\pi\sin\theta d\theta = 1, \quad \int_0^{\pi} p(\theta)\cos\theta 2\pi\sin\theta d\theta = g. \tag{2-53}$$

In practice, the following equation, which is derived by variable transformation, is used.

$$p(\cos\theta) = \frac{1}{2}\frac{1-g^2}{\left(1+g^2-2g\cos\theta\right)^{3/2}}. \tag{2-54}$$

2.2.3.4. Depolarization

A photon has an attribute of polarization, which is associated with the direction of electric field of the photon (see Sec. 2.2.1.3). Assuming the polarization of all photons in the incident light are the same at initial, the polarization as a whole decreases with repetition

of scattering, which is called as depolarization. Depolarization is unique to internal diffusion light. In the case of surface reflection, the light direction is changed only once at surface, and the reflected light is still polarized if the incident light is polarized. With the phenomenon, surface reflection and inner reflection can be separated with considerable accuracy. Setting a polarizer at between light and object, and make incident light only vertical wave, the surface reflection is contained only in vertical wave while inner reflection is contained in both vertical wave and horizontal wave equally. Using polarizer is effective for reducing surface reflection. However, we should note that internal reflection is not completely depolarized if the number of scattering is not so large.

2.2.4. Absorption

A photon is absorbed when the photon excites the energy level (usually of electronic orbital) of material on the trajectory. The energy level of material is defined by the chemical structure and vary with materials. The fact is applied to such as identification of material.

In the case of skin, principal chromophore is melanin in epidermis and hemoglobin in dermis. While hemoglobin plays the role of conveyance of oxygen, it has different absorption spectrum according to whether it holds oxygen (oxygenated hemoglobin) or not (deoxygenated hemoglobin).

2.3. Calculation model for skin optics

Among the calculation models introduced in Sec. 1.1.1, some models are picked up and described again here with formulae.

2.3.1. Beer-Lambert method

Here we assume three layer model of epidermis, dermis and fat from top, no scattering in epidermis and dermis, reflectance r_f at fat layer, and the thickness of epidermis and dermis as d_e and d_d. Then, the light pass through epidermis and dermis layer twice, so the path length in epidermis and dermis become $2d_e$ and $2d_d$. Therefore, the reflectance becomes:

$$R(\lambda) = r_f \cdot \exp\left(-2\left(C_m \mu_m(\lambda) d_e + C_{oh} \mu_{oh}(\lambda) d_d + C_{dh} \mu_{dh}(\lambda) d_d\right)\right). \quad (2\text{-}55)$$

Here, μ_e and μ_d are the absorbance in epidermis and dermis. C_m, C_{oh}, C_{dh} represents the concentrations of melanin, oxygenated hemoglobin, and deoxygenated hemoglobin. Then, absorbance is expressed as:

$$A(\lambda) = -\ln R(\lambda) = -\ln r_f + 2 \cdot \left(C_m \mu_m(\lambda) d_e + C_{oh} \mu_{oh}(\lambda) d_d + C_{dh} \mu_{dh}(\lambda) d_d\right). \quad (2\text{-}56)$$

This means that absorbance can be expressed as linear combination of absorption coefficient and constant term. The coefficient of each term in the linear combination is proportional to the chromophore concentrations. Setting μ of each chromophore as explanatory variable and A as objective variable, multiple regression analysis leads its coefficients, which are proportional to the respective chromophore concentrations.

2.3.2. Modified Beer-Lambert method

In modified B-L method, the light scattering in epidermis and dermis bring the changes in the path length, which depend on the wavelength. In consequence, the equation becomes:

$$A(\lambda) = \ln r_f - 2 \cdot \left(C_m \mu_m(\lambda) d_e(\lambda) + C_{oh} \mu_{oh}(\lambda) d_d(\lambda) + C_{dh} \mu_{dh}(\lambda) d_d(\lambda)\right) \quad (2\text{-}57)$$

The difference between Eq. 2-56 and 2-57 is whether d depends on wavelength or not.

To derive C, the products of $\mu s \cdot$ and ds become the explanatory coefficients, which should be derived by other experiments or calculations. Usually, the product of μ and d is derived as a whole. In the case with normal RGB image, independent component analysis is an effective method for deriving the vectors of melanin and hemoglobin, assuming the distributions of melanin and hemoglobin are independent.

2.3.3. Kubelka-Munk theory

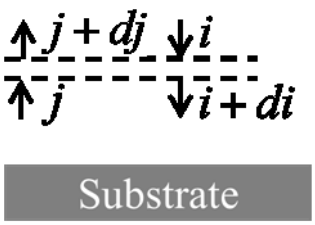

Fig. 2-2 Kubelka-Munk theory

In Kubelka-Munk theory, as the direction of movement, just two direction of upward and downward is considered. Assuming a virtual layer of infinitesimal thickness dx, the light flows of downward and upward as i and j, and the variations of the light flows as di and dj (Fig. 2-2), the transport equation becomes:

$$\begin{cases} -di = -(S+K)idx + Sjdx \\ dj = -(S+K)jdx + Sidx \end{cases} \tag{2-58}$$

Here, K and S are the absorption and scattering coefficients (which are different definition from the coefficients of other methods). Kubelka-Munk theory deriver several relationships starting from Eq. 2-58. Specifically, the following equation of the reflectance for thick coated film is frequently used.

$$\frac{K}{S}=\frac{\left(1-R_{\infty}\right)^{2}}{2R_{\infty}} \tag{2-59}$$

Here, R_{∞} is reflectance of the coated film when the film is infinitely thick.

2.3.4. Diffusion approximation

The content of this subsection is mainly based on Ref. 18.

Two assumptions are made. Firstly, the scattering by a medium with scattering coefficient μ_s' and anisotropy coefficient g can be approximated with a medium with scattering coefficient $\mu_s' = \mu_s\left(1-g\right)$ and isotropic scattering. Secondly, fluence rate $\Psi(r)$ satisfies the following diffusion equation:

$$\nabla^{2}\Psi\left(r\right)-\frac{\mu_a}{D}\Psi\left(r\right)=-\frac{S_0\left(r\right)}{D}+3\nabla\cdot S_1\left(r\right). \tag{2-60}$$

The equation can be derived from Boltzmann radiative transport equation under some assumptions for simplification [21]. Here, $S_0(r)$ and $S_1(r)$ are zeroth and first order source term, and given by the following equations:

$$S_0\left(x\right)=\int_{4\pi} S\left(x,\vec{\omega}\right)d\omega \quad , \quad S_1\left(x\right)=\int_{4\pi} S\left(x,\vec{\omega}\right)\vec{\omega}\ d\omega, \tag{2-61}$$

when S is the source. D is given by $D=1/\left[3\left(\mu_a+\mu_s\right)\right]$.

The boundary condition of two semi-infinite media with different refractive indices with a plane interface is given as the following equation:

$$\Psi\left(r\right)-2AD\hat{\Omega}_n\cdot\nabla\Psi\left(r\right)=0. \tag{2-62}$$

Here, A is the value related to the reflection at the interface, and given by the following equation:

$$A = \frac{2/(1-R_0)-1+|\cos\theta_c|^3}{1-|\cos\theta_c|^2}. \tag{2-63}$$

Here, θ_c is the critical angle, and $R_0 = \left[(n_{rel}-1)/(n_{rel}+1)\right]^2$, where n_{rel} is the relative refractive index. Furthermore, A is approximated by the following equations:

$$A = (1+r_d)/(1-r_d) \tag{2-64}$$

Here,

$$r_d = -1.440n_{rel}^{-2} + 0.710n_{rel}^{-1} + 0.668 + 0.0636n_{rel}. \tag{2-65}$$

According to the boundary condition, Ψ becomes zero on the plane $2AD$ above the interface with the first order approximation. Here, mirror method is utilized. The field can be expressed with sources and image sources where sources and image sources are placed symmetrically to the plane at $2AD$ above the interface. Assuming z-axis is the symmetrical axis, the fluence of a point source at $(\rho, z)=(0, z_0)$ is given by the following equation:

$$\Psi(\rho, z_0) = \frac{1}{4\pi D}\frac{\exp(-\mu_{eff} r_1)}{r_1} \tag{2-66}$$

Here, $\rho^2 = x^2 + y^2$ and $r_1 = \sqrt{(z-z_0)^2+\rho^2}$. When a point source and an image source is placed, the fluence becomes as the following:

$$\Psi(\rho, z_0) = \frac{1}{4\pi D}\left(\frac{\exp(-\mu_{eff} r_1)}{r_1} - \frac{\exp(-\mu_{eff} r_2)}{r_2}\right), \tag{2-67}$$

Here, $r_2 = \sqrt{(z+z_0+2z_b)^2+\rho^2}$ where $z_b = 2AD$.

We are interested in the photon current which exit from an object at z=0, which is given as:

$$R(\rho) = -D\nabla\Psi(\rho, z)\big|_{z=0}. \tag{2-68}$$

Under an arbitral distribution of point sources, the solution is very complex. For the simplicity, when point sources are represented by one point source whose depth is $z_0=1/\mu_t$ (mean free path), the photon current becomes:

$$R(\rho) = \frac{a'}{4\pi}\left[\frac{1}{\mu_1'}\left(\mu_{eff} + \frac{1}{r_1}\right)\frac{e^{-\mu_{eff} r_1}}{r_1^2} + \left(\frac{1}{\mu_1'} + 2z_b\right)\left(\mu_{eff} + \frac{1}{r_2}\right)\frac{e^{-\mu_{eff} r_1}}{r_2^2}\right]. \tag{2-69}$$

Moreover, integrating over the whole interface, reflectance in total is derived and the equation is the following:

$$R_d = \frac{a'}{2}\left(1 + \exp\left(-\frac{4}{3}A\sqrt{3(1-a')}\right)\right)\exp\left(-\sqrt{3(1-a')}\right). \tag{2-70}$$

Here, each parameters are given by the following equations.

$$a' = \mu_s' \Big/ \left(\mu_a + \mu_s'\right), \tag{2-71}$$

$$\mu_{eff} = \sqrt{3\mu_a\left(\mu_a + \mu_s\right)}. \tag{2-72}$$

For good approximation, μ_s' should be greater than μ_a enough. In addition, the approximation does not hold at around the incident point where the number of scattering of reflected light is small.

2.3.5. Monte Carlo simulation (MCS)

Monte Carlo simulation (MCS) is used as the most rigorous method to simulate the reflection from medium with scattering and absorption. In general, MCS stands for the method to derive physical quantities statistically after a number of numerical trials, whose base physical phenomena are stochastically generated. In the case of light scattering, a number of photons are generated and traced in a medium stochastically according to the

scattering and absorbing powers of the medium. Then physical quantities such as reflectance and transmittance are calculated statistically. MCS is often recognized as the correct solution, because the model replicates actual light movement faithfully.

The following is the explanation of MCS according to the implementation of MCML [5]. MCML is a program for MCS for multi layered model. The source code is distributed as an open source, and the function can be extended. The program is recognized as de facto standard for MCS.

In MCS, the motions of photons are defined by random numbers. Random number is generated uniformly in usual, however, distributions of physical statistical quantities are not usually uniform. The method to transform uniform random numbers into random numbers with an arbitral probability distribution is as follows. Assume a certain physical quantity χ is chosen with the probability $p(\chi)$ between [a, b]. At this time, $F(\chi_0)=\int_{\chi=a}^{\chi_0} p(\chi)d\chi$ is distributed between [0, 1]. Therefore, random number of an arbitral probability distribution $p(\chi)$ can be generated from a uniform random number ξ, by deriving χ that satisfies $F(\chi)=\xi$. In the case of MCS, exponential distribution is often arise. For $p(s)=\mu_t \exp(-\mu_t s)$, s is derived from uniform random number ξ with $s=-\ln(\xi)/\mu_t$. Here, $1-\xi$ is replaced with ξ to make the formula simpler.

A photon propagates medium numerically as following. Here, assume Cartesian coordinate. Set the incident point as origin, and the surface as x-y plane, and the depth direction as z-axis. First, a photon is generated. A photon has statuses of current position (x, y, z), traveling direction (u_x, u_y, u_z), and a weight W whose initial value is unity. Reflectance at surface R_{sp} is calculated with Fresnel equation and W become $W-R_{sp}$. Then, the photon goes to the inside of the model.

Then, the photon switches the direction, absorption and scattering, until W becomes lower than the designated threshold or the photon goes off the model. Initially, a step size is calculated. From uniform random number ξ, whose range is (0, 1), a step size is derived by the formula:

$$s = \frac{-\ln(\xi)}{\mu_{t1}}. \tag{2-73}$$

From the initial position (x, y, z), the photon move to ($x+u_x s$, $y+u_y s$, $z+u_z s$). After the movement, a certain ratio of the photon is absorbed. It is realized by subtracting $W\mu_a/\mu_t$ from W. Then, the photon turn the direction. The scattering follows Henyey-Greenstein function (Eq. 2-54). With a uniform random number ξ in a range of [0, 1],

$$\cos\theta = \begin{cases} \dfrac{1}{2g}\left\{1+g^2-\left[\dfrac{1-g^2}{1-g+2g\xi}\right]^2\right\} & if\ g>0, \\ 2\xi-1 & if\ g=0. \end{cases} \tag{2-74}$$

Azimuthal angle Ψ is derived from a uniform random number ξ with $\Psi = 2\pi\xi$. Then,

$$\begin{cases} u_x' = \dfrac{\sin\theta}{\sqrt{1-u_z^2}}\left(u_x u_z \cos\psi - u_y \sin\psi\right) + u_x \cos\theta \\ u_y' = \dfrac{\sin\theta}{\sqrt{1-u_z^2}}\left(u_y u_z \cos\psi - u_x \sin\psi\right) + u_y \cos\theta \\ u_z' = -\sin\theta\cos\psi\sqrt{1-u_z^2} + u_z \sin\theta. \end{cases} \tag{2-75}$$

In the case u_z is close to 1, the following equations are used.

$$\begin{cases} u_x' = \sin\theta\cos\psi \\ u_y' = \sin\theta\sin\psi \\ u_z' = \mathrm{SIGN}(\mu_z)\sin\theta. \end{cases} \tag{2-76}$$

If the step size s (the path length is s/μ_{t1}) is long so that the photon pass across the interface of layers, make the photon step back to the cross section of the interface and the

trajectory, and the new step size set to $s - s_1$ assuming the photon pass through layer 1 to 2 and s_1 is the step size in the layer 1. Then, the next move is defined whether reflection or transmission stochastically. If the next move of the photon is defined to transmission, the step size is multiplied by μ_{t1}/μ_{t2} and the moving direction is changed (refracted).

The termination of tracing is as following. If the weight becomes small, the contribution to the physical quantities also becomes small, so that the calculation becomes ineffective. However, the termination must be treated appropriately, or the errors are accumulated and become non-negligible. If the W becomes less than a predetermined threshold, the photon is basically terminated but survive with the probability $1/m$ assuming m is a certain integer. W of a survived photon is multiplied by m, and the propagation continues.

In the middle of the trace of a photon and after, physical states are recorded, counting on a respective element of histograms. After the calculation for a given number of photons, physical quantities will be derived.

3. Reduction of shading-derived artifacts in skin chromophore imaging

3.1. Introduction

The concentrations of chromophores in skin provide important information for making a diagnosis, and images can provide additional information, such as the size of a lesion, that aid visual understanding. Therefore, many studies have been conducted to evaluate the concentration of chromophores [26, 31, 40, 78, 86, 87], and some of these studies discuss imaging, in which visible light spectroscopy is usually used to achieve high spatial resolution [37-39, 41-43, 88]. Multiple regression analysis based on the Beer-Lambert (B-L) [26] law is a simple way to correlate the chromophore concentrations with the reflectance of skin. The B-L law has been applied to the three-layer skin model of epidermis, dermis, and fat, with the assumptions that no scattering occurs in the epidermis or dermis and no wavelength dependency exists in the reflectance from the fat layer [26]. With these assumptions, the optical path length becomes constant and does not depend on wavelength. Therefore, in accordance with the B-L law, the absorbance (the logarithm of the inverse of the reflectance) can be expressed as a linear combination of the absorption coefficient spectrums of melanin, oxygenated hemoglobin, and

deoxygenated hemoglobin, and a constant term. The constant term comes from the reflectance of the fat layer. The regression analysis uses the absorbance spectrum as a response variable and the extinction coefficients of each chromophore as the predictor variables. Although the implementation is easy, the model is quite different from actual conditions, and it leads to inconsistencies between the actual and the fitted spectrums [31, 35, 36].

To improve the estimation, the modified B-L method has been introduced [31, 86]. Although the method is based on the B-L law, the optical path length is allowed to be wavelength dependent. This added degree of freedom allows a part of the scattering effect to be included, and it improves the coefficient of determination [31, 86]. In this method, as the predictor variables in the multiple regression analysis, the product of each absorption coefficient and the wavelength-dependent path length was used. However, the method assumes that the optical path length is independent of the concentrations of chromophores, and thus the results are still different from measurements of the actual phenomenon. Neither the nonlinearity between the concentration and the absorbance nor the cross-talk between the chromophores have been taken into account [35, 36, 40].

In order to fully account for the effect of scattering in the estimation of chromophore concentrations, several methods have been considered; these include methods based on random work theory [37], Kubelka-Munk theory [38], a support vector machine [39], and an empirical method aided by a Monte Carlo simulation (MCS) [40, 41]. Although scattering effects are fully considered in these methods, the methods are susceptible to shading-derived errors caused by the incomplete estimation of the irradiance [37-39]. This is a serious problem for the visual understanding and quantitative evaluation of the chromophore imaging. Here, ‘shading’ is the spatial distribution of irradiance.

Shading results from the incident angle of the light, the spectral radiant intensity of the light source, and the distance from the light source. If the actual irradiance on the surface of a subject is lower than the estimate, then the apparent reflectance decreases and the chromophore concentrations will be overestimated; this tends to occur on the fringe areas of the subject. Therefore, for a precise calibration of reflectance, besides the radiant intensity distribution of the light, the shape of the subject also must be assessed (unless the areas of interest are limited to small, flat areas in which the irradiance can be fully assessed) [40]. The problem with shading is common among methods that consider nonlinear scattering effects in imaging [42].

Several studies have attempted to correct for the shading effect. In these studies, the shape of each subject was measured [43, 44] or the curvature effect was otherwise extracted [37] and taken into account. However, these approaches require hardware modifications and additional measurements or else assumptions about the shapes of the samples.

Incidentally, in the simple and modified B-L methods, in which the absorbance is expressed as a linear combination of each chromophore component with a constant term, the shading-derived error is not observed in the images of chromophore concentrations. The effect of surface curvature is proportional to irradiance, and in the absorbance, it is a constant term, independent of wavelength. Therefore, the effect of surface curvature will appear only in the constant term and will not appear in the image of the chromophore concentrations.

In order to fully account for the scattering effect and to reduce the shading-derived artifact, we propose an approach based on the MCS-aided empirical method [40, 41]. In this method, the simple B-L method is used to derive multiple regression coefficients

related to the concentrations of melanin, oxygenated hemoglobin and deoxygenated hemoglobin. Then, the multiple regression coefficients are converted to the concentrations of melanin and total hemoglobin (sum of oxygenated and deoxygenated hemoglobin) using compensation formulae (CF), which are derived from the diffuse reflectance spectra of human skin, numerically calculated in advance by a MCS [5]. In the previous method [40, 41], the constant term of the multiple regression coefficients, as well as the regression coefficients of melanin and total hemoglobin, were used in the CFs. Although the use of the constant term is important for estimating the absolute values of chromophore concentrations, it can cause the shading-derived error in reflectance that results in an overestimation of the chromophore concentrations. Since the shading-derived error is concentrated into the constant term during the first step of the multiple regression analysis, selecting the optimal combination of multiple regression coefficients has the potential to satisfy both of the requirements. *In vivo* experiments with a human forearm were performed to confirm the usefulness of the proposed approach for improving the robustness of the method against the estimation error in the irradiance.

3.2. Materials and methods

3.2.1. Outline of the method

According to the B-L law, the absorbance spectrum $A(\lambda)$, which is derived from the reflectance spectrum $R(\lambda)$ as $A(\lambda) = \log(1/R(\lambda))$, can be approximated with the following formula [40, 41]:

$$A(\lambda) = a_m \cdot \varepsilon_m(\lambda) + a_{oh} \cdot \varepsilon_{oh}(\lambda) + a_{dh} \cdot \varepsilon_{dh}(\lambda) + a_0 . \quad (3\text{-}1)$$

Here, melanin, oxygenated hemoglobin, and deoxygenated hemoglobin are assumed to

be the main contributors to the absorption of light in skin. In Eq. 3-1, λ represents the wavelength; ε_m, ε_{oh}, and ε_{dh} are the spectral absorption coefficients of melanin, oxygenated hemoglobin, and deoxygenated hemoglobin, respectively; a_m, a_{oh}, and a_{dh} are the respective concentration-related values; and a_0 is the constant term. Eq. 3-1 can be calculated by a multiple regression analysis (MRA1) in which A represents the response variables, and ε_m, ε_{oh}, and ε_{dh} are the predictor variables. Then, a_m, a_{oh}, a_{dh}, and a_0 are derived as the multiple regression coefficients.

Our proposed method obtains prior estimates of the relationship between the MRA1 regression coefficients and the chromophore concentrations of the MCS. With the MCS, a spectrum can be calculated from a given set of chromophore concentrations according to the skin model described in Sec. 3.2.2. Then, a set of regression coefficients can be derived from the spectrum using MRA1. By calculating regression coefficients for several sets of concentrations, sets of regression coefficients can be associated with particular chromophore concentrations. Polynomial, exponential, or logarithmic functions, or a combination of these functions, can be used as the form of the CFs. In this study, we used a polynomial form because it can be solved analytically by multiple regression analysis. To derive the CFs for calculating the concentrations from the regression coefficients, another multiple regression analysis (MRA2) was used. Here, we considered the original concentrations from the MCS to be the response variables and their products with the regression coefficients from MRA1 to be the predictor variables; we will call this MRA2. In symbolic form, MRA2 is expressed as

$$c_i = \vec{b}_i \cdot \vec{a} \quad , \tag{3-2}$$

where i represents m (for melanin) or th (for hemoglobin). Here, c_i is the estimated concentration of the respective chromophore, $\vec{a}$ is a vector whose elements are the

regression coefficients from MRA1 and their higher-order terms, and $\vec{b}_i$ is the vector converting the regression coefficients to concentrations.

3.2.2. Correlating the multiple regression coefficient with the chromophore concentrations

We used the same skin model and the same parameters that were used in the previous studies [40, 41], as follows: a two-layered model of the epidermis with uniform melanin and an underlying dermis with uniform oxygenated and deoxygenated hemoglobin was used; the thicknesses of the epidermis and dermis were 0.06 mm and 4.94 mm, respectively. The refractive indices n were assumed to be 1.4, independent of wavelength and layer. The refractive index of the external area was set to 1. The absorption coefficients of the epidermis and dermis were assumed to be $\varepsilon_m(\lambda)\cdot C_m$ and $\varepsilon_{oh}(\lambda)\cdot C_{oh}+\varepsilon_{dh}(\lambda)\cdot C_{dh}$, respectively. Here, C_m, C_{oh}, and C_{dh} are the concentrations of melanin, oxygenated hemoglobin, and deoxygenated hemoglobin in each layer. For $\varepsilon_m(\lambda)$, we used the average absorption coefficient of a monomer melanosome with a concentration of 1 mole/liter; this was approximated as $6.6\times10^{11}\times\lambda^{-3.33}$, where the unit of λ is nm [89]. For ε_{oh} and ε_{dh}, we used the extinction coefficients of oxygenated and deoxygenated hemoglobin, respectively, converted to the concentration of 45 hematocrit in blood [90]. The scales of C_m, C_{oh}, and C_{dh} were the ratios of the concentrations to those under which $\varepsilon_m(\lambda)$, $\varepsilon_{oh}(\lambda)$, and $\varepsilon_{dh}(\lambda)$, respectively, were derived. To characterize the scattering, a reduced scattering coefficient $\mu_s'(\lambda)$ is required; this is derived from $\mu_s'(\lambda)=\mu_s(\lambda)\times(1-g)$, using the scattering coefficient $\mu_s(\lambda)$ and anisotropy g, which are the primitive parameters of scattering [91, 92]. The value of $\mu_s'(\lambda)$ for both the epidermis and dermis was $2\times10^5\times\lambda^{-1.5}+2\times10^{12}\times\lambda^{-4}$; the first term represents Mie scattering, the

second one represents Rayleigh scattering [91-93], and the unit of λ is nm.

The MCS (using the program MCML [5]) was used to derive the spectra for various concentrations of chromophores; a_m, a_{oh}, a_{dh}, and a_0 were then calculated using MRA1. The calculated melanin concentrations C_m were set from 1% to 10% in 1% intervals, the hemoglobin concentration C_{th} (= C_{oh} + C_{dh}) was set from 0.2% to 1% in 0.2% intervals, and the oxygen saturation C_{StO2} (= C_{oh}/C_{th}) was set from 0% to 100% in 20% intervals. The wavelength was set from 500 nm to 600 nm in 20 nm intervals, and the number of photons under a single condition was 10^5 [94]. From the MCS calculations under the various conditions, a total of 300 spectra were generated. In the MCS, the incident angle was set to 0° and, for statistical accuracy, the reflectance was integrated over the entire reflected angle. Although the outgoing angle was not the same as in the actual measurement condition (see Sec. 2.6), it is appropriate if Lambertian reflection is assumed; it gives a first-order approximation of internal reflection [95]. For each combination of (C_m ,C_{oh} ,C_{dh}), after the reflectance spectra were converted to absorbance spectra, a_m, a_{oh}, a_{dh}, and a_0 were calculated using MRA1.

3.2.3. Shading effect

Shading has an effect on the results of MRA1, and thus, consequently, on the estimated chromophore concentrations. Assuming Lambertian reflection and using θ_i to denote the angle between the surface and the incoming light, the irradiance is $\cos\theta_i$ times that of normal incidence, independent of wavelength. Therefore, the apparent reflectance can be expressed as $R'=R\times\cos\theta_i$, where the actual reflectance is defined as R. Also, the apparent absorbance A' can be expressed as $A'=\log(1/R') = A+\log(1/\cos\theta_i)$, where the actual absorbance is $A=\log(1/R)$. Since the second term is independent of the

wavelength, a_0 becomes $\log(1/\cos\theta_i)$ larger than it is in the case of normal incidence [42].

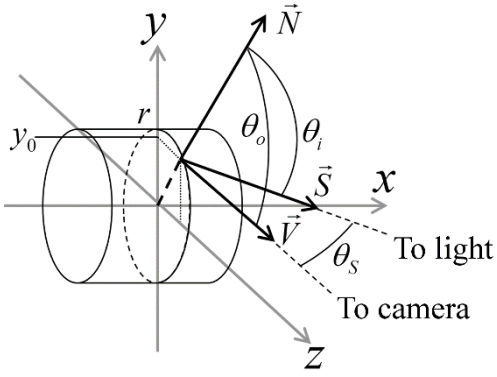

Fig. 3-1 Notation of positional and angular relationships for a point on a cylindrical subject in relation to a light source and a camera. Each symbol represents $\vec{S}$: light vector $\vec{N}$,: normal vector, $\vec{V}$: viewing vector, θ_i: incident angle, θ_o: viewing angle, θ_S: angle between $\vec{S}$ and $\vec{V}$, r: radius of the cylindrical subject; (x_0, y_0): coordinate value of a point on the subject.

We assumed that a light, a camera, and a cylindrical subject of radius r are arranged as follows. The cylinder is placed so that the center is at the origin and the axis of symmetry lies along the x-axis, the camera lies on the z-axis, and the light source is in the zx-plane (Fig. 3-1). The light vector $\vec{S}$ can be expressed as $(\sin\theta_s, 0, \cos\theta_s)$ at any point on the subject. Similarly, the normal vector $\vec{N}$ at the point (x_0, y_0) is $\left(0, y_0/r, \sqrt{1-y_0^2/r^2}\right)$. Therefore, the incident angle (the angle between $\vec{S}$ and $\vec{N}$) is $\cos^{-1}\left(\cos\theta_S \cdot \sqrt{1-y_0^2/r^2}\right)$. Under this arrangement, the incident angle depends on the y-coordinate and increases with increasing distance from the x-axis, so a_0 also increases. The intensity of the reflected light is expected to depend less on the viewing

angle θ_o than on the incident angle, because, in the case of Lambertian reflection [95], the observation point does not affect the intensity of the reflected light.

3.2.4. Formula of the relationship between the multiple regression coefficients and the chromophore concentrations

From the description in Sec. 3.2.3, for MRA1, we assumed that the shading effect would appear mainly in the a_0. Therefore, when using the regression coefficients of MRA1 to estimate the chromophore concentrations, removing a_0 from the CFs will eliminate the shading effect.

Note that the form of the polynomial equation is the key factor of our method. Removing a_0 from the CFs will reduce the estimated errors in the chromophore concentrations that are due to shading-derived errors in the reflectance. However, this will decrease the accuracy of the CFs, because a_0 also includes information related to the concentration of each chromophore. To compensate for the absence of a_0, we separate a_{th} into a_{oh} and a_{dh}. To determine the appropriate CFs, we considered using the following three types of $\vec{a}$ in Eq. 3-2 and examined each with various choices for the regression coefficients.

$$\vec{a}^{CF1} = \left(1 \quad a_m \quad a_{th} \quad a_0 \quad a_m^2 \quad a_{th}^2 \quad a_0^2 \quad a_m \cdot a_{th} \quad a_{th} \cdot a_0 \quad a_0 \cdot a_m\right)^T . \tag{3-3}$$

$$\vec{a}^{CF2} = \left(1 \quad a_m \quad a_{th} \quad a_m^2 \quad a_{th}^2 \quad a_m \cdot a_{th} \quad a_m^3 \quad a_{th}^3 \quad a_m \cdot a_{th}^2 \quad a_m^2 \cdot a_{th}\right)^T . \tag{3-4}$$

$$\vec{a}^{CF3} = \left(1 \quad a_m \quad a_{oh} \quad a_{dh} \quad a_m^2 \quad a_{oh}^2 \quad a_{dh}^2 \quad a_m \cdot a_{oh} \quad a_{oh} \cdot a_{dh} \quad a_{dh} \cdot a_m\right)^T . \tag{3-5}$$

Here, a_{th} is defined as the sum of a_{oh} and a_{dh}, and T represents the transpose. In Eq. 3-3, a_m, a_{th}, and a_0 were used in the CFs, and the choice of the regression coefficient was the

same as in the previous studies [40, 41]. In Eq. 3-4, a_m and a_{th} were used in the CFs, but a_0 was not used. In Eq. 3-5, a_{oh} and a_{dh} were used instead of a_{th}. To adjust the degrees of freedom between CF1, CF2, and CF3, the maximum degree of CF2 was set to three, and those of CF1 and CF3 were set to two. In CF2 and CF3, in which a_0 was omitted, the artifact from shading was expected to be removed, due to the manifestation of the shading effect in the coefficient a_0 (see Sec. 3.2.3). In any of these CFs, the oxygen saturation a_{StO2} can be calculated as a_{oh}/a_{th}.

3.2.5. Experiments

3.2.5.1. Correlation between estimated and expected value of chromophore concentrations

The chromophore concentrations were estimated with each CF from the spectrum made by the MCS and compared with the inputs of the MCS, which were the expected values. For this calculation, the skin model described in Sec. 3.2.2 (the same skin model parameters used for MRA2) was used.

3.2.5.2. Measurement of forearm skin

The right forearms of Japanese males (N=5) in their 20s to 40s were measured with the measuring device described in Sec. 3.2.6. For each subject, the forearm was placed horizontally and images were captured. This was done for two different postures: the inner forearm facing front (angle 1) and facing approximately 45° upward (angle 2). To correlate the positions on the forearm, several points were marked in a reticular pattern at a distance of 2 cm from neighboring points. After performing MRA1, the chromophore concentrations were calculated as images by using the CFs.

The averaged values of the chromophore concentrations in a 10 × 10 pixel (2.5 mm

× 2.5 mm when the surface faces front) area at the middle of horizontally neighboring marks were calculated for each CF.

3.2.6. Measuring Device

The following apparatus was prepared (Fig. 3-2). A camera (CV-M7+CL; jAi, Yokohama, Japan) was set in front of the subject. A liquid-crystal wavelength-tunable filter (VariSpec; CRi, Hopkinton, MA, USA; full width at half maximum: 10 nm) and a polarizer were set in front of the camera. Two halogen lights were set at the left and right sides of the camera in such a way that the angle between the camera and the lights was 30°. An infrared cut filter and a polarizer, which was set to be orthogonal to the polarizer in front of the camera, were set between each light source and the subject; this was done to reduce the specular reflection from the skin surface [42].

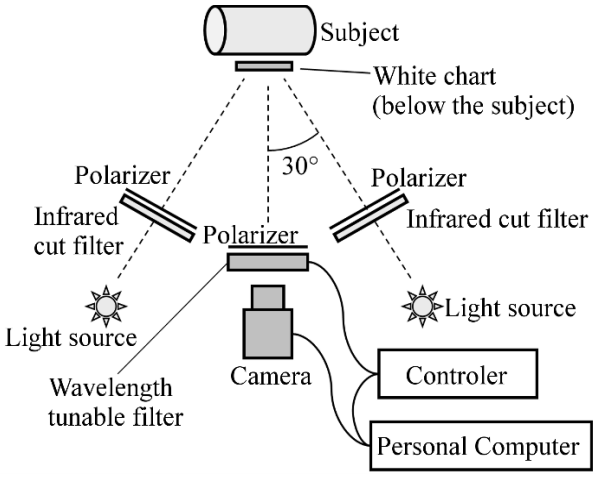

Fig. 3-2 Schematic of the measuring system.

Images were captured using a personal computer and by varying the transparent wavelength of the VariSpec. The resolution of the camera was 4 pixel/mm on a subject facing frontwards, and the pixel depth was 10 bits. The transparent wavelength was set from 500 nm to 600 nm, with an interval of 20 nm. The measurement time was about

10 s in total. Although we used a color camera, we used only the green channel. For calibration, we captured images of a gray card besides images of subjects, and the pixel values were converted to reflectance in a pixel-by-pixel manner. In the calibration, the pixel value of the white chart was also used, and it was set below the subject. The reflectance can be derived from this calibration if the surface of interest is perpendicular to the line of sight. However, if the surface of interest is not perpendicular to the line of sight, the shading-derived error in the reflectance, i.e., the calibration error in the reflectance, will be increased according to $\cos\theta_i$, as shown in Fig. 3-1.

3.2.7. Statistics

3.2.7.1. Correlation between estimated and expected value of chromophore concentrations

In the statistical analysis of the estimated and expected values of chromophore concentrations from the MCS, the standard deviation σ of each condition was defined as

$$\sigma_i^2 = \sum_{j=1}^{n} \left(c_{i,j} - C_{i,j} \right)^2 \Big/ (n-1). \tag{3-6}$$

Here, i is m (melanin) or th (hemoglobin), n is the number of data points, j indicates a particular data point, and $c_{i,j}$ and $C_{i,j}$ are, respectively, the estimated and expected values.

3.2.7.2. Measurement of forearm skin

In the statistical analysis of forearm skin, the variance V was determined as

$$V_{i,j} = (c_i \text{ of angle 1 at } j\text{-th area}) - (c_i \text{ of angle 2 at } j\text{-th area}). \tag{3-7}$$

Here, i is m (melanin) or th (hemoglobin) and c_i is the measured chromophore concentration. Assuming that the dispersion of the difference between c_i and the real value is equal to half of the dispersion of V, the standard deviation σ_i of the difference

between the real and measured values of c_i can be derived from the following equation:

$$\sigma_i^2 = \left(\sum_{j=1}^{n} V_{i,j}^{\ 2} \Big/ (n-1) \right) \Big/ 2 . \tag{3-8}$$

where n is the number of measured areas.

3.3. Results

3.3.1. Correlation between estimated and expected value of chromophore concentrations

For CF1, CF2, and CF3, the relationships between the original C_i and the estimated c_i (i=m, th) are shown in Fig. 3-3. The σ were 0.025, 0.481, and 0.084 for the melanin concentration estimated with CF1, CF2, and CF3, respectively, and 0.008, 0.092, and 0.016 for the hemoglobin concentration measured with CF1, CF2, and CF3, respectively. The errors increased in the order of CF1, CF3, and CF2.

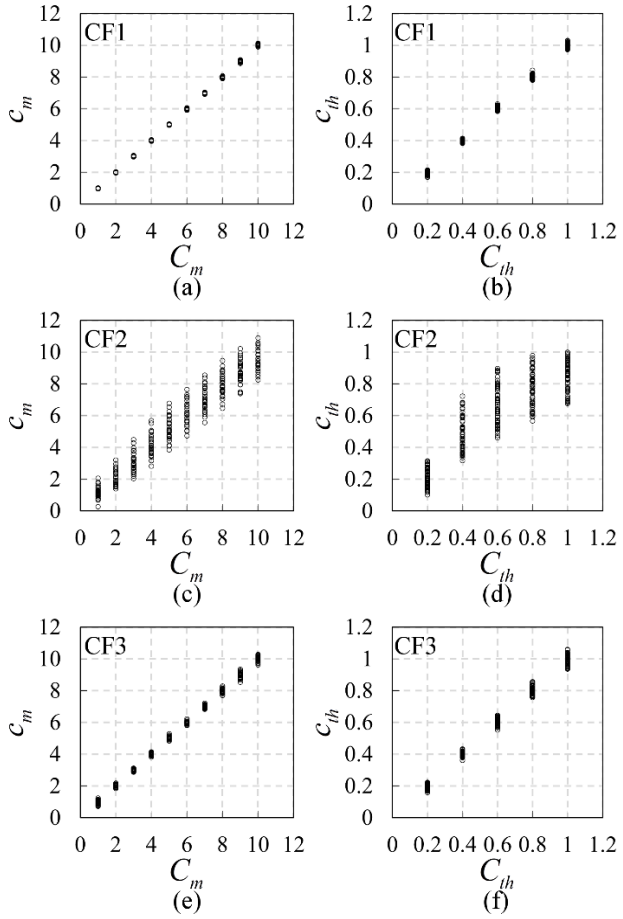

Fig. 3-3 Correlations between the original and the estimated values of (a) melanin and (b) hemoglobin, using CF1; (c) melanin and (d) hemoglobin, using CF2; and (e) melanin and (f) hemoglobin, using CF3. Horizontal axis: original values; vertical axis: estimated values. The unit of the horizontal and vertical axes is %.

3.3.2. Measurement of forearm skin

Images of the inner forearm from sets of spectra images are shown in Fig. 3-4, and Fig. 3-5 shows the images of the regression coefficients of the framed area in Fig. 3-4a. While the systematic variation from the center to the fringe (upper and lower sides in the pictures) cannot be found in a_m (Fig. 3-5a) or a_{th} (Fig. 3-5b), the value of a_0 became greater at the fringe (Fig. 3-5e). In a_{oh} (Fig. 3-5c) and a_{dh} (Fig. 3-5d), the values became

slightly larger and smaller at the edges, respectively, but the degree to which this happens is smaller than it was for a_0. The value of a_{StO2} was affected by the trend of a_{oh} and a_{dh} and decreased slightly at the fringe (Fig. 3-5c). The average and standard deviation of each regression coefficient of the sites A, B, C, and D in Fig. 3-4a were calculated, and the values were as follows: $a_m = (2.1\pm0.2)\times10^{-4}$; $a_{th} = (1.6\pm0.1)\times10^{-6}$; $a_{oh} = (8.5\pm0.9)\times10^{-7}$; $a_{dh} = (7.6\pm1.1)\times10^{-7}$; $a_0 = (2.2\pm0.2)\times10^{-1}$; and $a_{StO2} = (55\pm5)\%$.

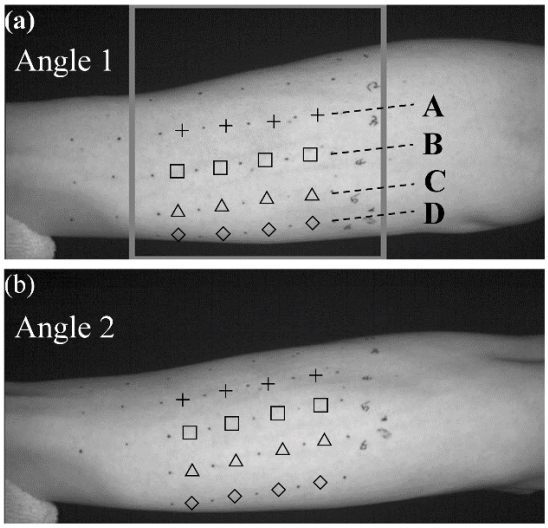

Fig. 3-4 Representative example of measured images (appearance) from different angles. The inner side of the forearm faced (a) straight or (b) upward. The hand is to the left side. To correlate the positions, points were marked in a reticular pattern. The symbols drawn on the pictures are the measured points for Fig. 3-8. The framed area in (a) is the area shown in Fig. 3-5 and Fig. 3-6.

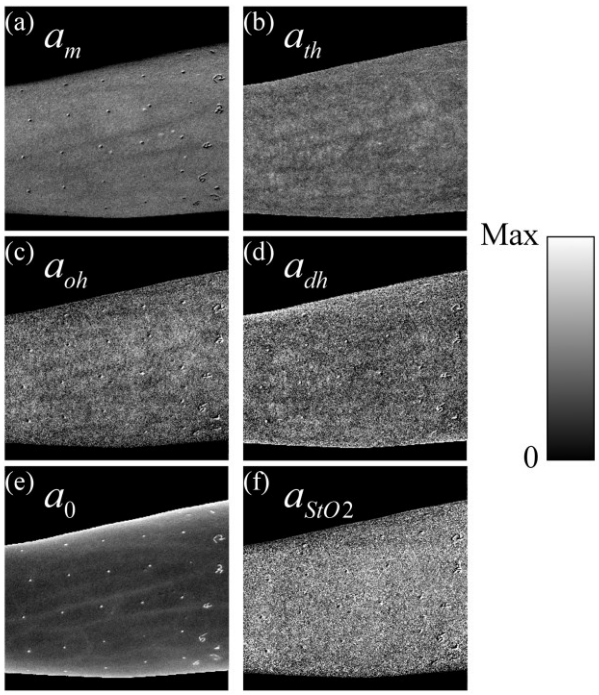

Fig. 3-5 Representative example of images of the multiple regression coefficients: (a) a_m; (b) a_{th} (=a_{oh} + a_{dh}); (c) a_{oh}; (d) a_{dh}; (e) a_0; and (f) a_{StO2} (=a_{oh}/a_{th}). The area of the images is the area surrounded by a border in Fig. 3-4a. The background is masked in black. The value of each regression coefficient corresponds to the brightness. The lower limit is zero for all images, and the upper limit ("Max") is 5×10^{-4} for a_m, 4×10^{-6} for a_{th}, 1×10^{-6} for a_{oh}, 1×10^{-6} for a_{dh}, 1 for a_0, and 100% for a_{StO2}. The reticular pattern is made up of points marked on the skin, and it can be clearly seen in (e).

Next, the chromophore concentrations were estimated with each CF. Fig. 3-6 presents the images of a representative example of these. In CF1, the values of c_m and c_{th} increased from the center to the fringe, but in CF3, no such tendency could be observed. This tendency is also seen in Fig. 3-6. From the cross-section, the values of CF3 near the center were close to those of CF1 (Fig. 3-7a, b). On the other hand, the fluctuations of CF3 are larger than those of CF1. In CF2, also, a systematic variation

could not be found, but the fluctuations were larger than those of CF3. The differences between these and the values with CF1 were especially observable in c_{th} (Fig. 3-7b). The averages and standard deviations of the magnified area in Fig. 3-7 were 5.7±0.6%, 4.7±1.5%, and 5.1±1.2% for melanin with CF1, CF2, and CF3, respectively, and 0.19±0.05%, 0.10±0.08%, and 0.18±0.05% for hemoglobin with CF1, CF2, and CF3, respectively.

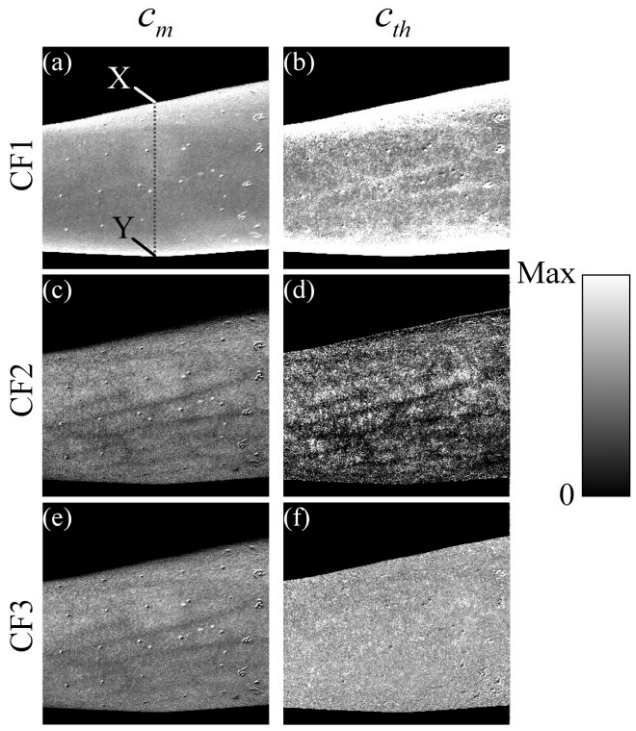

Fig. 3-6 Estimated c_m and c_{th} with each CF. (a)–(b) with CF1: (a) c_m and (b) c_{th}; (c)–(d) with CF2: (c) c_m and (d) c_{th}; (e)–(f) with CF3: (e) c_m and (f) c_{th}. The value of each estimated concentration corresponds to the brightness; the lower limit is zero for all images, and the upper limit ("Max") is 10% and 0.25% for the images of c_m and c_{th}, respectively. The dotted line and the characters "X" and "Y" in (a) represent the cross-section and ends represented in Fig. 3-7. The background is masked in black. The reticular pattern is made up of points marked on the skin.

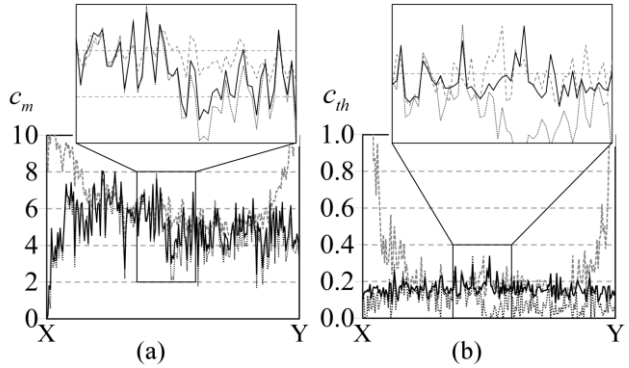

Fig. 3-7 Cross-sections of the estimated (a) c_m and (b) c_{th}, with CF1, CF2, and CF3. CF1: gray broken lines, CF2: dotted lines, CF3: solid black lines. The plots shown above are the magnified figures of the framed areas. The cross-sections were taken along the dotted lines in Fig. 3-6a, and the sides X and Y correspond to the positions noted in Fig. 3-6a. The unit of the vertical axes is %.

Finally, c_m and c_{th} estimated from different angles at the same site were compared, and the results from a representative example are shown in Fig. 3-8. The differences between the values of different angles at each position with CF3 were smaller than those with CF1. The values of σ for the representative example for melanin and hemoglobin (Fig. 3-8) were, respectively, 1.8% and 0.15% for CF1, 0.3% and 0.02% for CF2, and 0.3% and 0.01% for CF3. The values of σ for melanin and hemoglobin for all sites and all subjects were, respectively, 1.3% and 0.15% for CF1, 0.4% and 0.02% for CF2, and 0.3% and 0.02% for CF3. Fig. 3-9 shows a plot of c_m and c_{th} for all subjects and all points for CF3.

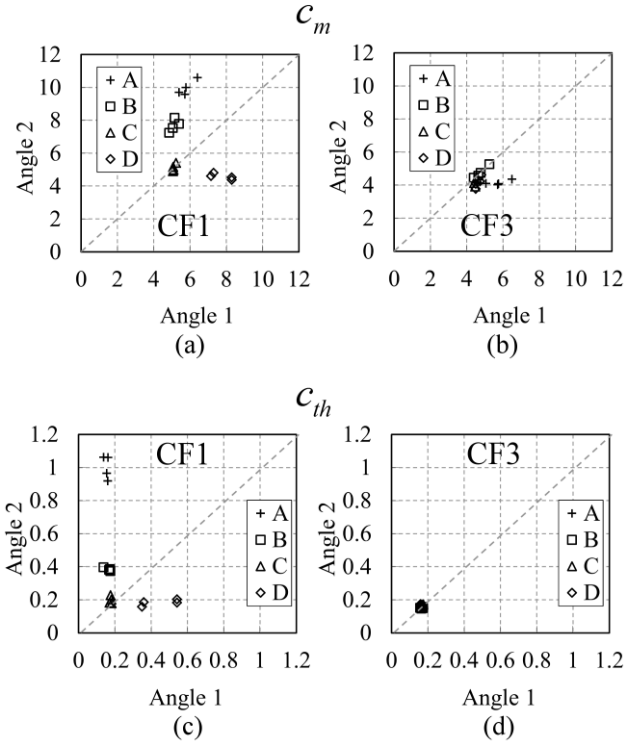

Fig. 3-8 Correlation between the estimates from different angles (angles 1 and 2) of the melanin and the hemoglobin concentrations at each position of the representative example (same subject as in Fig. 3-4). (a)–(b): c_m calculated with (a) CF1 and (b) CF3; (c)–(d): c_{th} calculated with (c) CF1 and (d) CF3. The symbols and legend (A to D) are the same as those used in Fig. 3-4. The unit of the horizontal and vertical axes is %.

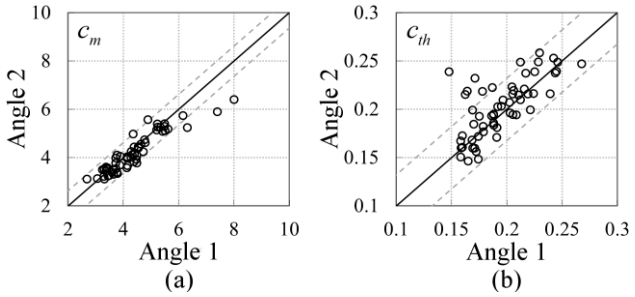

Fig. 3-9 Correlation between the estimates from different angles (angles 1 and 2) of the melanin and the hemoglobin concentrations at each position for all subjects. (a): c_m; (b): c_{th} calculated with CF3. The diagonal solid line represents $y=x$, and the diagonal gray broken line represents $y=x\pm1.96\sigma$, which is the 95% confidence interval assuming the V follows a Gaussian distribution. The unit of the horizontal and vertical axes is %.

3.4. Discussion

Under the condition that the forearm was set horizontally and the lights were set at the left and right sides of the camera, the incident angle at the upper and lower sides were greater than that at the center. Therefore, the irradiance at the surface became smaller. As we expected (see Sec. 3.2.3), the shading effect appeared in the a_0 image (Fig. 3-5e), and became greater at the fringe. As a consequence, with CF1 (Fig. 3-6a, b), since the formula contains a_0 (Fig. 3-5e), the effect of the shading can be seen in the estimation of chromophore concentrations. This tendency seems to be larger for hemoglobin than for melanin. With CF3 (Fig. 3-6e, f), which does not contain a_0, the artifact is hardly seen, as expected. The improvement is shown more clearly in Fig. 3-8. Each position on the subject should have the same chromophore concentrations even if the measurement angle is changed. Thus, the points plotted in Fig. 3-8 should be on the line $x=y$. Obviously, the points plotted for CF3 were closer to $x=y$ than those for CF1, which were

quantified with σ. From these results, we conclude that the estimation errors in the chromophore concentrations, that are due to the shading-derived error in the reflectance were greatly reduced by the proposed approach. With CF3, the σ were 0.3% and 0.02% for c_m and c_{th}, and the ranges of c_m and c_{th} were 3-6% and 0.15-0.25%, respectively (Fig. 3-9), which demonstrates that the ratio of the error to the chromophore concentrations is about 10%.

Near the center, where irradiance was evaluated correctly, CF3 estimated the same values, on average, as did CF1 (Fig. 3-7). In other words, CF3 is as accurate as CF1 when there is less of an effect of shading. Furthermore, the values are within the expected ranges of concentration: c_m, c_{th}, and a_{StO2} for the representative example were 5.0±0.7%, 0.17±0.01%, and 55±5%, respectively, which agrees with the average values for Japanese subjects, as reported in the literature [40, 93].

In the case of CF2 (Fig. 3-6c, d), although the shading effect was suppressed, the fluctuation was large. Moreover, the average value is very different from the value with CF1 near the center (Fig. 3-7). This tendency was notable for c_{th}. This probably came from the error between the expected and estimated chromophore concentrations, which can be seen in Fig. 3-3c, d.

Although in Sec. 3.2.2 we assumed Lambertian reflection for the angular dependency of reflection from skin as a precondition of the constancy of reflectance with varying outgoing angles, this precondition can be loosened. Lambertian reflection proved to be an inaccurate approximation for several real-world objects [95]. However, in the proposed method, to the extent that the angular dependency of the reflected light is proportional between wavelengths, the chromophore concentrations will not be affected by the viewing angle. This is because the multiplication of the reflectance by an

independent factor of the wavelength will be included in a_0 in the same way that the shading effect is included in a_0. From the fact that the variation from the center to the fringe does not explicitly appear in the multiple regression coefficients other than a_0 (Fig. 3-5), we infer that the loosened precondition is almost true when the viewing angle increases from the center to the fringe, as does the incident angle. Nonetheless, the penetration depth seems dependent in some way besides the shading effect on the incident angle and viewing angles. At the very edge of the forearm, a_{oh} and a_{dh} became slightly smaller and larger, respectively (Fig. 3-5c, d), which can be explained by a shallower penetration depth with a larger incident angle. The oxygen saturation in a shallower region is expected to be lower than that in a deeper region [96], which is the trend seen in the derived images.

There are some side effects from removing a_0 from the CFs, and these should be improved. First, although the fluctuations with CF3 were smaller than those with CF2, they were still larger than those with CF1 (Fig. 3-6, Fig. 3-7). We tried increasing the maximum degree of CF3 from two to three, but the fluctuations did not improve (not shown). The fluctuations are due directly to a_{oh} and a_{dh}, but did not appear in a_{th} (Fig. 3-5b). This indicates that the noise in a_{oh} and a_{dh} should be removed in order to reduce the noise in c_{th}. Next, the melanin images from CF3 show what seem to be veins (Fig. 3-6e). This comes from the a_m image (Fig. 3-5a), and the compensation did not seem to work well without a_0. Although the average values for CF3 were the same as those for CF1 (Fig. 3-7), this can create a serious problem in visual understanding. To reduce these problems, although the regression coefficients for the MRA1 will be converted to chromophore concentrations with CFs, maximizing the accuracy of MRA1 may be effective in terms of the propagation of errors. This means that the more linear the

relationship between the regression coefficients of MRA1 and the respective chromophore concentrations is, the smaller the estimation error will become. Therefore, for MRA1, employing the modified B-L method instead of the simple B-L method may be effective, because this will improve the correlation between the concentration and the respective regression coefficients of MRA1.

This technique for reducing the shading-derived error does not require any measurements or assumptions about the shape of the subjects and has no limitations as to skin type. In addition, the method is robust against the angular distribution of the reflected light, as discussed in the previous paragraph. However, the method as a whole has inherited some limitations of the base method. First, the estimated chromophore concentrations depend on the optical parameters and geometries used in the MCS. The thicknesses and scattering coefficients of the epidermis and dermis layer can vary with the individual, the site, and the condition of the skin (e.g., water content). Second, an adequate amount of light should be reflected from the dermis for a precise evaluation of the chromophore concentrations. In the case of darker skin, light is strongly absorbed in the epidermis, and the intensity of the light that reaches the dermis is weak. As a consequence, the error in the estimation of the chromophore concentration, especially of oxygenated and deoxygenated hemoglobin, will be larger than that for lighter skin.

In the case of oily skin, the specular reflection is stronger than that of non-oily skin, but this was corrected by using a polarizer in our measuring system. However, the amount of sebum will affect the scattering power of the epidermis, and thus it will also affect the estimated chromophore concentration. The existence of sebum is expected to decrease the scattering power of the surface of the epidermis and thus increase the penetration depth. This may result in an overestimation of the chromophores.

This method is very useful for the diagnoses of skin spots or lesions, especially when they are so large that the surface curvature becomes non-negligible; an example of this is a port-wine stain [97]. Also, in aesthetic evaluations in dermatology and cosmetology, evaluations of each body part (especially the face) as a whole are important [98]. The robustness of this method against fluctuations in the intensity of the light source provide a practical advantage. In practical applications, the intensity of the light source is sometime not stable; for example, when using a flashbulb. However, to the extent that the spectrum of the light source is proportional, the derived chromophore concentrations will not be affected, since the effect is gathered into a_0 in MRA1. This method is not limited to imaging: it can also be used for point measurements when the stability of the light source intensity cannot be guaranteed. On the other hand, the method cannot be applied when wavelength-dependent information cannot be utilized, such as for the derivation of the absorption and reduced scattering coefficient μ_a and μ_s' [44, 99]. In this case, the effect of shading will also cause errors in the estimated concentrations of chromophores.

3.5. Conclusion

In this paper, we presented a method for quantitative evaluation of skin chromophores over wide regions. We achieved the reduction of shading-derived artifact by eliminating the constant term of the B-L method in the conversion of the regression coefficients to concentrations. This method is robust to errors in estimating the irradiance and also accounts for the scattering effect. Measurements of a forearm confirmed that, by optimizing the compensation formulae, the proposed approach can dramatically reduce the shading-derived artifacts and fully account for the scattering effect. The proposed

approach will enable more accurate imaging of large areas, such as whole arms, hands, faces, or legs. Although the method has problems with noise and artifacts, these can be overcome by applying the modified B-L method to MRA1. This issue should be further investigated.

4. Critical angle method to refractive index measurement of human skin *in vivo*

4.1. Introduction

The refractive index (RI) of skin is an important parameter that indicates the condition of skin. It also defines the characteristics of light reflection from skin. It has thus been recognized as an important parameter in applications such as laser therapy [57] and cosmetics [58]. Various methods have been developed for measuring it. Methods for measuring skin RI can be broadly categorized into two kinds based on their measurement area and depth. One class of methods measure the average RI between two interfaces (e.g., the upper and lower surfaces of the epidermis); they utilize the difference between the physical and optical distances between the interfaces [45-47]. The other class of measurements measure the RI of an area close to a surface and utilize the relationship between the incident angle and the reflectance [48-54]. In the case of *in vivo* measurements of skin, the measurement depth is important because the amount of water varies dramatically with depth and it generates a gradient in the RI with depth [55, 56]. In evaluating the behavior of light at air–skin interface, the latter class of measurements is more appropriate since those measurements are considered to sensitive to the ratio of surface reflection to interior reflection [57-59].

The ultimate goal of our research is to measure *in vivo* the RI of a superficial area of a cornified layer. However, since this is difficult, most studies have performed *ex vivo* measurements of slices of skin [52-54]. The main source of difficulty of *in vivo* measurements is undulations in the skin surface [60]. RI measurements generally require precisely measuring the reflectance as a function of the incident angle at the interface between a prism and a sample. Consequently, a flat sample surface is needed to ensure good contact between the prism and the sample. Hence, some modification is required to apply this method to samples with rough surfaces. In some studies, the sample was pressed against the prism by applying a high pressure to achieve good contact [53, 54]. However, this method is not suitable for *in vivo* measurements. Another significant problem of *in vivo* measurements is their long acquisition times. This is inconvenient for the subject. Furthermore, the skin conditions will change over time since the water content will vary due to occlusions. Due to these difficulties, almost all previous studies performed *ex vivo* measurements of skin slices. This results in other problems. First, this method is destructive. In addition, after being cut off, skin will dry out since its water supply is disrupted; this will change its RI [57, 61]. To make the conditions of samples close to those living skin or to increase the contact area, other studies have used saline [52-54] or high-RI immersion oil [61]. However, various kinds and amounts of liquid are applied and these factors will affect the RI. Therefore, *in vivo* measurements are desirable for evaluating the RI under different conditions and for different individuals.

In this report, we modify the critical angle method for partial contact to realize *in vivo* measurements of the RI of skin. We then evaluate the feasibility of this method by performing *in vivo* measurements of silicone samples and human skin. We also discuss

the effect of absorption, which is disregarded in the proposed method.

4.2. Materials and Methods

4.2.1. Critical angle method for partial contact

The critical angle method is commonly used to accurately measure the RIs of liquids, but it assumes that no absorption occurs and there is total contact between the probe and sample [49, 100]. Assuming that light is incident on the interface from a medium with an RI of n_i to a medium with an RI of n_t, the reflectance will be 1 for incident angles larger than or equal to the critical angle:

$$\theta_c = \sin^{-1}\left(n_t / n_i\right), \tag{4-1}$$

when $n_i > n_t$ [48, 50-52]. On the other hand, the reflectance will decrease rapidly as the incident angle decreases from the critical angle. This allows the critical angle to be easily and precisely determined, especially for p-waves. In the critical angle method, the RI of a sample n_t is determined from Eq. 4-1 using a prism with a known RI of n_i and measuring θ_c. This method is not usually used for solid materials with rough surfaces since partial contact makes θ_c indistinct.

Here, we assume that the reflection for a prism can be expressed as a simple sum of reflection from areas that are in contact and reflection from areas that are not in contact. In this case, the variation of the reflectance near the critical angle will be indistinct due to mixing of light reflected from areas in contact and from areas that are not in contact. However, the critical angle still exists. Since the RI of air ($n \approx 1$) is much smaller than that of skin ($n > 1.33$) [57], the reflectance from a non-contact area will be 1 when the incident angle is near the critical angle of skin. Based on the above assumption, the

reflectance R can be expressed as a function of the incident angle as

$$R(\theta_i) = A \cdot r(\theta_i) + (1 - A). \tag{4-2}$$

Here, θ_i is the incident angle, $r(\theta_i)$ is the reflectance of an area where there is contact, and A is the ratio of the contact area to the total area. The first and second terms in Eq. 4-2 correspond to areas in contact and areas out of contact, respectively. The Fresnel equation can be substituted for $r(\theta_i)$. According to Eq. 4-2, even when there is partial contact between the prism and the sample, the critical angle can still be determined provided A is sufficiently high. Since human skin is flexible, this condition is realizable.

4.2.2. Measurements and data analysis

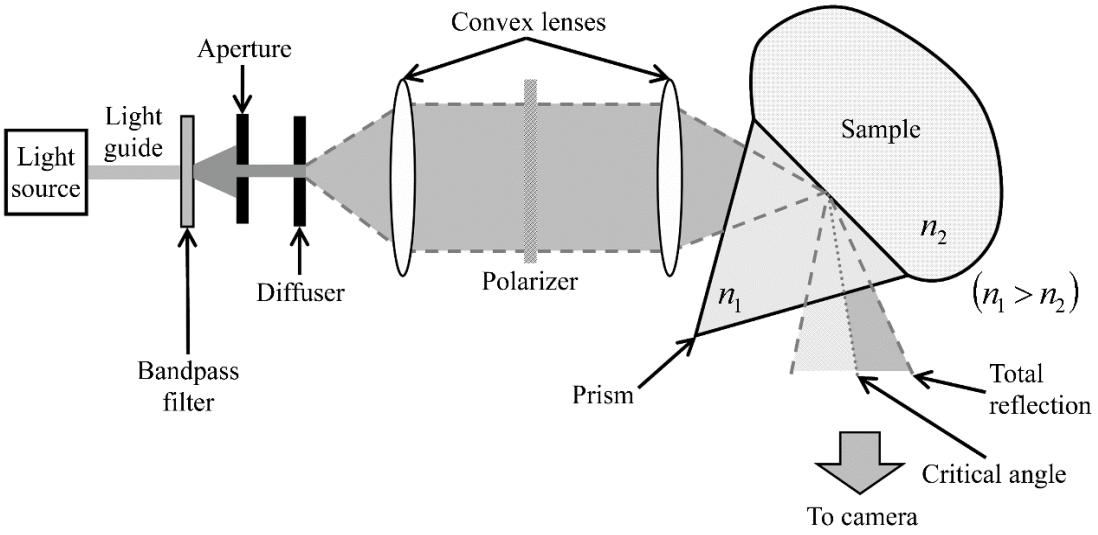

Fig. 4-1 Schematic of measurement system.

The instrument shown in Fig. 4-1 was used for RI measurements. Light from the light source (LA-180Me, Hayashi Watch-Works, Tokyo, Japan) passes through a bandpass filter (43178-H, Edmund Optics, Barrington, NJ, USA; center wavelength: 550 nm; full width at half maximum: 10 nm) and an aperture. It is then spread out by a diffuser. The light is then collimated by two convex lenses before it strikes the equilateral-

triangular prism (SFL11, Edmund Optics; RI at 550 nm: 1.791). It illuminates a sample after passing through the prism. The light spot on the sample was about 5 mm in diameter. A polarizer was inserted between two convex lenses to generate a p-wave. The reflected light was recorded by a camera (D200, Nikon, Tokyo, Japan) with an attached lens (Ai Nikkor, Nikon; 50 mm f/1.2S). The focal point of the lens was set at infinity so that each position of the acquired image can be associated with each incident angle. The exposure time was set to 1/5 s and the aperture was set to *f*/1.2. The prism and the camera could be independently rotated about the center of the prism to allow for variations in RI; their positions were varied according to the sample used (i.e., silicone or skin).

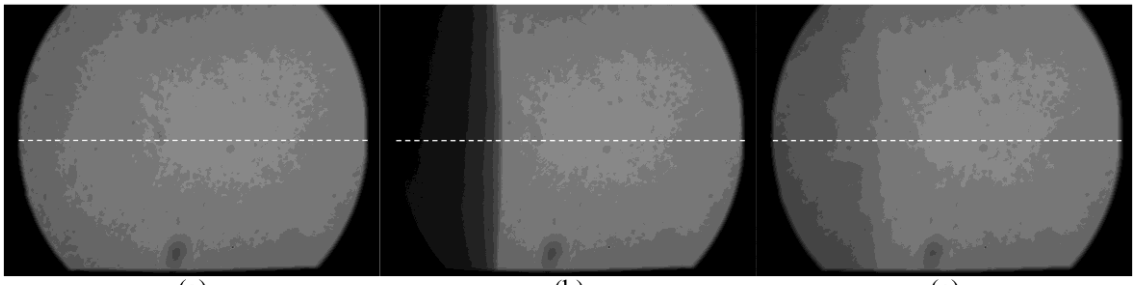

(a) (b) (c)

Fig. 4-2 Representative examples of linear images (i.e., intensity is linear) of green channel for Experiment 1. Each point on the broken lines in the images is correlated with each incident angle. (a) No sample; (b) sample with flat surface; (c) sample with rough surface. The reflectance of each incident angle was obtained along the broken lines.

From the images taken with the system shown in Fig. 4-1, the correlation between the reflectance and the incident angle was obtained. Below, the protocol is explained using data from experiment 1. First, images without a sample (when the prism is contact

with air) and images with a sample were obtained. They were saved as raw data (12 bits/pixel/channel) and then converted to TIFF images (16 bits/pixel/channel) whose pixel values vary linearly with the light intensity (Fig. 4-2). The angular distance between adjacent pixels was approximately 0.004°. The pixel values along the horizontal center line (see Fig. 4-2) were extracted. Next, the reflectance was derived by dividing the pixel values by the corresponding pixel values in the image obtained without a sample (i.e., pixel values when the reflectance is unity). The repeatability error of the pixel value was evaluated from duplicate measurements of air (the condition shown in Fig. 4-2a) and the standard deviation of the reflectance was found to be 0.15 %.

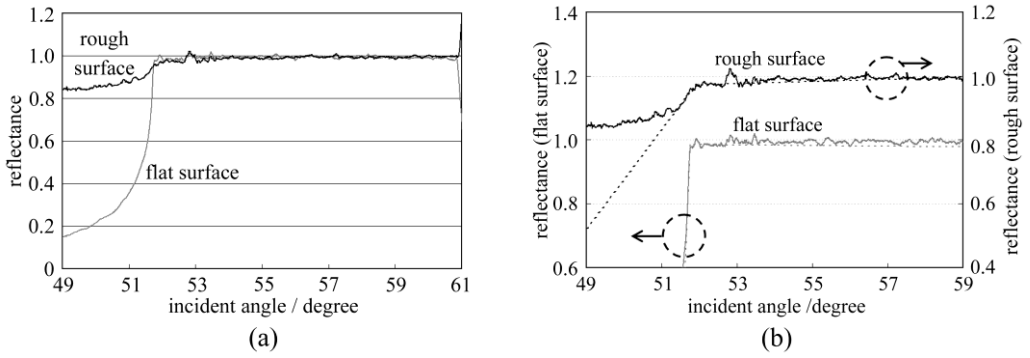

Fig. 4-3 Reflectance as a function of incident angle for flat and rough surfaces: (a) reflectance and (b) fitting results. Gray line: flat surface; black line: rough surface. The broken line indicates the fitting results. For clarity, the area near the critical angle was enlarged and the *y* axis of each sample was shifted in (b). The profiles are averages of multiple measurements of each sample.

Using the relationship between the incident angle and the pixel position, a plot of reflectance against incident angle was obtained (Fig. 4-3a). The relationship between the incident angle and the position in the image was determined from data obtained in advance by performing measurements using an RI matching liquid (Cargille Laboratories,

Cedar Grove, NJ, USA). From the position of the critical angle of liquids, the incident angle was correlated with the horizontal axis in the images by making a linear approximation.

A profile of reflectance against incident angle was approximated by two lines (Fig. 4-3b) with tangents of p_1 and p_2 that are connected at the point (X_C, Y_C):

$$\begin{cases} if\ x < X_C : y = p_1 \cdot (x - X_C) + Y_C \\ \quad else : y = p_2 \cdot (x - X_C) + Y_C. \end{cases} \tag{4-3}$$

X_C was taken to be the critical angle. The four parameters X_C, Y_C, p_1, and p_2 were calculated from the profile as an optimization problem. Specifically, the 'fminsearch' function in MATLAB software (Mathworks, Natick, MA, USA) that implements the Nelder–Mead simplex method was used. The area to be fixed was defined visually. Although Eq. 4-2 in which the Fresnel equation is substituted for $r(\theta_i)$ is theoretically rigorous, the optimization problem did not converge well. This is probably due to several errors and the degrees of freedom of A, which makes the prediction ambiguous. In the approximation, the estimation of X_C will not be affected by A, which can be confirmed by substituting Eq. 4-3 for $r(\theta_i)$ in Eq. 4-2. Furthermore, X_C will not be affected by fluctuations in the light source intensity provided the fluctuation percentage is constant.

4.2.3. Silicone samples

Silicone samples with flat and rough surfaces were prepared using a transparent, room-temperature-curing silicone resin (KE-108 (condensed), Shin-Etsu Silicones, Tokyo, Japan) as a base. A catalyst (CAT-108, Shin-Etsu Silicones) was added to KE-108 and the mixture was poured into a mold. Rough surfaces were formed by taking the

topography of the surface of the forearm of a male (38 years old) using polyether impression material (Impregum soft, Sumitomo 3M, Tokyo) and using it as a part of the mold, to imitate the topography of actual skin. The RI obtained by the dipping method was n_D = 1.41±0.01 (details not given).

4.2.4. Conductance (water content) measurements

The conductance, which is expected to reflect the water content [101, 102], was measured using a Skicon 200 EX instrument (IBS, Shizuoka, Japan) along with RI. In addition to the conductance method, capacitance measurements are considered to be a straightforward method for evaluating moisture content [101, 102]. However, conductance measurements are more suitable than capacitance measurements in the present case since the conductance depends more on the water content of shallower regions than the capacitance [102, 103].

4.2.5. Experiment 1: silicone samples

The RIs of silicone sample with flat and rough surfaces were measured to verify the assumption in Subsection 4.2.1. Each area was measured several times and the average was taken.

4.2.6. Experiment 2: *in vivo* measurements of human skin (cheek)

The left and right cheeks of Japanese adult females (n = 16) in their 20s to 40s were measured. After removing makeup and washing their faces, each subject remained in a controlled room (temperature: 20°C; relative humidity: 40%) for over 20 min. The conductance and RI of the left and right cheeks were then measured. Each site was

measured five times and the average was taken.

4.3. Results

4.3.1. Experiment 1: silicone samples

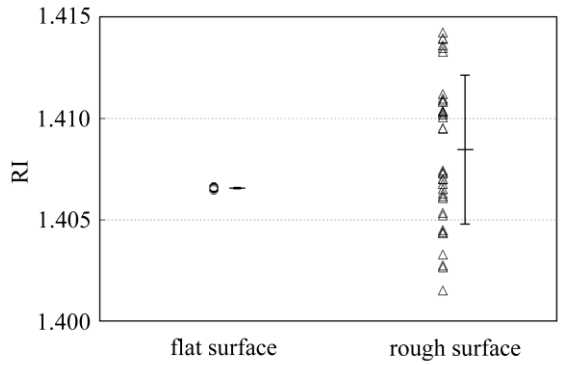

Fig. 4-4 RIs obtained in different measurements. Open circles (for flat surface) and open triangles (for rough surface) are values obtained in different measurements. The bars to the right of the data points represent the average and the standard deviation.

From the acquired images (Fig. 4-2), the intensity of the reflected light was derived as a function of the incident angle. It was then converted to reflectance (Fig. 4-3a) and fitted using Eq. 4-3 (Fig. 4-3b). The profile shown in Fig. 4-3 represents the average of multiple measurements. The numbers of measurements performed for flat and rough surfaces are 10 and 37, respectively. The RIs of the flat and rough surfaces were calculated to be 1.407 (SD = 4.9×10^{-5}) and 1.408 (SD = 3.6×10^{-3}), respectively (Fig. 4-4). These average values are very similar, while the standard deviation of the rough surface is larger than that of the flat surface.

4.3.2. Experiment 2: *in vivo* measurements of human skin (cheek)

Fig. 4-5 shows a representative example of the profile of human skin (cheek) and the result of fitting. This representative profile was compared with Eq. 4-2 obtained using the Fresnel equation with complex RIs ($N = n + ik$) and varying k (Fig. 4-6a). Here, n was set to the estimated RI and A was visually selected to make the range of the theoretical profile fit the range of the measured profile. The value of k that gave the closest profile to the measured profile was 0.004 in terms of the sharpness of the shoulder. A representative profile was compared with Eq. 4-2 with $k = 0.004$ varying n (Fig. 4-6b). The value of n for the closest profile to the measured profile was 1.513 near the shoulder.

Fig. 4-5 Representative example of skin reflectance as a function of incident angle and fitting results. The RI of this measurement was $n = 1.521$. The fitting range for this profile was set to 56.8–59.7° (indicated by the two vertical broken lines).

RI was plotted against the conductance at each site (i.e., two points on the left and right cheeks of each panelist) (Fig. 4-7). There is a significant correlation between the conductance and RI at a 99.9% confidence level.

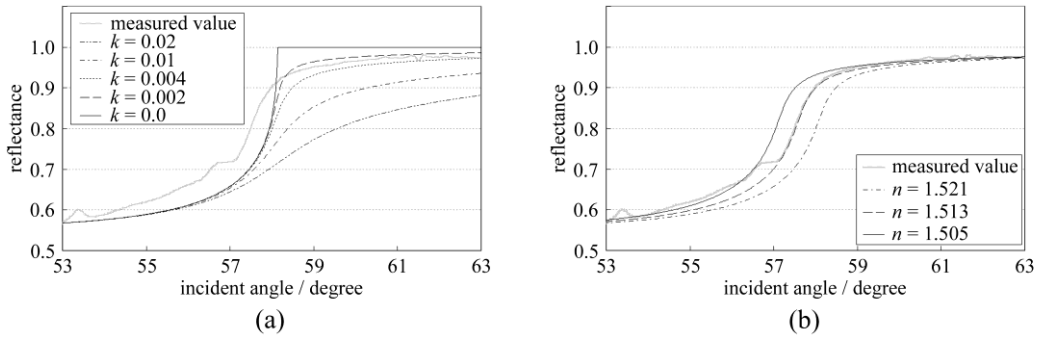

Fig. 4-6 Theoretical profiles of reflectance as a function of incident angle from Eq. 4-2 with the Fresnel equation varying complex RI ($N = n + ik$) with the measured profile (as in Fig. 4-5, RI = 1.521). A = 0.45. (a) With constant n of 1.521, k was set to 0, 0.002, 0.005, 0.01, and 0.02. (b) With constant k of 0.004, n was set to 1.521, 1.513, and 1.505 (interval of 0.008).

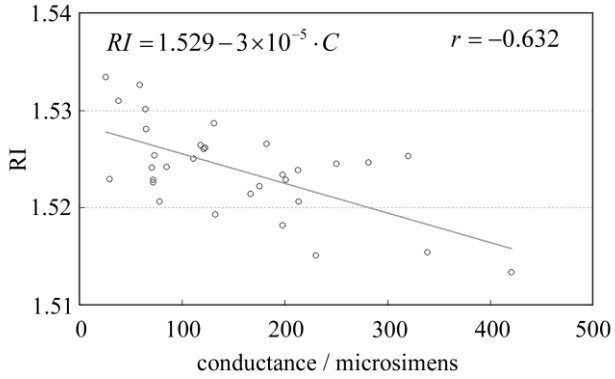

Fig. 4-7 Correlation between RI and conductance C. The unit of conductance is microsiemens.

4.4. Discussion

The critical angle of the rough surface is indistinct due to partial contact (Fig. 4-2c), but it was still recognizable (Fig. 4-3). From the profiles, RIs were derived for partial contact with the rough surfaces, although the standard deviation was greater than that for

the flat surface, which had better contact (Fig. 4-4). This result indicates that the critical angle method can be used for rough silicone surfaces provided that a sufficiently high proportion of the area is in contact and that the material has a low absorption.

As shown in Fig. 4-5, in the *in vivo* measurements of cheek skin, the RIs were measured in the same manner as for the silicone samples. In other words, a sufficiently high contact area for the RI measurement was achieved by getting the subjects to press the measurement site against the prism. A short acquisition time was realized, which reduces problems associated with time-varying conditions such as skin surface deformation and water content variation due to occlusions. From Fig. 4-7, the RI range was about 1.51–1.53, which is relatively higher than those of previous studies (which are less than 1.5) [52-54, 61]. This is probably due to the skin surfaces being relatively dry in our experiment. Although the present experiments were performed using a p-wave, a previous study indicated that the anisotropy is small [53].

Assuming the discrepancy between the theoretical and measured profiles is only due to absorption, we estimated the effect of absorption by extending RI to complex RI. The imaginary part k of complex RI is visually estimated to be about 0.004 from the sharpness of the shoulder in the profiles shown in Fig. 4-6a. Although the sharpness of the shoulder can be changed by varying A in Eq. 4-2, this will also alter the reflectance range so that the profile will not be close to the measured profiles. For the measured site in Fig. 4-6b, the RI value is possibly overestimated by about 0.008. Although earlier studies found that the epidermis has a higher absorption (k = 0.02) [53, 54], the actual value may be smaller than that determined from plots of the actual reflectance against the incident angle, which are sharper than the fitting results shown in the studies [53, 54].

Since other causes may smooth the profile of the reflectance against the incident angle, our estimate may represent an upper limit for k.

The RI is significantly correlated with the conductance, which depends on the water content [101, 102] (Fig. 4-7). The water content is expected to greatly affect the RI because the RI of water (1.33) differs significantly from that of dry tissue (≈1.5) [57]. The water content is known to vary between sites and individuals [104]. Although the sebum is also a variable factor, it is not expected to greatly affect the RI measurements because the sebum at the measurement sites is expected to be washed away by washing the skin. To the best of our knowledge, this is the first time that a correlation between these two parameters has been observed above the natural variation, although the relationship has been theoretically predicted in previous studies [57, 61]. From this result, we estimate the RI from conductance C (μS) using the formula $RI = 1.529 - 3\times10^{-5}\cdot C$, without considering systematic errors. Alternatively, we can use $RI = 1.521 - 3\times10^{-5}\cdot C$ by assuming that the offset of 0.008 from the results of the above discussion can be applied to all subjects. This formula for the conductance varies between measurement devices; the above formula is unique to Skicon 200 EX.

Despite being a straightforward and well-studied method for estimating the water content in skin [101, 102], the conductance method has problems. The most serious problem is the contact resistance between the skin and the probe, which affects the conductance. An increase in the contact area will reduce the contact resistance and hence increase the measured value. In future studies, the relationship between RI and the water content should be determined by direct methods that are insensitive to the contact ratio such as confocal Raman microspectroscopy [55, 104]. Other factors such as temperature and dielectric substances are considered to be suppressed since the room

temperature was controlled and the measurement sites were cleaned prior to the measurements.

This method can be applied to other wavelengths by using bandpass filters for different wavelengths. However, we used a single wavelength in the present study for the stable measurement because replacing the filter prolongs the measurement time and makes it difficult to perform quick measurements. This problem can be overcome by improving the system design.

The derivation of θ_c from these profiles has the potential to be improved in future studies. Theoretically, the profile should be fitted by the Fresnel equation with complex RI [48, 49, 52-54]. RIs have been measured in this manner in recent studies [52-54]. We also tried this method, but found that it did not work well, which is probably due to errors from other sources. An alternative method has been proposed that involves detecting the maximum of the first derivative [105]. Although detection is difficult, this method is worth considering since it seems to be more robust against absorption than our method [105].

There are some other probable causes of errors in the present measurement method. First, there may be multiple reflections in the prism and in the skin, which would reduce the angular resolution. In most previous studies, the effect of stray light from other incident angles was nullified by performing successive measurements at different incident angles [50, 51, 53, 54]. Simultaneous measurements in the present method are essential for realizing a short measurement time, but they adversely affect the angular resolution. A second potential source of errors is intermediate regions between contact and non-contact areas. Although we assumed a binary condition in Eq. 4-2, the gap between the prism and the sample changes varies continuously between contact and non-contact. In

intermediate regions, the light behavior will differ from that of either contact or non-contact areas due to the effect of evanescent waves [106]. In addition to these errors, the RI may vary on the surface due to the fact that the stratum corneum is composed of materials with different RIs, including sebum, water, and cell membrane. As Fig. 4-5 shows, the profiles of some subjects exhibit a plateau (about 57° in Fig. 4-5), which implies such a composition.

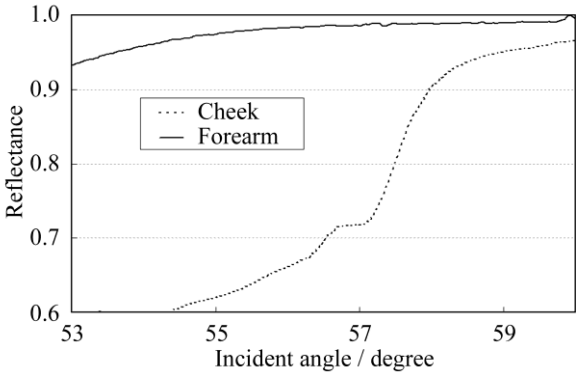

Fig. 4-8 Representative profiles of reflectance against incident angle of forehand and cheek.

This method assumes that deformation of the skin will provide a sufficiently high contact area to enable the critical angle to be determined. However, skin deformability and topography varies between sites, individuals, and conditions (e.g., water content). Consequently, the method will not always give valid results. As a preliminary study, we show a representative profile of the inner side of a forearm together that of a cheek (Fig. 4-8). The folding point of the forearm gives more ambiguous results than the cheek; this is probably due to the smaller contact area and the stronger absorption. In fact, the estimation for the forearm profile performed in the same manner as the cheek profile indicated $A \approx 0.09$ and $k \approx 0.02$, which is smaller and larger than the values for cheek,

respectively. The cheek is more measurable than the forearm due to its greater deformability and lower absorption, making detection of the folding point easier.

We found that the critical angle method is applicable to cheek skin provided there is a high contact ratio and low absorption. In addition, we explained the variation in the RIs of individuals in terms of water content using the critical angle method, which suggests that the method is sufficiently accurate for detecting the variation under normal conditions (at least relatively). Although measurable sites are currently limited to the cheek, it is anticipated that the application range of this method can be extended by improving the method.

5. Measuring translucency using edge-loss

5.1. Introduction

Translucency is an important factor in giving skin a natural appearance, and can also provide clues as to the internal condition of the skin. Given the importance of translucency, numerous studies have been performed on this parameter in the fields of medicine [18, 21, 62, 63], cosmetics [64, 65], and computer graphics [66, 67]. In the field of cosmetics, one of the important goals is the improvement of skin appearance in daily life. In the field of medicine, the same can be said for cases where esthetic problems are a major concern. In such cases, the interest is in small variations in factors encountered during daily life (such as changes due to external stimuli like ultraviolet radiation, skin-care activities, or aging) as influences on appearance. The important issue is measuring translucency as an eventual lateral spread of reflected light and relating such measurements to appearance.

Most previous studies, however, have mainly discussed the standard optical properties of average human skin, with few studies attempting to assess individual differences or variations during daily life. Generally, translucency can be evaluated by calculating the absorption coefficient and effective scattering coefficient [21, 67, 68] or

the effective attenuation coefficient [66, 68] from a measured point spread function (PSF). One frequently used measurement configuration is the linear fiber array method, which involves a single optical fiber for light incidence and multiple optical fibers for light measurement lined up in a single row with the edges adjacent [66, 69]. Another proposed configuration is video reflectometry measurement (VRM), which involves focusing light on the measurement surface through a system of lenses and using a camera to acquire images of the returning light [21, 62, 64, 67, 70]. Such conventional methods for translucency measurement need to detect weak signals from points adjacent to the incident point, thus requiring detection over a wide dynamic range and strict shielding from stray light from the environment and the incident point. In addition, given skin unevenness, point sources of light can be affected by the location of incidence. The instruments and protocols for measurement therefore tend to be elaborate to respond to these challenges.

Given this background, we tried to develop another method for easy detection of daily changes in translucency as the lateral spread of reflected light utilizing edge-loss. Edge-loss is a phenomenon known to cause changes in measurement values depending on the type of colorimeter [107-109]. Many studies have been conducted in the field of prosthetics, where the effect is particularly apparent and can easily result in esthetic issues [107, 109-113]. Edge-loss is also known to exert an influence when colorimetry is performed on human skin [108]. Studies of edge-loss have shown that the choices of illumination area and measurement area exert major influences on the magnitude of colorimetry results [107-109, 111, 112, 114]. Although some of these studies have suggested the idea of quantifying sample translucency using edge-loss [112, 114], the choice of measurement conditions has not been adequately generalized.

We therefore began with a generalization of the relationship between illumination area, measurement area, and edge-loss, and optimized the measurement conditions (the combination of illumination area and measurement area). We then evaluated the adequacy of our optimization with translucent samples, and examined how translucency index varies with changes in the absorbing and scattering power of human skin.

5.2. Materials and Methods

5.2.1. Measuring Device

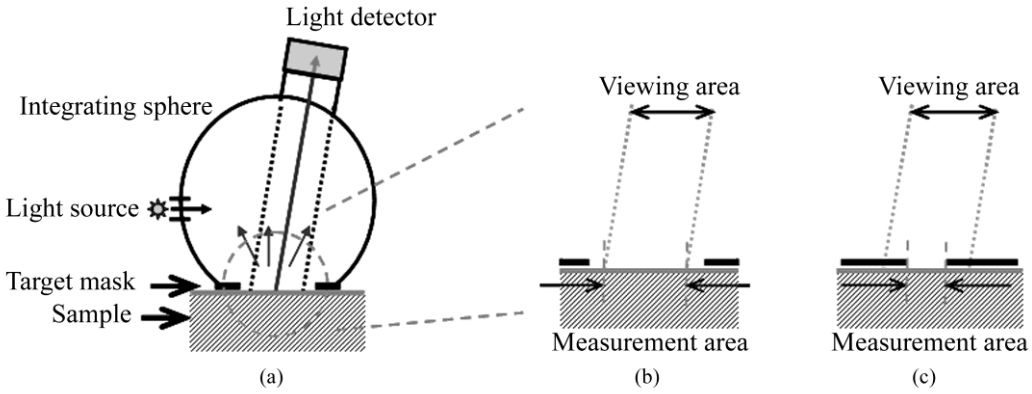

Fig. 5-1(a) Schematic of the measurement device. Light from the light source is diffused by the integrating sphere and illuminates the sample. Part of the reflected light enters the detector and its spectrum is measured. (b) Measurement area when aperture radius exceeds detector viewing radius. The measurement radius is equal to the viewing radius. (c) Measurement area when detector viewing radius exceeds aperture radius. The measurement radius is equal to the aperture radius.

In our method, translucency is calculated from reflectances measured using a CM-2600d portable spectral reflectometer (Konica Minolta, Tokyo, Japan). This device has an

optical system with diffusion light illumination/8º detection (Fig. 5-1a). Reflectance can be measured in 10-nm increments across a 360- to 740-nm spectrum. SCE (excluding specular reflection) mode was used in this study.

The CM-2600d reflectometer can alternate the detection radius between 4 mm and 1.5 mm, and the target mask that comes into contact with the sample can be changed. We utilized these features of the device in the present study. For normal measurements, a target mask with a 5.5-mm aperture radius is used when the detection radius is set to 4 mm (MAV mode), and a target mask with a 3-mm aperture radius is used when the detection radius is set to 1.5 mm (SAV mode). However, using a target mask with a different aperture radius allowed the creation of measurement conditions different from those normally used.

Let us consider how varying the aperture radius of the target mask changes the measurement radii when the detector viewing radius of the device is constant. If the viewing radius is smaller than the aperture radius, the entire viewing area is the sample surface, and the measurement radius is equal to the viewing radius (Fig. 5-1b). Conversely, if the viewing radius is larger than the aperture radius, only the area of the sample within the aperture is exposed within the viewing area, and the measurement radius is equal to the aperture radius (Fig. 5-1c).

5.2.2. Formulation of Edge-Loss

To optimize the measurement conditions, we modeled reflectance measurement in order to evaluate edge-loss for given measurement conditions and a given PSF. Wavelength is not explicitly stated, but each parameter is in fact a function of wavelength. Using the BSSRDF $S(\vec{x}_i, \vec{\omega}_i; \vec{x}_o, \vec{\omega}_o)$, incident radiance $L_i(\vec{x}_i, \vec{\omega}_i)$ from direction $\vec{\omega}_i$ to point

$\vec{x}_i$ and outgoing radiance $L_o(\vec{x}_o, \vec{\omega}_o)$ from point $\vec{x}_o$ in direction $\vec{\omega}_o$ can be expressed according to the following relationship [66, 67]:

$$L_o(\vec{x}_o, \vec{\omega}_o) = \int_A \int_{2\pi} S(\vec{x}_i, \vec{\omega}_i; \vec{x}_o, \vec{\omega}_o) \cdot L_i(\vec{x}_i, \vec{\omega}_i) \cdot (\vec{n} \cdot \vec{\omega}_i) d\vec{\omega}_i d\vec{x}_i \quad (5\text{-}1)$$

Here, $\vec{n}$ is the normal vector to the sample surface, and the integrated areas A_i and 2π are the illumination area and the solid angle of the hemisphere, respectively. Next, reflectance of the sample is expressed in terms of the outgoing radiance. Apparent reflectance can be written as r according to the following formula:

$$r = \frac{\int_A L_{os}(\vec{x}_o, \vec{\omega}_d) d\vec{x}_o}{\int_A L_{ow}(\vec{x}_o, \vec{\omega}_d) d\vec{x}_o} \quad (5\text{-}2)$$

$L_{os}(\vec{x}_o, \vec{\omega}_d)$ and $L_{ow}(\vec{x}_o, \vec{\omega}_d)$ are the outgoing radiance in the direction of the detector of the sample and a standard white plate, respectively. Vector $\vec{\omega}_d$ is the direction of the center of the detector as seen from the center of the measurement area, and the domain of integration A_o indicates the measurement area on the sample. Next, the BSSRDF of the sample $S_s(\vec{x}_i, \vec{\omega}_i; \vec{x}_o, \vec{\omega}_o)$ and the BSSRDF of the standard white plate $S_w(\vec{x}_i, \vec{\omega}_i; \vec{x}_o, \vec{\omega}_o)$ are related by the following formula:

$$\begin{aligned} &\int_{2\pi} S_s(\vec{x}_i, \vec{\omega}_i; \vec{x}_o, \vec{\omega}_d) \cdot L_i(\vec{\omega}_i) \cdot (\vec{n} \cdot \vec{\omega}_i) d\vec{\omega}_i \\ &= R \cdot p(\vec{x}_i, \vec{x}_o) \cdot \int_{2\pi} S_w(\vec{\omega}_i; \vec{\omega}_d) \cdot L_i(\vec{\omega}_i) \cdot (\vec{n} \cdot \vec{\omega}_i) d\vec{\omega}_i \end{aligned} \quad (5\text{-}3)$$

However, $\int_{\vec{x}_o} p(\vec{x}_i, \vec{x}_o) d\vec{x}_o = 1$ and $S_w(\vec{\omega}_i; \vec{\omega}_o) = \int_A S_w(\vec{x}_i, \vec{\omega}_i; \vec{x}_o, \vec{\omega}_o) d\vec{x}_o$, where A is the

whole surface. Here, we call R the true reflectance and $p(\vec{x}_i, \vec{x}_o)$ the normalized PSF. $R \cdot p(\vec{x}_i, \vec{x}_o)$ is the PSF weighted by incident radiance.

With further assumptions of isotropy and homogeneity regarding BSSRDF and incident radiance, Eqs. 5-1, 5-2, and 5-3, apparent reflectance r can be calculated as follows:

$$r = \frac{R}{S} \cdot \int_{A_o} \int_{A_i} p\left(\left|\vec{x}_o - \vec{x}_i\right|\right) d\vec{x}_i d\vec{x}_o \quad . \tag{5-4}$$

Here, S is the area of the sector $A_i \cap A_o$, and $p(\vec{x}_i, \vec{x}_o)$ is replaced by $p\left(\left|\vec{x}_o - \vec{x}_i\right|\right)$.

Finally, edge-loss is evaluated. When both the illumination radius and measurement radius are finite, apparent reflectance is less than true reflectance due to edge-loss. We defined edge-loss E quantitatively as this percentage decrease, as:

$$E = (R - r)/R = 1 - \frac{1}{S} \cdot \int_{A_o} \int_{A_i} p\left(\left|\vec{x}_o - \vec{x}_i\right|\right) d\vec{x}_i d\vec{x}_o \tag{5-5}$$

5.2.3. Optimization of measurement conditions

From Eq. 5-5, we evaluated the relationship between illumination radius, measurement radius and edge-loss with numerical integration. Here we used a simple function system, Eq. 5-6, as the function system for the PSF for the purpose of approximation, since our objective was simply to evaluate the effect of the relative degree of lateral spread.

$$p\left(\left|\vec{x}_o - \vec{x}_i\right|\right) = \frac{\mu_{eff}}{2\pi} \cdot \frac{\exp\left(-\mu_{eff} \cdot \left|\vec{x}_o - \vec{x}_i\right|\right)}{\left|\vec{x}_o - \vec{x}_i\right|} \quad . \tag{5-6}$$

Preliminary experiments showed that, using the red channel of the camera, the normalized PSF of human skin obtained by VRM [64, 67] fit well with Eq. 5-6 if μ_{eff} was used as a fitting parameter. The mean value of μ_{eff} for Japanese forearm skin was around 0.8 mm^{-1} (results of preliminary experiments, details not shown).

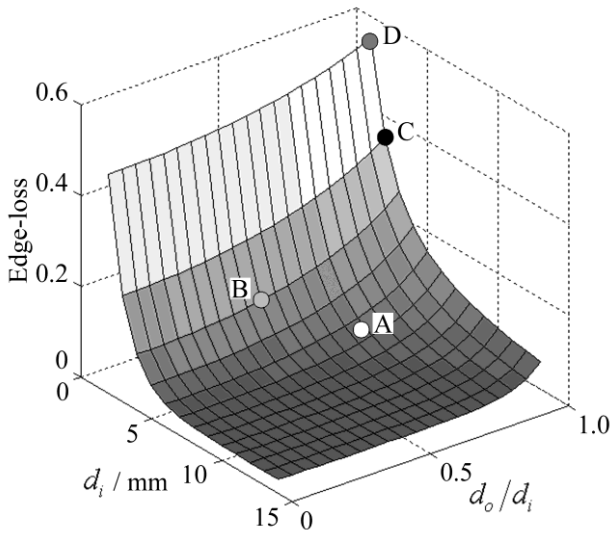

Fig. 5-2 Magnitude of edge-loss for illumination radius (d_i) and measurement radius/illumination radius (d_o/d_i) given in Eq. 5-6 (μ_{eff} =0.8 mm^{-1}) for normalized PSF. Points A-D in the plot show conditions used for reflectance measurement (see Table 5-1). Edge-loss values at points A-D in the plot were 0.050, 0.118, 0.354, and 0.553, respectively. The combination of A and C was used in Experiment 2.

With numerical integration, changes in edge-loss with the illumination radius d_i and the ratio of the measurement radius to the illumination radius d_o/d_i as parameters are evaluated. A plot of the results is shown in Fig. 5-2. Edge-loss increases with

decreasing d_i and increasing d_o/d_i. These results are consistent with findings from previous studies [107-109, 111, 112].

Table 5-1 Illumination radius (d_i) and measurement radius (d_o) conditions A-D and the respective geometrical settings (mm).

	Measurement conditions			Geometrical settings			
Condition	d_i	d_o	d_o/d_i	Mode	Target mask	Viewing radius	Aperture radius
A	5.5	4	0.73	MAV	MAV (standard)	4	5.5
B	3	1.5	0.5	SAV	SAV (standard)	1.5	3
C	2	2	1	MAV	Customized	4	2
D	1	1	1	MAV	Customized	4	1

Using the variation of edge-loss under different conditions, the level of translucency of the sample can be evaluated. Selecting combinations so as to maximize the difference in edge-loss facilitates detection of even small variations. Taking Fig. 5-2 as a reference, a good combination of conditions would be large d_i and small d_o/d_i together with small d_i and large d_o/d_i in order to maximize signal-to-noise ratio (S/N). Optimum conditions must be selected from among those possible, taking into account the additional restriction imposed by the device of possible viewing radii of 4 mm and 1.5 mm. In addition, radii that are too small will cause the measurement to be affected by the reduced

amount of light reflected from the sample and by irregularities in skin topography and color unevenness.

Conditions A and C from Table 5-1 were ultimately selected as standard conditions to combine for calculating translucency index. Conditions B and D were used in Experiment 1 for the purposes of comparison. The MAV mode was used for Conditions A, C and D, and the SAV mode was used for Condition B. For Conditions A and B, the standard target masks for the MAV and SAV modes were used, respectively. For Conditions C and D, the aperture size of each target mask was customized by affixing a black sheet with a hole to a target mask for the MAV mode. Edge-loss values $E(A)$, $E(B)$, $E(C)$, and $E(D)$ in Fig. 5-2 were 0.050, 0.118, 0.354, and 0.553, respectively.

5.2.4. Calculation of reflectance and translucency index

First, sample reflectance was recalculated from the device output values to exclude the reflected component from the target mask from measurement values. Apparent reflectance r_i under condition i is calculated from the following equation.

$$r_i = \frac{r_{i,s} - r_{i,b}}{r_{i,w} - r_{i,b}} . \tag{5-7}$$

Here, $r_{i,w}$, $r_{i,b}$, and $r_{i,s}$ are the measured reflectance values of the standard white plate (a plastic plate supplied with the spectral reflectometer; reflectance in the ordinary sense is 98.57±0.29% at between 400 nm and 700 nm), blank, and the sample under condition i. Here, “blank” refers to the condition in which no light returns from the aperture. Reflectance calculated in this way represents the proportion of the amount of reflected

light compared to that from the standard white plate. Basically, $r_{i,s}$ in this paper represents the mean value from five measurements.

Using the pair of apparent reflectances of the sample thus obtained under the combination of conditions *i* and *j* to meet $E(i) < E(j)$, the translucency index $T_{i,j}$ is defined by the following equation:

$$T_{i,j} = \frac{r_i - r_j}{r_i}. \tag{5-8}$$

From Eq. 5-5, this equation can be rewritten with edge-loss as follows:

$$T_{i,j} = \frac{E(j) - E(i)}{1 - E(i)}. \tag{5-9}$$

From Eq. 5-9, it follows that when $E(i) \approx 0$, then $T_{i,j} \approx E(j)$. As can be seen from Fig. 5-2, within the possible extent of skin translucency, it is Condition A that almost meets this condition. Hereafter, "translucency index" referred to by itself indicates $T_{A,C}$, and "reflectance" by itself refers to r_A.

5.2.5. Experiments

5.2.5.1. Experiment 1: Preparation and measurement of translucent samples

For the purpose of confirming the optimization, translucency indices of samples with different translucencies under multiple combinations (A/C, A/B, and C/D) were measured. Translucent samples were prepared as follows using transparent, room-temperature curing silicone resin (KE-108, condensed type; Shin-Etsu Silicones, Tokyo, Japan) as a base. A set amount of cosmetic foundation (in-house trial product) with

similar color to average Japanese skin and catalyst (CAT-108; Shin-Etsu Silicones) was added to the KE-108, and the mixture was poured into a mold. Proportions of foundation to silicone resin were varied (0.05, 0.10, 0.15, 0.20, and 0.50 wt%) to adjust translucency. When the PSF of each sample was measured with VRM [64, 67] and the μ_{eff} of the samples with foundation proportions of 0.05, 0.10, 0.15, 0.20, and 0.50 wt% was calculated according to Eq. 5-6, values came to 0.03, 0.24, 0.38, 0.63, and 1.38 mm^{-1} at the red channel, respectively (details not shown). Since μ_{eff} of forearm skin was about 0.8 mm^{-1} according to the results of our preliminary experiments, translucency of forearm skin in Japanese is expected to be between 0.20 wt% and 0.50 wt%.

Values for r_A, r_B, r_C and r_D of the translucent samples were calculated from Eq. 5-7, and $T_{A,C}$, $T_{A,B}$, and $T_{C,D}$ were then calculated from Eq. 5-8. Standard deviation for each translucency index $s_{T_{i,j}}$ was evaluated from standard deviations s_{r_i} for r_i and s_{r_j} for r_j by applying the error propagation equation to Eq. 5-8. S/N was evaluated by dividing the change in translucency index between different translucent samples by the error. As mentioned above, translucency of forearm skin in Japanese individuals is expected to be between 0.20 wt% and 0.50 wt% at the red channel. Therefore, for each combined condition, S/N was regarded as the difference between translucency at 0.50 wt% and translucency at 0.20 wt% divided by the error for translucency at 0.20 wt% at 650 nm wavelength.

5.2.5.2. Experiment 2: Measurement of human skin

Experiment 2-1: A/E treatment

To examine the effect of scattering in the stratum corneum on translucency index, scattering power was varied by means of acetone-ether (A/E) treatment [115], which dissolves lipid in the stratum corneum. The resulting reflectances and translucency indices were calculated. The inner forearms of adult males (n=6) in their 30s and 40s were used. A total of five circular areas (inner diameter, 2 cm) were selected on the left and right inner forearms, and these areas were immersed in an acetone-ether mixture for 30 min. Reflectances and translucency indices before and after treatment were measured.

Experiment 2-2: Ultraviolet (UV)-induced erythema

To consider the effect of accumulated pigment (hemoglobin) in the skin on reflectance and translucency index, the reflectance and translucency index of erythema induced by UV irradiation [116] were measured over time. The inner forearms of adult males (n=5) in their 30s and 40s were used. One square area of sides 2 cm was irradiated for 10 min with UV radiation at a UV-B intensity of approximately 300 $\mu W/cm^2$ and a UV-A intensity of approximately 500 $\mu W/cm^2$. This dose is equivalent to approximately twice the minimal erythema dose in ordinary Japanese (result of preliminary experiments). The reflectance and translucency indices of the area exposed to UV radiation were measured before and 1 day after UV irradiation.

5.3. Results and Discussion

5.3.1. Measurement of translucent samples

Reflectances were calculated from output values under each measurement condition using Eq. 5-7, and Fig. 5-3a shows translucency indices $T_{A,C}$, $T_{A,B}$, and $T_{C,D}$ at a wavelength of 650 nm and the errors calculated from these combinations with Eq. 5-8. Fig. 5-3b shows the spectrum of translucency index $T_{A,C}$ as a representative example. The S/N designated in Sec. 5.2.5 was improved in the order of $T_{A,B}$, $T_{C,D}$, $T_{A,C}$ as 11.01, 15.08, 28.29, respectively.

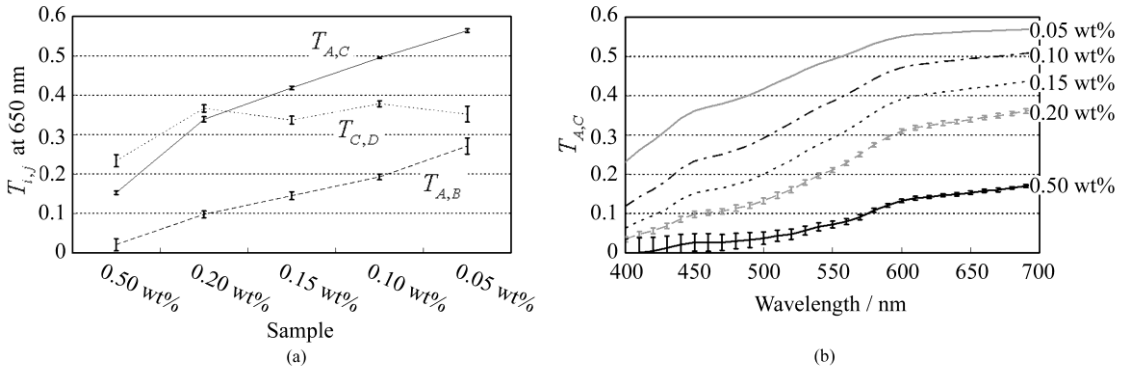

Fig. 5-3(a) Translucency indices of prepared translucent samples (various combinations of measurement conditions for calculating translucency index) at a wavelength of 650 nm. The lower the concentration of foundation (wt%) in the sample, the higher the translucency. (b) $T_{A,C}$ as a representative example. Error bars are shown for 0.5 wt% and 0.2 wt%. In order of increasing translucency, each line represents 0.50, 0.20, 0.15, 0.10, and 0.05 wt%, respectively.

This result supports the hypothesis set out in Sec. 5.2.3 that the S/N would improve

with increasing change in edge-loss. From the given edge-loss values for conditions A-D in Fig. 5-2, changes in edge-loss between combinations A-B, C-D, and A-C can be calculated as 0.068, 0.201, and 0.304, respectively, meaning that the ranking orders of changes in edge-loss and S/N were consistent.

Looking at the comparative values of translucency indices between samples, for $T_{A,C}$ and $T_{A,B}$ the relationship was such that the index increased with increasing translucency across the whole range of sample translucencies. For $T_{C,D}$, however, this ranking order did not hold true between samples with higher translucency of ≤0.20 wt%.

The reason for this was considered to be that a considerable degree of edge-loss occurs in condition i of Eq. 5-9 (condition C in this case). If translucency of the sample increases considerably, $E(j)$ approaches 1 and the variation of $E(j)$ becomes smaller. As a result, $E(j)$ becomes less sensitive than $E(i)$ in terms of translucency. As partially differentiating $T_{i,j}$ with respect to $E(i)$ in Eq. 5-9 always results in negative values, $T_{i,j}$ can be seen to decrease as $E(i)$ increases when $E(j)$ is constant. That is, if $E(i)$ increases significantly, $T_{i,j}$ will not necessarily increase despite increasing sample translucency. Taking these factors into account, it is particularly important to select condition i in Eq. 5-9 so that edge-loss is minimized, in order to expand the coverage of translucency. This result also indicates that the selected combination, which is adequate for the measurement of skin translucency, may be inappropriate for objects with greater translucency.

5.3.2. Measurement of human skin

Experiment 2-1: A/E treatment

Fig. 5-4 shows average values for all subjects for reflectance and translucency index spectra before and after treatment for the areas treated with A/E. Reflectance increased after treatment, but translucency index decreased. Here, values at a wavelength of 650 nm were extracted from the spectrum to specifically investigate the influence of changes in scattering power alone (Fig. 5-5). Reflectance and translucency index had changed significantly with a 99% confidence level.

These changes are reasonable from a qualitative perspective. The increase in the proportion of light reflected by the stratum corneum (where light absorption is weak) is considered to reduce the amount of light that reaches and returns from layers below this (where pigment absorb light), making reflectance increase. At the same time, light returning from shallow locations does not show much diffusion, with light diffusing more widely the deeper it reaches, making the translucency index decrease.

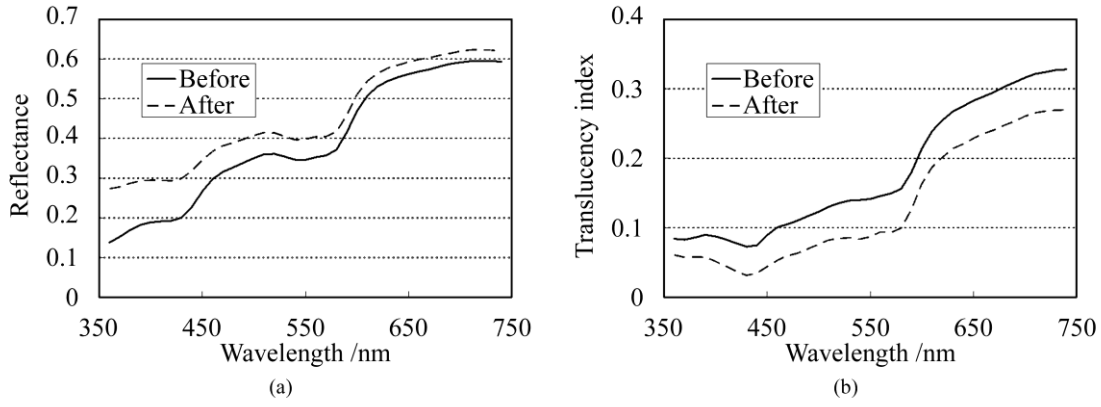

Fig. 5-4 Comparison before and after A/E treatment. (a) r_A; (b) $T_{A,C}$ spectrum. Solid lines: before treatment; dashed lines: after treatment. Values represent mean values for all subjects. r_A increased and $T_{A,C}$ decreased as a result of A/E treatment.

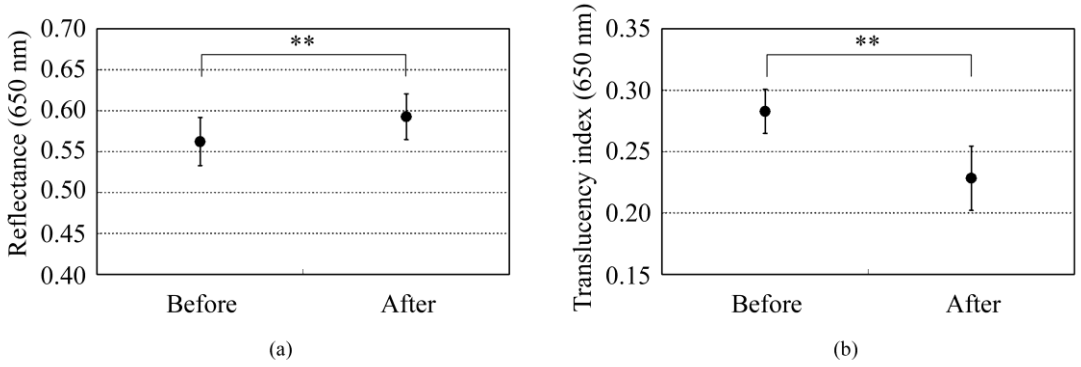

Fig. 5-5 Values at a wavelength of 650 nm extracted from spectra before and after A/E treatment. (a) r_A; (b) $T_{A,C}$. Significance was tested using a t-test (paired, bilateral). **: 99% confidence level.

Experiment 2-2: UV-induced erythema

Fig. 5-6 shows average values for all subjects for reflectance and translucency index spectra measured before and 1 day after treatment. Reflectance and translucency index were both decreased 1 day after treatment at a wavelength of around 550 nm compared with before treatment. On the other hand, at around 650 nm, reflectance was almost the same as before and translucency index was increased. Fig. 5-7 shows values at 550 nm and 650 nm extracted from the spectra. At 550 nm, both reflectance and translucency index values decreased significantly (99% confidence level). At 650 nm, reflectance was barely changed, but translucency index was significantly increased (95% confidence level) after 1 day compared with before irradiation.

Changes at 550 nm are reasonable from a qualitative perspective. Reflectance decreased at a wavelength of 550 nm after 1 day as a result of erythema with a peak at 24-48 h [117]. Decreases in reflectance at a wavelength of 550 nm can be explained by the absorption spectrum of hemoglobin, which has strong peak at around 500-600 nm

[118, 119]. The fact that translucency index also decreased can be explained by the depth reached by light and the degree to which this light contributes to diffusion. Hemoglobin present at a certain depth selectively absorbs the component of incident light that contributes to diffusion. Therefore, when reflectance decreases as a result of absorption by pigment, translucency index also simultaneously decreases.

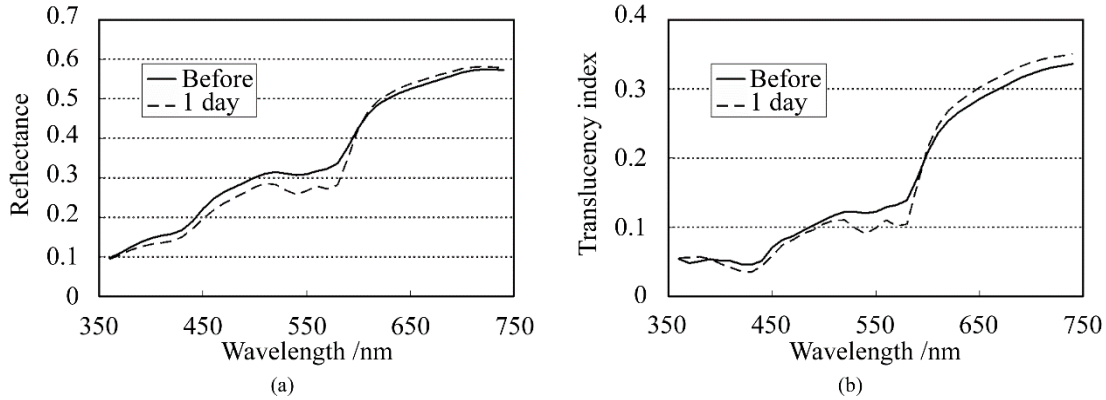

Fig. 5-6 Comparison of before and 1 day after UV irradiation. (a) r_A; (b) $T_{A,C}$. Solid lines: before irradiation; dashed lines: 1 day after irradiation. Values represent mean values for all subjects. Both r_A and $T_{A,C}$ decreased at a wavelength of around 550 nm after 1 day compared with before irradiation. On the other hand, $T_{A,C}$ increased while r_A was barely changed at 650 nm.

Although scattering power might also be changed in accordance with changes in thickness under conditions of erythema, the decrease in translucency index at 550 nm hardly seems to be explained by variations in scattering power. Vascular dilation under conditions of erythema [117] can cause thickening of the skin and variations in scattering power. If we consider the fact that translucency was increased at 650 nm, at which the extinction coefficient of oxyhemoglobin is two orders of magnitude smaller [59] than the

value at 550 nm and hemoglobin density has less effect on translucency than at 550 nm, scattering power should be changed in the direction of increasing translucency.

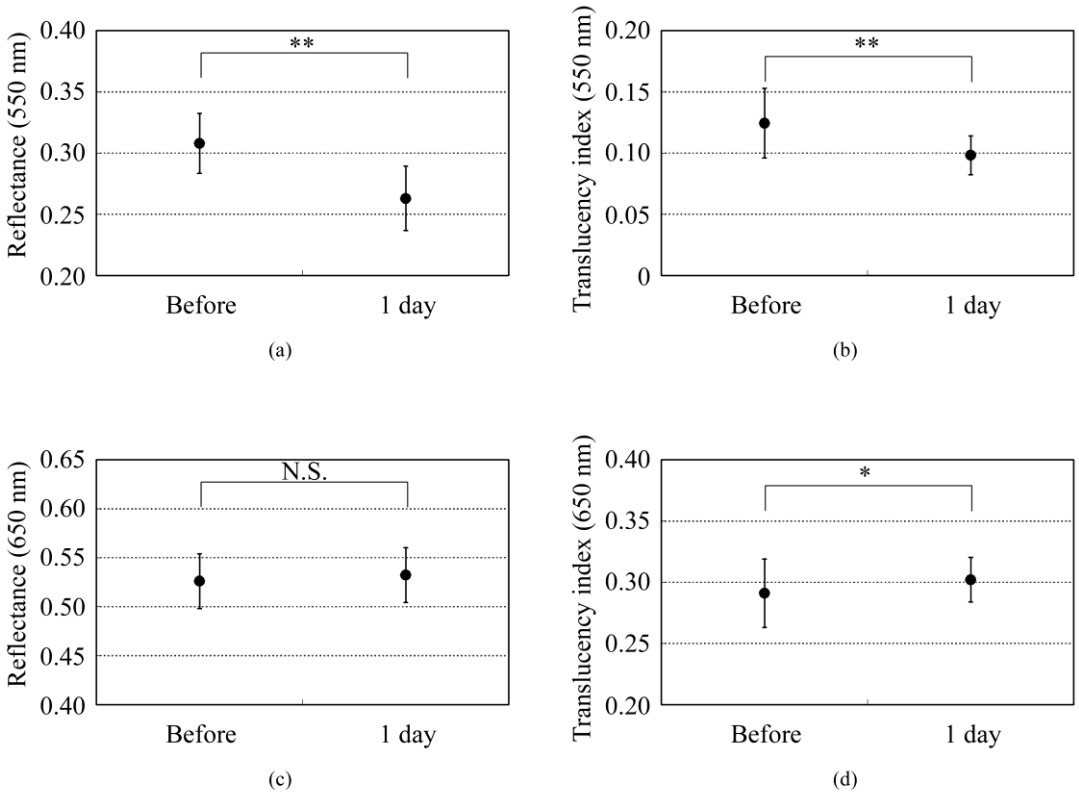

Fig. 5-7 Values at 550 nm and 650 nm extracted from spectra before and 1 day after UV irradiation. (a) r_A at 550 nm; (b) $T_{A,C}$ at 550 nm; (c) r_A at 650 nm; (d) $T_{A,C}$ at 650 nm. Significance was tested using a t-test (paired, bilateral). **: 99% confidence level, *: 95% confidence level, N.S.: not significant.

The order of translucency index of skin and translucent samples using the proposed method are consistent with the order of μ_{eff} by VRM. From the results of Experiment 2, in which translucency index of skin was approximately 0.3 at 650 nm (Fig. 5-5b, Fig. 5-7d), and the result of Experiment 1, we can say that forearm skin in Japanese individuals

shows a translucency between 0.20 wt% and 0.50 wt%. The order of translucency is thus consistent with the order from VRM mentioned in Sec. 5.2.5.

Lastly, as an evaluation of the possibilities of the proposed method, absorption coefficients (μ_a) and effective scattering coefficients (μ_s') were roughly estimated from the reflectances (r_A) and translucency indices ($T_{A,C}$) of the result in Experiment 2. Given PSF as a function of the parameters μ_a and μ_s', and given specific values of each parameter, we can derive reflectance and translucency index with Eq. 5-4 and 5-8, substituting PSF into $R \cdot p\left(\left|\vec{x}_o - \vec{x}_i\right|\right)$. Inversely, μ_a and μ_s' can be derived from reflectance and translucency index as an optimization problem. The formula proposed by Farrel et al. [18, 21, 67] was used as the PSF, as a function of μ_a, μ_s', refractive index and the distance from the incident point. The refractive index was set at 1.3, as used by Jensen et al. [67] The parameters μ_a and μ_s' were calculated from r_A and $T_{A,C}$, using the 'fminsearch' function in MATLAB software (Mathworks, Natick, MA, USA), in which the Nelder-Mead simplex method is implemented, to solve the optimization problem.

The specific values of the results in Experiment 2 and the derived values of μ_a and μ_s' (in mm^{-1}) from these results are shown in Table 5-2. The large increases seen in μ_s' after A/E treatment (from 2.80 to 3.88) and in μ_a after UV-induced erythema (from 0.49 to 0.81) can be anticipated as natural results from changes in the skin. Each calculated μ_a and μ_s' at 'before' at 650 nm and at 550 nm is generally larger (but not

exceeding a ten-fold increase) than the respective values at the red channel (for 650 nm) and green channel (for 550 nm) according to Jensen et al. [67]. The differences are supposed to come not only from differences between subjects, but also from inadequate handling of standard white and surface reflection. We think that more appropriate treatment of these issues will increase the reliability of the derived optical properties.

Table 5-2 Estimated values of μ_a and μ_s' from the results (r_A, $T_{A,C}$) in Experiment 2.

		Input		Output	
		r_A	$T_{A,C}$	μ_a /mm^{-1}	μ_s' /mm^{-1}
Experiment 2-1 (A/E treatment) at 650 nm					
	Before	0.56	0.28	0.049	2.80
	After	0.59	0.23	0.057	3.88
Experiment 2-2 (UV-induced erythema) at 550 nm					
	Before	0.31	0.12	0.49	3.61
	1 day	0.26	0.10	0.81	3.84

Limitations of this measurement method

The limitations that we have identified thus far are as follows.

First, this method cannot deal with the anisotropy of translucency. Although a previous study showed that skin translucency is anisotropic [69], the translucency index that this method derived represents the average over all directions. This method cannot deal with anisotropy due to the isotropic shape of the aperture.

A second issue is that the translucency of the standard white plate influences translucency index values. In the proposed method, the standard white plate is not only

the standard for white, but also the standard for opacity. When calculating reflectance according to Eq. 5-7, reflectance of the standard white plate is assumed to be constant even under different conditions. If the standard white plate is not completely opaque, however, reflectance will not be constant in the same way as for other translucent samples. If we want to obtain translucency indices of samples as absolute values or to compare indices of different instrument, the opacity of the standard for white should be corrected.

The third point to consider is that surface reflection is not completely excluded in measurements. When gauging the internal condition of the skin, it is desirable to separate reflected light from the skin into surface reflection and inner reflection, and to calculate the degree of diffusion of inner reflection. Eliminating surface reflection would require adoption of a method such as polarization analysis [42, 98].

5.4. Conclusion

We have proposed a method for evaluating translucency by measuring reflectance under two different types of measurement conditions. Although the proposed method cannot lead to the determination of scattering and absorption coefficients by itself, translucency can be measured as a lateral spread, which was our aim, and some advantages appear to be offered over conventional methods. The signals to be detected in this method are the convolutions over the illumination and measurement areas, and are unlikely to be an order of magnitude smaller than the total amount of reflection. This method is thus expected to be less susceptible to the influence of stray light and skin unevenness. In addition, this method uses almost the same geometric condition as standard spectral reflectance measurement, allowing simultaneous measurement of translucency and reflectance. Furthermore, the translucency index can be measured as a spectrum that also provides

useful information for detailed discussions, as we tried to consider the effect of scattering in Experiment 2-2. At present, in cases of skin appearance evaluation where eventual effects of translucency are of concern, this method can obtain sufficient information. If the values of the optical properties from the preliminary method we examined are related to those from conventional methods, the method would be applicable as a practical tool for deriving these coefficients.

6. Rapid calculation of diffuse reflectance from a multilayered model

6.1. Introduction

The reflectance of skin noninvasively provides information about the inner conditions, such as the scattering coefficients, absorption coefficients, and chromophore concentrations [71]. When deriving this information, a Monte Carlo simulation (MCS) has often been used as the standard [72-79], since a MCS precisely follows the behavior of each photon that is scattered from or absorbed in a medium, and the range of scattering and absorption coefficients to which it can be applied is not limited. In addition, a MCS can be applied easily to arbitrary multilayered structures. A multilayered structure is unavoidable when evaluating the reflectance of skin, which consists of an epidermis that contains melanin and an underlying dermis that contains hemoglobin. Because of its high reliability, a MCS is often used to evaluate approximation methods [72-79], although it has a high computation time. In a MCS, a large number of photons are generated, and each photon numerically propagates through the skin model following designated probabilities of scattering and absorption; from a statistical analysis of these results, the reflectance and other physical quantities are then calculated. Increasing the number of

photons increases the precision of the MCS, but it also increases the calculation time, which may become too long to be used for the inverse problem, imaging, or interactive tools. A sufficiently short calculation time is crucial for those applications, since it is necessary to calculate the reflectance many times. Therefore, to shorten the calculation time, several methods have been considered for approximating the results of an MCS. For example, various studies have proposed diffusion approximation [73], hybrid diffusion and two-flux approximation [74], the path-integral method [72], and an empirical method aided by MCS [40]. However, in each of these methods, the difference from the MCS depends on the type of approximation, and often the applicable range of parameters is limited. The methods based on the diffusion approximation [73, 74] limit the size of the ratio of the absorption coefficient μ_a to the reduced scattering coefficient μ_s'. In the path-integral method, although the trajectories of the light are represented by the classical path, it is difficult to find an appropriate path for the various absorption and scattering coefficients [72]. Finally, although the empirical method aided by a MCS can estimate the chromophore concentrations over a wide range, it cannot estimate the reflectance [40].

Several studies have attempted to reduce the time required to calculate the reflectance while keeping the results equivalent to those of an MCS [75-77, 79, 80]. These studies were based on a method known as white MCS (WMCS) [75] or single MCS [76, 77, 79], which were primarily developed for solving time-domain problems [75-77, 79]. The WMCS is based on the Beer-Lambert (B-L) law, which states that the absorbance of photons traveling through a medium along a certain trajectory can be calculated from the path length and the absorption coefficient. The WMCS also utilizes similarity: In a semi-infinite and homogeneous medium without absorption, if μ_s' grows to α times the

original condition, then a homothetic trajectory that is $1/\alpha$ times smaller can be associated with the original one [75, 76]. With similarity, we only need to calculate the MCS one time without absorption, and then for any absorption and scattering coefficient of the medium, we can derive a histogram for the path length and determine the spatial distribution of reflectance in the time domain. Not apply only to semi-infinite and homogeneous media, a WMCS can be applied to an arbitrary composite structure composed of multiple media if the path length in each medium can be calculated for each trajectory [78, 80]. However, in such cases, similarity cannot be fully utilized, and the application range for a certain precalculated data set is limited. For a multilayered structure like skin, the optical path-length matrix method (OPLM) has been developed [78]. In the OPLM, a MCS is used to determine the path lengths for each photon in the epidermis and in the dermis; this is recorded on a two-dimensional histogram. The absorption coefficient is determined, and the reflectance is then calculated from the two-dimensional histogram by using the B-L law [78]. Although this method works with a multilayer model, if we want to change any of the scattering coefficients or the thickness of any of the layers, we must recalculate everything.

To resolve this issue, we developed a faster method for estimating the reflectance of an arbitrary multilayered model; its results are in close agreement with those of the MCS. Here, we omit the spatial and time-resolved information. In this method, the WMCS was modified for application to a slab by the introduction of transition matrices for light flow without absorption from the incident angle to the exit angle, based on the distribution by path length. The method is called the layered WMCS (LWMCS). Once the value is given for μ_a, the transition matrices for each layer can be calculated for that μ_a. The transition matrices of all the layers are then combined by using the adding-doubling (AD)

method [120]. From the previously calculated values, the transition matrices can be derived for all the layers by matrix arithmetic; the calculation time is thus substantially shorter than it is with the conventional MCS (cMCS). In addition, with this method, we can change the number of layers, the thickness, μ_a, μ_s', and the refractive indices without having to repeat the initial calculations. To demonstrate the benefit of the quicker calculation, we used this method to estimate the chromophore content, which requires repeated calculations of the reflectance.

6.2. Theory

6.2.1. Outline of the method

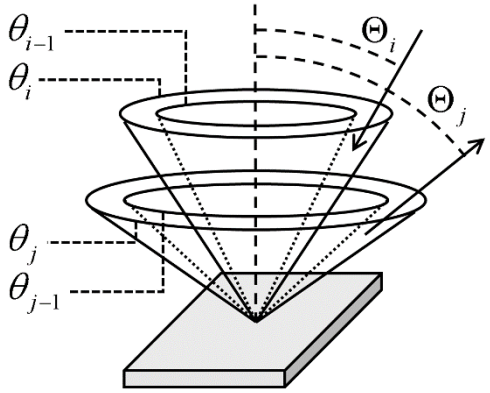

Fig. 6-1 Range of direction of incident angle Θ_i and exit angle Θ_j. Here, Θ_i and Θ_j indicate the direction between the two respective cones of θ_{i-1} and θ_i, and of θ_{j-1} and θ_j, respectively.

In this paper, we focus on the incoming angle of the light, measured in relation to the normal to the surface, and we exclude any analysis of lateral distribution or time. We begin by deriving the transition matrices of reflectance **R** and transmittance **T**, which are

based on the transition probability relative to the incident and exit angles. The incident and exit angles are separated by the angles $\{\theta_0,\theta_1,\ldots,\theta_{n-1},\theta_n\}$, where θ_0=0° and θ_n=90°. For convenience, the ranges $[\theta_{i-1},\theta_i]$ and $[\theta_{j-1},\theta_j]$ are represented by Θ_i and Θ_j, respectively, where i=1,2,…,n and j=1,2,…,n (Fig. 6-1). **R** and **T** are expressed as:

$$\mathbf{R}=\begin{pmatrix} R(\Theta_1\rightarrow\Theta_1) & \cdots & R(\Theta_n\rightarrow\Theta_1) \\ \vdots & \ddots & \vdots \\ R(\Theta_1\rightarrow\Theta_n) & \cdots & R(\Theta_n\rightarrow\Theta_n) \end{pmatrix}, \tag{6-1}$$

$$\mathbf{T}=\begin{pmatrix} T(\Theta_1\rightarrow\Theta_1) & \cdots & T(\Theta_n\rightarrow\Theta_1) \\ \vdots & \ddots & \vdots \\ T(\Theta_1\rightarrow\Theta_n) & \cdots & T(\Theta_n\rightarrow\Theta_n) \end{pmatrix}. \tag{6-2}$$

Here, $R(\Theta_i\rightarrow\Theta_j)$ and $T(\Theta_i\rightarrow\Theta_j)$ represents the discretized conditional probability of the exit angle being between $[\theta_{j-1},\theta_j]$ when the incident angle is Θ_i, for reflection and transmission, respectively. $R(\Theta_i\rightarrow\Theta_j)$ and $T(\Theta_i\rightarrow\Theta_j)$ can be expressed using the conditional probability densities:

$$R\left(\Theta_i\rightarrow\Theta_j\right)=\int_{\theta_{j-1}}^{\theta_j} r\left(\Theta_i\rightarrow\theta\right)d\theta, \tag{6-3}$$

$$T\left(\Theta_i\rightarrow\Theta_j\right)=\int_{\theta_{j-1}}^{\theta_j} t\left(\Theta_i\rightarrow\theta\right)d\theta. \tag{6-4}$$

Here, $r(\Theta_i\rightarrow\theta_j)$ and $t(\Theta_i\rightarrow\theta_j)$ are, respectively, the conditional probability densities of the exit angle θ_j when the incident angle is Θ_i, for reflectance and transmittance. We should note that, for simplicity, these values are not normalized to a solid angle, but they can be converted to normalized values if needed. Although the expression does not consider the azimuth angle, the reflectance and transmittance can be derived from these matrices, under the condition that either or both the incident angle and measurement angle distributions are axially symmetric. This precondition will be satisfied in the case of

normal or diffuse incidence, or when the reflected light is gathered with an integrated sphere.

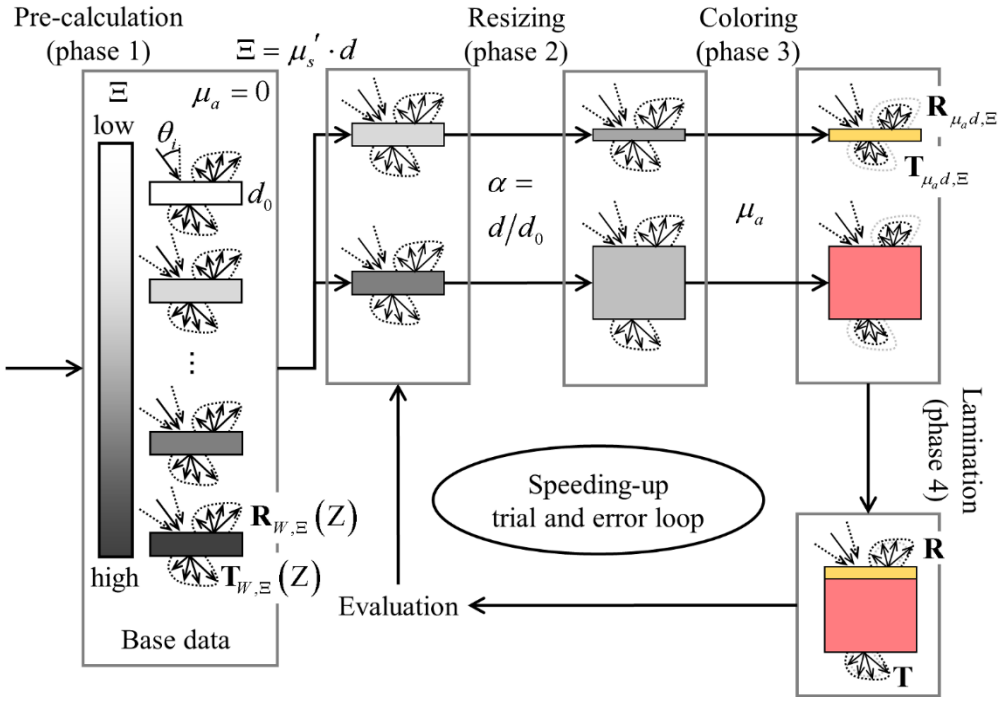

Fig. 6-2 Conceptual diagram of the layered white Monte Carlo simulation (LWMCS).

To derive **R** and **T** for a model of skin, we developed the LWMCS (Fig. 6-2). In the LWMCS, the transition matrices of reflection and transmission involving path lengths without absorption are calculated in advance by a MCS for several μ_s's for a specific thickness (phase 1, Sec. 6.2.2). In this case, each element of each of the transition matrices is a histogram of the path lengths. For an arbitrary μ_s', the thickness of a layer d can be associated with one from the precalculated base data by using a scale factor; this step is called *resizing* (phase 2, Sec. 6.2.3). To take account of μ_a, the B-L law was used, and the absorbance for a certain path length was derived from μ_a and the path length. The intensity for each path length was calculated, and these values were then accumulated. This phase is called *coloring* (phase 3, Sec. 6.2.4). Since the

accumulation is done across all path length, the results are in the form of Eq. 6-1 and Eq. 6-2 (i.e., each element becomes a scalar). Then, from the derived transition matrices of each layer, the transition matrices of the multilayered model can be calculated by using the AD method [120]; this is called *lamination* (phase 4, Sec. 6.2.5). The refractive index is not considered in the first three phases, but it is considered in phase 4. The protocol described above is called the generalized LWMCS (gLWMCS).

We will now discuss resizing in detail. Since, from similarity, the transition matrices can be associated with the product of μ_s' and d, it is not necessary that d has the same thickness as d_0 in the precalculation. Thus, the ratio α of d to d_0 is calculated and is used as a scaling factor. The concept of similarity is described as follows. The transition matrices for the case with reduced scattering coefficient μ_s'/α, absorption coefficient μ_a/α, and thickness $d\cdot\alpha$ are the same as those for μ_s', μ_a, and d, where α is an arbitrary factor. The probability that a photon follows an arbitrary trajectory magnified by α, with μ_s'/α, μ_a/α, and $d\cdot\alpha$ is the same as that of a photon following the original trajectory in a layer with μ_s', μ_a, and d (Fig. 6-3) [75, 76]. This means that the transition matrices in phase 1 can be expressed as a function of the normalized reduced scattering coefficient $\xi=\mu_s'\cdot d$ and the scale factor $\alpha=d/d_0$. The form of the transition matrices as a function of ξ do not change with α, while ξ changes not only with μ_s' but also with d. Therefore, if the transition matrices for the series of $\xi=\{\Xi_1, \Xi_2,\ldots, \Xi_m\}$ are prepared as in phase 1, appropriate transition matrices can be derived for arbitrary μ_s', μ_a, and d. Although Ξ_i has a discrete value, we can derive **R** and **T** for a given ξ by interpolating between the largest and smallest values of ξ in Ξ_i in phase 3.

Phase 1 requires repeated evaluations of a MCS; however, once the parameters of a multilayered model are defined, the reflectance can be calculated quickly. This allows us to shorten the trial-and-error process of adjusting the parameters. The method can also be applied to optimization problems that require recursive calculations of the reflectance; an example of this would be estimating chromophore concentrations.

To estimate the error of the interpolation as a function of ξ in gLWMCS, we also examined a specified LWMCS (sLWMCS). In an sLWMCS, the transition matrices from phase 1 are specified for a particular μ_s' and d in the model used; this means that the interpolation in phase 3 is not necessary. However, phase 1 must be repeated when μ_s' or d are changed in any layer.

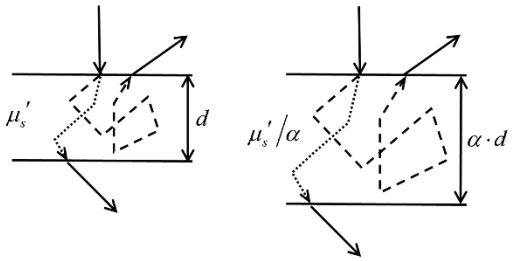

Fig. 6-3 Schematic of similarity. The left and right images are homothetic, and the scale factor is α. Homothetic trajectories have the same probability.

6.2.2. Precalculation of the transition matrices of a single layer (phase 1)

The aim of phase 1 is to use the path length without absorption to calculate **R** and **T** for each layer and for several different scattering powers. The results will then be used to quickly derive **R** and **T** for layers with an arbitrary absorption coefficient. Assuming a path length l and layer thickness d_0, the normalized path length $\zeta = l/d_0$ can be separated as $\{\zeta_0,\zeta_1,\ldots,\zeta_{m-1}, \zeta_m\}$ where $\zeta_0=0$ and $\zeta_m=\infty$. For convenience, the range $[\zeta_{j-1},\zeta_j]$ is

represented by Z_j, where j=1,2,…,m. A single MCS produced one column each of **R** and **T** for path lengths without absorption and for a particular pair of Θ_i and ξ, as follows:

$$\mathbf{R}_{W,\xi}(\Theta_i)=\begin{pmatrix} R_{W,\xi}(\Theta_i\rightarrow\Theta_1,Z_1) & \cdots & R_{W,\xi}(\Theta_i\rightarrow\Theta_1,Z_m) \\ \vdots & \ddots & \vdots \\ R_{W,\xi}(\Theta_i\rightarrow\Theta_n,Z_1) & \cdots & R_{W,\xi}(\Theta_i\rightarrow\Theta_n,Z_m) \end{pmatrix}, \tag{6-5}$$

$$\mathbf{T}_{W,\xi}(\Theta_i)=\begin{pmatrix} T_{W,\xi}(\Theta_i\rightarrow\Theta_1,Z_1) & \cdots & T_{W,\xi}(\Theta_i\rightarrow\Theta_1,Z_m) \\ \vdots & \ddots & \vdots \\ T_{W,\xi}(\Theta_i\rightarrow\Theta_n,Z_1) & \cdots & T_{W,\xi}(\Theta_i\rightarrow\Theta_n,Z_m) \end{pmatrix}. \tag{6-6}$$

Here, $R_{W,\xi}(\Theta_i\rightarrow\Theta_j,Z_k)$ and $T_{W,\xi}(\Theta_i\rightarrow\Theta_j,Z_k)$ are the conditional probabilities that the exit angle and the path length are between $[\theta_{j-1},\theta_j]$ and $[\zeta_{k-1}, \zeta_k]$, respectively, when the incident angle is Θ_i. The subscript W represents white (no absorption). Each row in $\mathbf{R}_{W,\xi}(\Theta_i)$ and $\mathbf{T}_{W,\xi}(\Theta_i)$ forms a histogram of the path length. In sLWMCS, the particular values of ξ in the skin model are used for the precalculation. However, in the gLWMCS, the value of ξ used in the precalculation was not the same as the value used in the model.

6.2.3. Resizing the thickness of a layer (phase 2)

In phase 2, an appropriate set of transition matrices is chosen. For a particular layer with μ_s' and d, we choose the precalculated data set with $\xi=\mu_s'\cdot d$. In the sLWMCS, the transition matrices for the particular ξ in the skin model are calculated in phase 1. In the gLWMCS, the minimum Ξ_i larger than ξ and the maximum Ξ_i smaller than ξ are chosen, and the results are then interpolated in phase 3.

6.2.4. Coloring of transition matrices for a single layer (phase 3)

In the sLWMCS, the absorbance for a particular absorption coefficient and path length can be calculated in accordance with the B-L law. Assuming that an absorption

coefficient μ_a, thickness d, and normalized path length $\zeta=l/d$ are given, the absorbance A can be expressed using the normalized absorption coefficient $\mu_a \cdot d$ as $A=\exp\left(-\mu_a d\cdot\zeta\right)$. Therefore, the total amount of reflected and transmitted light can be expressed as a function of the angle, as follows:

$$\begin{aligned}\vec{\mathbf{R}}_{\mu_a d,\zeta}(\Theta_i)&=\begin{pmatrix}R_{\mu_a d,\zeta}(\Theta_i\rightarrow\Theta_1)\\ \vdots \\ R_{\mu_a d,\zeta}(\Theta_i\rightarrow\Theta_n)\end{pmatrix}=\mathbf{R}_{W,\zeta}(\Theta_i)\cdot\vec{\mathbf{A}}(\mu_a d)\\ &=\begin{pmatrix}R_{W,\zeta}(\Theta_1\rightarrow\Theta_1,Z_1) & \cdots & R_{W,\zeta}(\Theta_n\rightarrow\Theta_1,Z_m)\\ \vdots & \ddots & \vdots \\ R_{W,\zeta}(\Theta_1\rightarrow\Theta_n,Z_1) & \cdots & R_{W,\zeta}(\Theta_n\rightarrow\Theta_n,Z_m)\end{pmatrix}\begin{pmatrix}e^{-\mu_a d\cdot Z_1}\\ \vdots \\ e^{-\mu_a d\cdot Z_m}\end{pmatrix},\end{aligned} \tag{6-7}$$

$$\begin{aligned}\vec{\mathbf{T}}_{\mu_a d,\zeta}(\Theta_i)&=\begin{pmatrix}T_{\mu_a d,\zeta}(\Theta_i\rightarrow\Theta_1)\\ \vdots \\ T_{\mu_a d,\zeta}(\Theta_i\rightarrow\Theta_n)\end{pmatrix}=\mathbf{T}_{W,\zeta}(\Theta_i)\cdot\vec{\mathbf{A}}(\mu_a d)\\ &=\begin{pmatrix}T_{W,\zeta}(\Theta_1\rightarrow\Theta_1,Z_1) & \cdots & T_{W,\zeta}(\Theta_n\rightarrow\Theta_1,Z_m)\\ \vdots & \ddots & \vdots \\ T_{W,\zeta}(\Theta_1\rightarrow\Theta_n,Z_1) & \cdots & T_{W,\zeta}(\Theta_n\rightarrow\Theta_n,Z_m)\end{pmatrix}\begin{pmatrix}e^{-\mu_a d\cdot Z_1}\\ \vdots \\ e^{-\mu_a d\cdot Z_m}\end{pmatrix}.\end{aligned} \tag{6-8}$$

These vectors become columns of the transition matrices for the associated incident angle. If we calculate $\vec{\mathbf{R}}_{\mu_a d,\zeta}$ and $\vec{\mathbf{T}}_{\mu_a d,\zeta}$ for all incident angles and then combine them, the transition matrices of a layer with an arbitrary absorption coefficient are derived as:

$$\begin{aligned}&\mathbf{R}_{\mu_a d,\zeta}\\ &=\left(\vec{\mathbf{R}}_{\mu_a d,\zeta}(\Theta_1)\ \cdots\ \vec{\mathbf{R}}_{\mu_a d,\zeta}(\Theta_n)\right)=\begin{pmatrix}R_{\mu_a d,\zeta}(\Theta_1\rightarrow\Theta_1) & \cdots & R_{\mu_a d,\zeta}(\Theta_n\rightarrow\Theta_1)\\ \vdots & \ddots & \vdots \\ R_{\mu_a d,\zeta}(\Theta_1\rightarrow\Theta_n) & \cdots & R_{\mu_a d,\zeta}(\Theta_n\rightarrow\Theta_n)\end{pmatrix},\end{aligned} \tag{6-9}$$

$$\mathbf{T}_{\mu_a d,\xi} = \left(\vec{\mathbf{T}}_{\mu_a d,\xi}(\Theta_1) \quad \cdots \quad \vec{\mathbf{T}}_{\mu_a d,\xi}(\Theta_n)\right) = \begin{pmatrix} T_{\mu_a d,\xi}(\Theta_1 \to \Theta_1) & \cdots & T_{\mu_a d,\xi}(\Theta_n \to \Theta_1) \\ \vdots & \ddots & \vdots \\ T_{\mu_a d,\xi}(\Theta_1 \to \Theta_n) & \cdots & T_{\mu_a d,\xi}(\Theta_n \to \Theta_n) \end{pmatrix}. \tag{6-10}$$

In the sLWMCS, a particular ξ in the skin model is used in phase 1, therefore the transition matrices can be simply calculated from Eq. 6-9 and 6-10. In the gLWMCS, the value of ξ in the model does not usually match the value of ξ used in phase 1; instead, **R** and **T** are derived by interpolation. For a particular ξ, assuming that the transition matrices for Ξ_i were calculated in phase 1, the transition matrices for ξ are calculated by linear interpolation, as follows:

$$\mathbf{R}_{\mu_a d,\xi} = \frac{\Xi_+ - \xi}{\Xi_+ - \Xi_-}\mathbf{R}_{\mu_a d,\Xi-} + \frac{\xi - \Xi_-}{\Xi_+ - \Xi_-}\mathbf{R}_{\mu_a d,\Xi+}, \tag{6-11}$$

$$\mathbf{T}_{\mu_a d,\xi} = \frac{\Xi_+ - \xi}{\Xi_+ - \Xi_-}\mathbf{T}_{\mu_a d,\Xi-} + \frac{\xi - \Xi_-}{\Xi_+ - \Xi_-}\mathbf{T}_{\mu_a d,\Xi+}, \tag{6-12}$$

where Ξ_+ is the minimum Ξ_i larger than ξ, and Ξ_- is the maximum Ξ_i smaller than ξ.

6.2.5. Lamination of layers with the adding-doubling method (phase 4)

We will number the layers from the top down. We will not allow the refractive index to change at the boundaries, and instead, any change in the refractive index will be considered to take place in a virtual layer. This means when there is a change in the refractive index, the boundary (in the usual sense) should be counted twice, and the effect of the refractive index ratio is treated as a characteristic of a virtual layer at that location. **R**, **T** and L are defined as in Fig. 6-4a. The notation of the transition matrix is expanded

to multiple layers, and the transition matrix of the combined layers, from boundaries k to l, are expressed as $\mathbf{R}^{k:l}$ and $\mathbf{T}^{k:l}$ (Fig. 6-4b).

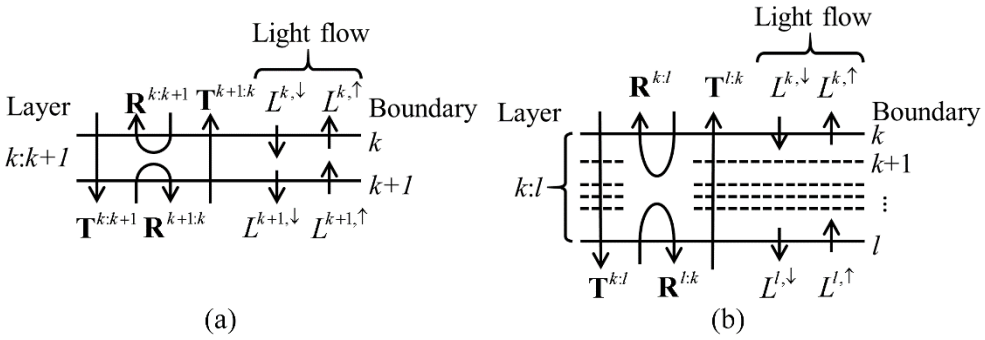

Fig. 6-4 Notation of **R**, **T**, and the light flow L. (a) Notation for a layer between boundaries k and k+1. (b) Notation for a composition of layers between boundaries k to l.

Our aim in phase 4 is to derive the matrix $\mathbf{R}^{1:N}$ that contains the transition probability from an arbitrary incident angle to an arbitrary exit angle for the layers with boundaries 1 to N. We begin by combining two pairs of transition matrices of two adjacent layers into a single pair of transition matrices. Then, by using recursion, the transition matrices of an arbitrary number of layers can be combined into a pair of transition matrices.

The reflection and transmission transition matrices for a layer between the boundaries k and k+1 (Fig. 6-4) can be written as:

$$\mathbf{R}^{k:k+1} = \begin{pmatrix} R^{k:k+1}(\Theta_1 \to \Theta_1) & \cdots & R^{k:k+1}(\Theta_n \to \Theta_1) \\ \vdots & \ddots & \vdots \\ R^{k:k+1}(\Theta_1 \to \Theta_n) & \cdots & R^{k:k+1}(\Theta_n \to \Theta_n) \end{pmatrix}, \tag{6-13}$$

$$\mathbf{T}^{k:k+1} = \begin{pmatrix} T^{k:k+1}(\Theta_1 \to \Theta_1) & \cdots & T^{k:k+1}(\Theta_n \to \Theta_1) \\ \vdots & \ddots & \vdots \\ T^{k:k+1}(\Theta_1 \to \Theta_n) & \cdots & T^{k:k+1}(\Theta_n \to \Theta_n) \end{pmatrix}. \tag{6-14}$$

Here, $R^{k:k+1}(\Theta_i \rightarrow \Theta_j)$ and $T^{k:k+1}(\Theta_i \rightarrow \Theta_j)$ represent the discretized conditional transition probability of reflected and transmitted light, respectively, and they can be expressed as:

$$R^{k:k+1}\left(\Theta_i \rightarrow \Theta_j\right) = \int_{\theta_{j-1}}^{\theta_j} r^{k:k+1}\left(\Theta_i \rightarrow \theta\right) d\theta, \tag{6-15}$$

$$T^{k:k+1}\left(\Theta_i \rightarrow \Theta_j\right) = \int_{\theta_{j-1}}^{\theta_j} t^{k:k+1}\left(\Theta_i \rightarrow \theta\right) d\theta, \tag{6-16}$$

in the same manner as in Eqs. 6-3 and 6-4. Here, $r^{k:k+1}(\Theta_i \rightarrow \theta)$ and $t^{k:k+1}(\Theta_i \rightarrow \theta)$ are the conditional probability density of the exit angle of reflected and transmitted light, respectively, when the incident angle is Θ_i.

Assuming depolarized light, the transition matrix of a virtual layer k:k+1 with a change in refractive indices (a single boundary in the usual sense) can be derived by using the Fresnel equation. If $1 \geq N_1 \cdot \sin\Theta_i / N_2$, where N_1 and N_2 are the refractive index of the reflected side and the transmitted side, respectively, the transition matrix for reflectance can be expressed as follows:

$$\begin{aligned} & R^{k:k+1}\left(\Theta_i \rightarrow \Theta_j\right) \\ & = \delta_{i,j} \frac{\left(\sin\left(\Theta_i - \mathrm{B}_i\right)/\sin\left(\Theta_i + \mathrm{B}_i\right)\right)^2 + \left(\tan\left(\Theta_i - \mathrm{B}_i\right)/\tan\left(\Theta_i + \mathrm{B}_i\right)\right)^2}{2}. \end{aligned} \tag{6-17}$$

Here, B_i is the transmission angle, which can be derived by using Snell's law ($\sin \mathrm{B}_i = N_1 \cdot \sin\Theta_i / N_2$), and $\delta_{i,j}$ is the Kronecker delta. With regard to the transition matrix for transmission, the following relationship is useful:

$$\sum_{j=1}^{n} T^{k:k+1}\left(\Theta_i \rightarrow \Theta_j\right) = 1 - R^{k:k+1}\left(\Theta_i \rightarrow \Theta_i\right). \tag{6-18}$$

The transition matrix of transmission can be derived if we assume the transmitted light is distributed uniformly across the range of $[\beta_{i-}, \beta_{i+}]$, where for the incident angles θ_{i-1} and θ_i, we have the transmission angles β_{i-} and β_{i+}, respectively. When $1 < N_1 \cdot \sin\Theta_i / N_2$,

which is the condition of total reflection, $R^{k:k+1}(\Theta_i \rightarrow \Theta_j)=\delta_{i,j}$ and $T^{k:k+1}(\Theta_i \rightarrow \Theta_j) = 0$ for $j=1,2,\ldots,n$.

The angular dependency of the light flow at a boundary k is expressed as $\vec{L}^{k,\downarrow}$ in the downward direction and $\vec{L}^{k,\uparrow}$ in the upward direction (Fig. 6-4). Here, $\vec{L}^{k,\downarrow}$ and $\vec{L}^{k,\uparrow}$ are vectors, and their i-th elements represent the flow toward Θ_i. Balancing the inflow and outflow leads to the following relationships involving $T^{1:2}$, $T^{2:1}$, $R^{1:2}$, $R^{2:1}$, and the light flow at the boundary 1:2:

$$\vec{L}^{2,\downarrow} = \mathbf{T}^{1:2} \cdot \vec{L}^{1,\downarrow} + \mathbf{R}^{1:2} \cdot \vec{L}^{2,\uparrow}, \tag{6-19}$$

$$\vec{L}^{1,\uparrow} = \mathbf{T}^{2:1} \cdot \vec{L}^{2,\uparrow} + \mathbf{R}^{1:2} \cdot \vec{L}^{1,\downarrow}. \tag{6-20}$$

We can obtain similar relationships for the boundary 2:3. In addition, by considering two layers to be one composited layer, we can obtain the same kind of equation for the composited boundary 1:3. By eliminating $L^{2,\downarrow}$ and $L^{2,\uparrow}$, noting that **R** and **T** are noncommutative, and noting that the equations should hold for arbitrary values of $\vec{L}^{1,\downarrow}$, $\vec{L}^{1,\uparrow}$, $\vec{L}^{3,\downarrow}$, and $\vec{L}^{3,\uparrow}$, $\mathbf{R}^{1:3}$ and $\mathbf{T}^{1:3}$ can be expressed in terms of $\mathbf{R}^{1:2}$, $\mathbf{R}^{2:1}$, $\mathbf{R}^{2:3}$, $\mathbf{T}^{1:2}$, $\mathbf{T}^{2:1}$, and $\mathbf{T}^{2:3}$ as follows:

$$\mathbf{R}^{1:3} = \mathbf{T}^{2:1} \cdot \left(\mathbf{E} - \mathbf{R}^{2:3} \cdot \mathbf{R}^{2:1}\right)^{-1} \cdot \mathbf{R}^{2:3} \cdot \mathbf{T}^{1:2} + \mathbf{R}^{1:2}, \tag{6-21}$$

$$\mathbf{T}^{1:3} = \mathbf{T}^{2:3} \cdot \left(\mathbf{E} - \mathbf{R}^{2:1} \cdot \mathbf{R}^{2:3}\right)^{-1} \cdot \mathbf{T}^{1:2}, \tag{6-22}$$

where **E** is the unit matrix. By interchanging 1 and 3, we can obtain similar equations for $\mathbf{R}^{3:1}$ and $\mathbf{T}^{3:1}$. Once $\mathbf{R}^{1:h}$ and $\mathbf{T}^{1:h}$ have been derived, by substituting $\mathbf{R}^{1:h}$, $\mathbf{R}^{h:h+1}$, $\mathbf{T}^{1:h}$, and $\mathbf{T}^{h:h+1}$ for $\mathbf{R}^{1:2}$, $\mathbf{R}^{2:3}$, $\mathbf{T}^{1:2}$, and $\mathbf{T}^{2:3}$, respectively, we obtain $\mathbf{R}^{1:h+1}$ and $\mathbf{T}^{1:h+1}$. We can obtain $\mathbf{R}^{h+1:1}$ and $\mathbf{T}^{h+1:1}$ in a similar way. Thus, the pairs of transition matrices can be derived recursively for an arbitrary number of layers.

6.3. Numerical investigation

6.3.1. Binning of path length

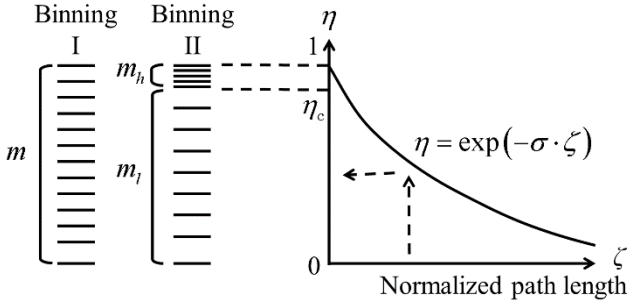

Fig. 6-5 Schematic of binning.

In the WMCS methods, including the LWMCS, it is important to optimize the bin width for the light path lengths such that the necessary computer resources and time are minimized but accuracy is maintained. The simplest method of binning is equal division, but this is not effective [79]. At short path lengths, a small difference in the path length reflects a large difference in absorption, and so the bin width should be narrow. On the other hand, when the path length is long, differences in the path length are not sensitive to differences in absorption, and so a narrow bin width results in a waste of computer resources and time. Therefore, in order to minimize the errors, the size of the database, and the processing time, the bin widths should be narrower for shorter path lengths and wider at longer path lengths. Note that whether a certain path length is long or short depends on the thickness and the scattering coefficient, so the degree of variation should be adjusted for this. We examined two types of binning that fulfilled this condition (Fig. 6-5).

6.3.1.1. Equal division of logarithm (Binning I)

For a particular constant σ_R, the normalized path length ζ is transformed into η_R=exp(σ_R×ζ), and the range of η_R (0 to 1) is divided equally into **R** bins. For **T**, since the path length is greater than or equal to the thickness of layer d, the path length was transformed into η_T=exp(σ_T×(ζ-1)), noting that ζ=l/d. By doing this, the bin widths of ζ for shorter path lengths became narrower than those for longer path lengths. Another benefit of the transformation is that the semi-infinite range of path lengths [0, ∞] is transformed to a finite range [0, 1], which enables fading of the binning. In particular, the divisions of the binning of η_R and η_T can be expressed as $\eta_j = j/m$, for j=0,…,m. The range [η_{j-1}, η_j] is now represented by $(2j-1)/2m$. We will call this *Binning I*.

6.3.1.2. Dual-partitioning of equal divisions of logarithm (Binning II)

Dual-partitioning is also examined, because the variation of the bin width in Binning I is gradual, and thus the narrowness of the bin widths may be insufficient to achieve high precision. This is done as follows: a certain point η_c is set between 0 and 1. The region from 0 to η_c and the region from η_c to 1 are then each divided separately into m_l or m_h sections, respectively. This binning can be characterized by four parameters (σ, η_c, m_l, and m_h). For **R** and **T**, the parameters are expressed as (σ_R, η_{cR}, m_{lR}, m_{hR}) and (σ_T, η_{cT}, m_{lT}, m_{hT}), respectively.

6.3.2. Skin model

We used a two-layered model: an epidermis with uniform melanin, and an underlying dermis with uniform oxygenated and deoxygenated hemoglobin; the thickness of the epidermis and dermis were 0.06 mm 4.94 mm, respectively. The refractive index was

assumed to be 1.4, independent of wavelength or layer. The refractive index of the external area was set to unity. The absorption coefficients of the epidermis and dermis were assumed to be $\varepsilon_m(\lambda)\cdot C_m$ and $\varepsilon_{oh}(\lambda)\cdot C_{oh}+\varepsilon_{dh}(\lambda)\cdot C_{dh}$, respectively. Here, C_m, C_{oh}, and C_{dh} are the concentrations in each layer of melanin, oxygenated hemoglobin, and deoxygenated hemoglobin, respectively. For $\varepsilon_m(\lambda)$, we used the average absorption coefficient of the monomer melanosome with a concentration of 1 mole/liter; this was approximated as $6.6\times10^{11}\times\lambda^{-3.33}$ in cm^{-1}, where the unit of λ was nm [89]. For ε_{oh} and ε_{dh}, we used the extinction coefficients of oxygenated and deoxygenated hemoglobin, respectively, converted to a hematocrit concentration of 45 [90]. The scales of C_m, C_{oh}, and C_{dh} were the ratio against the concentrations under which $\varepsilon_m(\lambda)$, $\varepsilon_{oh}(\lambda)$, and $\varepsilon_{dh}(\lambda)$, respectively, were derived. To characterize the scattering, the reduced scattering coefficient $\mu_s'(\lambda)$ is required; this was derived from $\mu_s'(\lambda)=\mu_s(\lambda)\times(1-g)$ with the scattering coefficient $\mu_s(\lambda)$ and asymmetry factor g, which are the primitive parameters of scattering [92]. The value of $\mu_s'(\lambda)$ for both the epidermis and dermis was $2\times10^5\times\lambda^{-1.5}+2\times10^{12}\times\lambda^{-4}$; the first term represents Mie scattering, the second one represents Rayleigh scattering [91-93], and the unit of λ is nm. Although g is known to be larger than 0 [92], for simplicity, g was assumed to be 0.

For the error estimation presented in Sec. 6.3.6.1, μ_a was set from 0 to $300cm^{-1}$ in intervals of $10cm^{-1}$ for the epidermis and was set from 0 to $30cm^{-1}$ in $1cm^{-1}$ intervals for the dermis. The range of μ_a from 0 to $300cm^{-1}$ of the epidermis covers 0 to 21% of C_m, and that from 0 to $30cm^{-1}$ of the dermis covers 0 to 1.1% of C_{oh}, and 0 to 1.0% of C_{dh} for wavelengths in the range of 400 to 700 nm. These concentrations are the actual values for skin that is light to moderately pigmented [93]. Other than μ_a, the parameters of the skin model in Sec. 6.3.6.1 were the same as those of the skin model described above.

6.3.3. MCS

For calculating the MCS, the program MCML [5] was modified to record the histograms of reflectance and transmittance against the path length, and to perform the calculations for an arbitrary incident angle. With the modified MCML, we executed the cMCS and phase 1 of the sLWMCS and gLWMCS. The number of photons for each condition was 10^5 [94]. For the standard condition for the skin model, the incident angle was set to 0°, and the reflectance was integrated over all exit angles.

6.3.3.1. Conventional MCS (cMCS)

As a standard, we used conventional MCS (cMCS). In the cMCS, the parameters μ_s', μ_a, d, and the refractive index of each layer, were set as described in Sec. 6.3.2, and photons were considered to travel in a multilayered model of skin.

6.3.3.2. sLWMCS

Following the procedure described in Sec. 6.2, we used a sLWMCS to calculate **R** and **T** for the skin model in Sec. 6.3.2. The divisions of binning for the incident angle and exit angle θ_i were both set to {0°,1°,…,89°,90°}, and the representative values Θ_i were defined as {0.5°,1.5°,…,88.5°,89.5°}. Both binning I (sLWMCS(I); Sec. 6.3.1.1) and binning II (sLWMCS(II); Sec. 6.3.1.2) were used. Phases 2 to 4 were executed using MATLAB® (Mathworks, Natick, MA, USA). The incident angle (for the whole model) was set to 0.5°, which approximated the 0° incidence angle of the standard condition.

As mentioned above, the appropriate values of σ_R and σ_T depend on the thickness and the scattering coefficient. The value of σ was determined visually to be such that the elements of the histogram did not concentrate in the lowest and highest bins (around 0 and 1 for η). For both the sLWMCS(I) and the sLWMCS(II), m was set to 100; and σ_R

and σ_T were set to 0.072 and 0.072, respectively, for the epidermis, and 0.3 and 0.049, respectively, for the dermis. For the sLWMCS(II), η_{cR} and η_{cT} were set to 0.97, m_{lR} and m_{lT} were set to 70, and m_{hR} and m_{hT} were set to 30.

6.3.3.3. gLWMCS

Following the procedure described in Sec. 6.2, **R** and **T** of the skin model in Sec. 6.3.2 were calculated by using the gLWMCS. The same values that were used for the sLWMCS (Sec. 6.3.3.2) were used for the discretization of the incident and exit angles. Binning II (Sec. 6.3.1.2) was used [gLWMCS(II)]. The value of Ξ_i was set to $10^{(i/10-1)}$ for i in the range of 0 to 30 in each interval, which means Ξ_i varied from 0.1 to 100 with equal intervals on a log scale. The range of Ξ_i is comparable to 16.7-16667cm^{-1} in μ_s' for d=0.06mm (where d is for the epidermis in our skin model), and to 0.2-202cm^{-1} in μ_s' for d=4.94mm (where d is for the dermis in our skin model). Since μ_s' is 103.13cm^{-1} at 400nm and monotonically decreases to 19.129cm^{-1} at 700nm in our skin model, the variation covers μ_s' in the epidermis and dermis at wavelengths from 400 to 700 nm. The MCS was repeated for each Ξ_i; this was achieved by setting d to 1 and μ_s' to Ξ_i in the modified MCML. Phases 3 and 4 were executed using MATLAB®.

The value of σ was defined visually to be such that the elements of the histogram did not concentrate in the lowest and highest bins (around 0 and 1 in the η); this was the same as for the sLWMCS. For the gLWMCS(II), σ_R was defined using the equation σ_R =0.06+0.024ξ, and σ_T was set to 0.06 for all ξ. For the gLWMCS(II), η_{cR} and η_{cT} were set to 0.97, m_{lR} and m_{lT} were set to 70, and m_{hR} and m_{hT} were set to 30; this was the same as for the sLWMCS(II).

6.3.4. Evaluation function

The relative error of reflectance from a method evaluated was defined as follows:

$$E = \frac{[\text{reflectance from a method evaluated}] - [\text{reflectance from cMCS}]}{[\text{reflectance from cMCS}]}. \quad (6\text{-}23)$$

6.3.5. Evaluation function for using the spectrum to estimate chromophore concentrations

To estimate the chromophore concentrations from a given spectrum $S(\lambda)$, the evaluation function to be minimized in the optimization problem was defined as follows:

$$F = \sum_{\lambda=400nm}^{700nm} \left(S(\lambda) - S(c_m, c_{oh}, c_{dh}; \lambda) \right)^2. \quad (6\text{-}24)$$

Here, $S(c_m, c_{oh}, c_{dh}; \lambda)$ is the estimated spectrum for a given chromophore concentration

6.3.6. Numerical experiments

6.3.6.1. Error estimation

To estimate the error, the skin model in Sec. 6.3.2 was used. For μ_s', we used the values at 400, 500, 600, and 700 nm, which were, respectively, 103.13, 49.889, 29.040, and 19.129 cm^{-1}. The value of μ_a for the epidermis was set to range from 0 to 300 in intervals of width 10, and μ_a for the dermis was set to range from 0 to 30 in intervals of width 1. We calculated E for the cMCS, sLWMCS(II), gLWMCS(II), and sLWMCS(I). For the cMCS, the reflectance was calculated twice under each condition (with different random number sequence), and the results from the second trial were used to evaluate the method. If we assume the sLWMCS(II) to be the standard, then the difference between that and the gLWMCS(II) demonstrates the effect of interpolation, and the difference between that and the sLWMCS(I) demonstrates the effect of binning.

A representative reflectance spectrum from our skin model was calculated with the cMCS, the sLWMCS(II), and the gLWMCS(II). The concentrations of melanin, oxygenated hemoglobin, and deoxygenated hemoglobin were set to 1%, 0.1%, and 0.1%, which are in the range of Asian skin.

The MCML for the cMCS and phase 1 of each LWMCS was executed on Windows 8® (64bit). The PC had 4 GB of memory, and the CPU was Core i5-3230M®, 2.60GHz (Intel, Santa Clara, CA, USA). For the calculation of phases 2 to 4 in the sLWMCS and gLWMCS, we used MATLAB® 7.0.4 on a Windows XP® emulator in a VMWare Player® 5.0.2 on Windows 8 (64bit); note that MATLAB® 7.0.4 does not work in Windows 8. Processing time was evaluated with the MATLAB profiler. Windows XP® and Windows 8® are products of Microsoft (Redmond, WA, USA), and VMWare Player® is the product of VMWare® (Palo Alto, CA, USA). The memory allocated to the Windows XP emulator was 2GB, and 3 of the 4 CPU cores were allocated to the emulator.

6.3.6.2. Estimating chromophore concentrations from a spectrum

The inverse problem, such as the estimation of chromophore concentrations, is where rapid calculations become important, because the spectrum must be calculated iteratively under several different conditions. From a given spectrum, we searched for the chromophore concentrations as an optimization problem that minimized the evaluation function F. The optimization problem was solved with the built-in function *fminsearch* of MATLAB, in which the Nelder-Mead simplex method is implemented. The skin model of Sec. 6.3.2 was used, and the wavelength was set from 400 to 700 nm at intervals of 10 nm.

With the spectrum from the cMCS as the input, we used the sLWMCS(II) and gLWMCS(II) to search for the chromophore concentrations that minimized F. The results were compared with the input of the cMCS. For the input of cMCS, the concentrations of melanin, oxygenated hemoglobin, and deoxygenated hemoglobin were set to 1%, 0.1%, and 0.1%, respectively, and the initial values of the iteration were set to 2%, 0.5%, and 0.5%, respectively. The tested concentrations were the same with those used in Sec. 6.3.6.1 as a representative spectrum. The processing time and number of iterations were evaluated with the MATLAB profiler.

6.4. Results

6.4.1. Error estimation

In Fig. 6-6, the values of E for the cMCS, sLWMCS(II), gLWMCS(II), and sLWMCS(I) are plotted against the cMCS, for the various conditions of μ_a in the epidermis and dermis. The average and standard deviation of E over the whole range of μ_a are shown in Table 6-1. On average, the absolute values of E for both the sLWMCS(II) and the gLWMCS(II) were one order of magnitude larger than those of the cMCS, but they were smaller than that from the sLWMCS(I). The standard deviation of E for both the sLWMCS(II) and the gLWMCS(II) were smaller than that for with the cMCS or the sLWMCS(I). Representative reflectance spectrums of the skin model with the cMCS, sLWMCS(II), and gLWMCS(II) are shown in Fig. 6-7. The processing time of the cMCS was 1531 sec. for the derivation of the spectrum (31 wavelengths). The processing time of phases 2 to 4 in the sLWMCS(II) and gLWMCS(II) were 3 sec. and 5 sec., respectively, for the derivation of each spectrum, which are, respectively, about 500

times and 300 times faster than that of the cMCS. As can be seen in Fig. 6-7, the skin reflectance spectrums from both the sLWMCS(II) and the gLWMCS(II) were practically identical to that from the cMCS. The difference between the cMCS and the sLWMCS(II) or gLWMCS(II) was more than two digits smaller than the reflectance, which reflects the precision shown in Table 6-1.

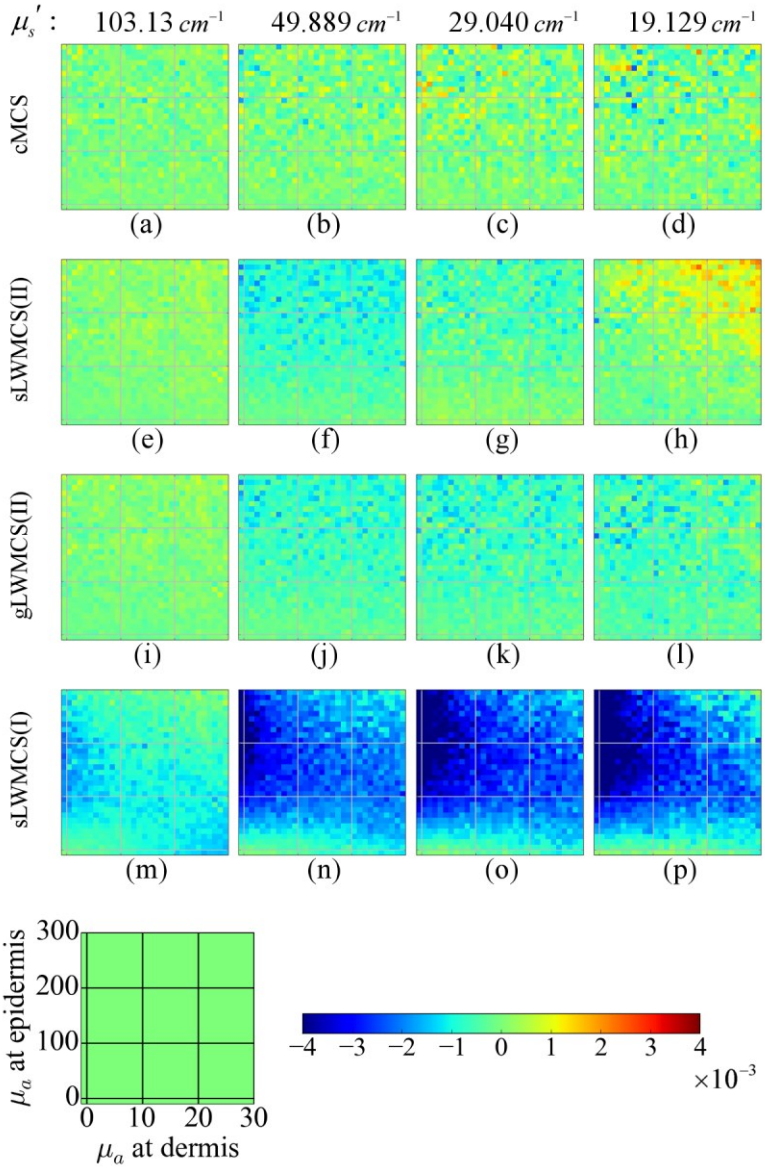

Fig. 6-6 E of (a)-(d): cMCS; (e)-(h): sLWMCS(II); (i)-(l): gLWMCS(II); (m)-(p): sLWMCS(I). For each row, from left to light, μ_s' varies as the values indicated on top of the picture, which are the values at 400, 500, 600, and 700 nm in our skin model. Horizontal and vertical axes are μ_a for the dermis and epidermis, respectively, and the specific values of each axes are shown at the bottom left. The correlation between E and the color is shown as a color bar at the bottom right. The unit of μ_s' and μ_a is cm^{-1}.

Table 6-1 The average and standard deviation of E ($\times 10^{-3}$) for each method at each wavelength.

$\mu s'$ (cm^{-1}) / MCS	103.13 (at 400nm)	49.889 (at 500nm)	29.040 (at 600nm)	19.129 (at 700nm)	time/spectrum (31 point)
cMCS	0.01 ±3.22	-0.17 ±4.30	0.33 ±5.15	-0.32 ±5.68	1531 sec.
sLWMCS(II)	0.91 ±2.48	-6.26 ±3.88	-2.87 ±4.16	2.46 ±5.65	3 sec.
gLWMCS(II)	0.13 ±2.48	-5.47 ±3.50	-5.43 ±3.88	-4.77 ±4.16	5 sec.
sLWMCS(I)	-8.84 ±4.29	-19.98 ±8.47	-23.92 ±11.28	-23.32 ±13.76	-

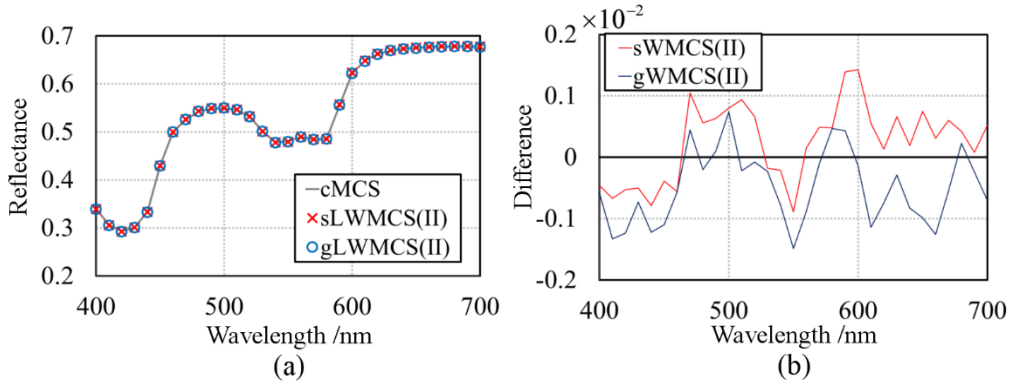

Fig. 6-7 Calculated reflectance spectrum of the skin model used in the methods. The concentrations of melanin, oxygenated hemoglobin, and deoxygenated hemoglobin were set to 1%, 0.1%, and 0.1%, respectively. (a) Reflectance spectrum of cMCS: gray solid line; sLWMCS(II): red cross; and gLWMCS(II): blue circle. (b) Difference between cMCS and sLWMCS(II): red line; difference between cMCS and gLWMCS(II): blue line.

6.4.2. Estimating chromophore concentrations from the spectrum

The results are summarized in Table 6-2. With the sLWMCS(II), the estimated concentrations of melanin, oxygenated hemoglobin, and deoxygenated hemoglobin were 1.005%, 0.099% and 0.100%, respectively, for the spectrum from the cMCS with the concentrations of 1%, 0.1%, and 0.1%, respectively. The evaluation function was calculated with 186 iterations, and the total processing time was 633 sec. The processing time in phase 3 was 471 sec., which is about three times longer than the processing time for phase 4, which was 158 sec. The processing time of phase 2 was less than 1 sec.

Table 6-2 The results of estimating the chromophore concentration.

		sLWMCS(II)	gLWMCS(II)
Estimated concentration			
	Melanin (1 %)	1.005 %	0.997 %
	Oxyhemoglobin (0.1 %)	0.099 %	0.101 %
	Deoxyhemoglobin (0.1 %)	0.100 %	0.099 %
Processing time			
	Phase 3	471 sec.	825 sec.
	Phase 4	158 sec.	158 sec.
	Total	633 sec.	984 sec.
Iteration		186 times	174 times

With the gLWMCS(II), the estimated concentrations of melanin, oxygenated hemoglobin, and deoxygenated hemoglobin were 0.997%, 0.101%, and 0.099%, respectively, for the same spectrum that was used for the sLWMCS(II). The evaluation function was calculated with 174 iterations, and the total processing time was 984 sec. The processing time in phase 3 was 825 sec., which was about five times longer than the processing time for phase 4, which was 158 sec.

6.5. Discussion

As can be seen in Fig. 6-6 and Table 6-1, the values of the E of the sLWMCS(II) and gLWMCS(II) were less than 1% across the values of μ_s' and μ_a that are included in the range of actual human skin, from light to moderately pigmented [93]. This shows that we achieved our aim of quickly obtaining results that are in good agreement with those

of the cMCS. The standard deviations of these methods were smaller than that of the cMCS. This means that the statistical errors in the sLWMCS(II) and the gLWMCS(II) are smaller than that of the cMCS, when the same number of photons are used. In the MCS, the reflectance is calculated stochastically, and so statistical errors result from the finite number of photons. In the LWMCSs, the MCS was executed for each layer and for each incident angle, and so the total number of photons was much larger than it was in the cMCS. On the other hand, the average of the values of E from the LWMCSs was larger than that of the cMCS, which is probably due to the discretization error in the path length and the angles in both the sLWMCS(II) and gLWMCS(II). The errors of the sLWMCS(II) are close to those of the gLWMCS(II). This means ξ was successfully estimated by interpolation. The value of σ in the gLWMCS(II) also seems to be appropriate, based on a comparison of the errors of the gLWMCS(II) and the sLWMCS(II). Comparing the results of the sLWMCS(II) with those of the sLWMCS(I), we see that dual partitioning was better than single partitioning. These results indicate that in binning I, the changes in the bin width with the path length were not adequate.

The calculation of the sLWMCS(II) and gLWMCS(II) were two orders of magnitude faster than that of the cMCS. The calculation time will become even shorter if the latest MATLAB is used without an emulator. It is worth noting that the processing times of these methods will not be affected by the number of photons, the absorption coefficient, or the reduced scattering coefficient. The processing time of phase 1 varies with these parameters, but phase 1 is only calculated once, and so this will not affect the time of phases 2 to 4.

The time to calculate the reflectance was sufficiently short that the chromophore concentrations could be successfully estimated by solving an optimization problem.

The calculation time of the estimation was about ten to twenty minutes in the environment we used; this is comparable to that for a single spectrum estimation with a cMCS. This may be acceptable for estimating chromophore concentrations, and it is better than the several days required for doing this with the cMCS, which has a processing time that is 300 times longer than that of the gLWMCS. The spectrum estimated by the optimization problem can be nearly identical to the input spectrum, which may be one of the reasons that the estimate had such good precision. Before using this method with measured spectrums, it is important to evaluate its robustness against errors, e.g., to evaluate the difference between the skin model and actual skin.

The OPLM [78] was also developed in order to quickly derive the reflectance with values identical to those obtained from a cMCS of a multilayered model. However, the gLWMCS has apparent advantages over the OPLM in terms of the ease with which the structure of the model can be changed. With the OPLM, if there are any changes in the parameters or the number of layers, the baseline data must be recalculated. The gLWMCS, however, allows us to alter the μ_s', thickness, or refractive index of any layer, or to add more layers, without the need to recalculate the baseline data. In terms of calculation time, we note that for the OPLM, the number of dimensions of the path length matrix increases if we expand the number of layers. This causes the computational cost to increase exponentially. With the gLWMCS, the additional calculations are only required for creating the transition matrices and for combining the additional layer with the other layers, so the computational cost only increases linearly with the number of layers. According to a study of the OPLM [78], the errors were larger than those of the sLWMCS(II) and gLWMCS(II), especially for longer wavelengths [78]. However, this

is probably due to the equal divisions in the binning of the path length, and we assume it would be improved if the binning were optimized.

For some applications, such as imaging, the calculation time is still too long. Since most of this is due to arithmetic operations on matrices in phases 3 and 4, the time could be shortened by reducing the size of the matrices. However, if this is done by simply decreasing the number of bins in the path length histograms, the accuracy will deteriorate. Optimizing the binning strategy (i.e., finding a better binning strategy than equal logarithmic widths with dual partitioning) will be effective for improving both the calculation time and the accuracy. The incident and exit angles were discretized with equal angle intervals, but other methods, such as equal cosine intervals [120], could be considered as possible alternatives to maximize the performance. Increasing the number of photons in the MCS will improve the error; it will lengthen the precalculation (phase 1), but not the subsequent calculations (phases 2 to 4). When estimating the chromophore concentration, the initial values affect the number of iterations required. We intentionally set the starting values far from the actual values to demonstrate the robustness of the methods. However, if we determine appropriate starting values by using an approximation method, such as a diffusion model, the iteration count, and therefore the processing time, will be reduced. In addition, we could use fewer than 31 wavelengths, and the method used for interpolation could be improved. In the gLWMCS, the transition matrices are calculated twice for each layer (for Ξ_+ and Ξ_-), but they are only calculated once in the sLWMCS. This is the primary reason for the difference in their processing times. If the transition matrices could be interpolated at step 2, then they would not need to be calculated twice. Upgrading the computer

hardware and software would also reduce the calculation time, since the environment we used was not the best currently available.

The selection of the Ξ_i could also affect the accuracy of the calculation. A narrower interval of the Ξ_i will enlarge the amount of baseline data and lengthen the time to complete phase 1, but it will improve the results. In optimizing the interval of the Ξ_i, the dominant type of scattering should be taken into account. For low Ξ_i, single scattering is dominant, while multiple scattering is dominant for high Ξ_i. In the intermediate region, the linear interpolation error is expected to become larger due to the phase transition. Therefore, for the most accurate calculations of reflectance and transmittance, the interval of the Ξ_i in the intermediate region should be smaller than those of the other regions.

This method inherits the following limitations from the AD method [120]. It cannot be used for time-domain analysis, and it cannot derive the reflectance as a function of the distance from the incident point. The model is limited to a homogeneous multilayer model in which the interfaces are parallel and infinite, and each layer must have uniform scattering and absorption properties, and a uniform refractive index. Either or both the incident light or the detected light must be axially symmetric. However, if we limit the model to the condition that g=0, as in the skin model we used, the method may be adapted to a nonsymmetric condition by separate treatment of scattered light and nonscattered light. This works because once the light has been scattered, the direction is independent of the azimuthal angle of the incident light.

This method also inherits benefits of the AD method [120], as follows. The characteristics of the scattering properties of each layer are derived separately, which is a remarkable characteristic and enables a physical interpretation of the results.

In real cases, the thickness of the layers and the other structural attributes of actual skin are not exactly the same as in the skin model that we used. We also did not consider polarization, although, according to Fresnel's law, transmitted and reflected light are partially polarized, and this affects reflectance. These will cause discrepancies between the results with the model and those with actual skin. The effect of polarization may be implemented in the method by modeling the transition between parallel and perpendicular polarization. In our model, g was approximated as zero, and we only varied μ_s' to model the scattering characteristics. The asymmetry factor can be set to a more appropriate value. If we wish to consider varying the anisotropy, the base transition matrices can be precalculated for various values of the anisotropy coefficient, in addition to various values of μ_s'. In this case, the calculation time will increase since the interpolation will become two dimensional.

6.6. Conclusion

We developed a method to quickly derive results equivalent to those of the cMCS for the calculation of reflectance from a layered medium and with a broad range of applicable parameters. Once the baseline data set is prepared, it can be applied to various multilayer models, including human skin. The difference between the reflectance calculated by our method and that of the cMCS was about 0.1% over the range of μ_s' and μ_a of light to moderately pigmented skin. In addition, we successfully used the method to estimate the chromophore concentration from a spectrum; this required iterative calculations of the reflectance. We expect that this method can substitute for the cMCS when the total amount of reflection is the concern. With this fast and accurate method, the parameters to be fit in the inverse problem can include the thickness and the reduced

scattering coefficient, which are usually assumed to be constant due to limitations in computation time and resources. We discussed ways in which the processing time can be further shortened while still maintaining accuracy, and this should be further studied in future work.

7. Concluding remarks

In the dissertation, we aimed at getting higher-level information of skin from internal diffuse reflection.

In Chapter 2, as fundamental knowledge, the structure of human skin and behavior of light are described. Section 2.1 and 2.2 described the structure of human skin, and the basic knowledge of classical optics, respectively, in relation to this dissertation.

In Chapter 3, to quantitatively evaluate skin chromophores over a wide region of curved skin surface, we propose an approach that suppresses the effect of the shading-derived error in the reflectance on the estimation of chromophore concentrations, without sacrificing the accuracy of that estimation. In our method, we use multiple regression analysis, assuming the absorbance spectrum as the response variable and the extinction coefficients of melanin, oxygenated hemoglobin, and deoxygenated hemoglobin as the predictor variables. The concentrations of melanin and total hemoglobin are determined from the multiple regression coefficients using compensation formulae based on the diffuse reflectance spectra derived from a Monte Carlo simulation. To suppress the shading-derived error, we investigated three different combinations of multiple regression coefficients for the compensation formulae. *In vivo* measurements with the forearm skin demonstrated that the proposed approach can reduce the estimation errors that are due to shading-derived errors in the reflectance. With the best combination of multiple

regression coefficients, we estimated that the ratio of the error to the chromophore concentrations is about 10%. The proposed method does not require any measurements or assumptions about the shape of the subjects; this is an advantage over other studies related to the reduction of shading-derived errors.

In Chapter 4, we adapted the critical angle method for measuring rough surfaces under partial contact to acquire *in vivo* skin refractive index (RI). Assuming that the total reflection is the simple sum of reflection from areas that are in contact and reflection from those that are out of contact, the RI can be estimated even for partial contact with a rough surface. We found that cheek skin is sufficiently soft that a large enough area can be in contact and that the critical angle was detectable. The RIs of the cheeks of adult females were measured. The RI range was about 1.51–1.53 at a wavelength of 550 nm without considering systematic errors. The RIs of cheeks are significantly correlated with the conductance, which corresponds to the water content. We determined the relationship between the RI and conductance within the variation of skin under normal conditions; this relationship has been theoretically obtained in previous studies. In the present study, a direct *in vivo* measurement method was developed that enables us to measure the RI in daily life, although this method contains errors including effects due to disregarding absorption.

In Chapter 5, we have developed a simple and effective method for everyday measurement of translucency with a handy spectral reflectometer using edge-loss. Edge-loss can be used to quantify translucency index in terms of changes in reflectance under two types of measurement conditions. Here, a measurement condition represents the pairing of an illumination area and a measurement area. As a measure of the degree of lateral spread of reflected light, translucency index can influence the appearance of

human skin, as this index represents eventual translucency. First, we estimated how edge-loss changes when measurement conditions are varied. We then selected the combination of two measurement conditions of large edge-loss and small edge-loss to minimize errors. Finally, we estimated actual skin translucency changes before and after treatments comprising acetone-ether immersion and ultraviolet irradiation. The results were qualitatively consistent with the expectations under variations in absorbance and scattering capacity, indicating the effectiveness of this method in evaluating translucency. This method allows simultaneous measurement of translucency and reflectance as a spectrum, and also appears applicable for daily use, although common optical parameters cannot be derived using this method alone.

In Chapter 6, to rapidly derive a result for diffuse reflectance from a multilayered model that is equivalent to that of a Monte-Carlo simulation (MCS), we propose a combination of a layered white MCS and the adding-doubling method. For slabs with various scattering properties and without absorption, we calculate the transition matrices for light flow with respect to the incident and exit angles. From this series of precalculated transition matrices, we can calculate the transition matrices for an arbitrary multilayer model. The relative errors of the results of this method compared to a conventional MCS were about 0.1%. We successfully used this method to estimate the chromophore concentration from the reflectance spectrum of a numerical model of skin.

With those newly developed method, precise estimation become possible in the quantitative evaluation for functions and appearance of human skin tissue using reflectance spectroscopy. The imaging of chromophore concentrations (Chapter 4) still has problems, e.g. artifact of blood vessels in melanin images, which should be removed.

In solving the problem, improvement of skin model will be required. The method for short-time calculation of MCS will become a powerful tool for solving the problems.

Acknowledgement

I would like to express my gratitude to Professor T. Iwai and Associate Professor I. Nishidate for their valuable instruction and useful suggestions on all of the present work. My hearty thanks are also extend to M. Miyaki, N. Komeda, K. Ohkubo, N. Ojima and K. Iwata of Kao Corporation for useful discussions and advice.

For the study described in Chapter 4, I wish to express my gratitude to Kotatsu Bito of Kao corporation for providing the RI measurement of silicone samples with the dipping method and to the staff of Lightwave Technology Lab. in Faculty of Systems Engineering, Wakayama Univ., including Dr. Eiji Nitanai, for demonstrating their equipment to us, which provided useful insights for developing our system.

For the study described in Chapter 5, I wish to express my gratitude to Takanori Igarashi in Kao Corporation for collaborating in the implementation of experiments during the initial trial-and-error phase of this study, and to Koji Ohkubo and Takashi Kawata in Kao Corporation for providing extremely helpful support for the experiments involving A/E treatment and UV-induced erythema, respectively.

Thanks are also due to other members of the Graduate school of bio-applications and systems engineering, Tokyo University of Agriculture and Technology, for various supports with which the present dissertation has been successfully accomplished.

References

[1] S. Chandrasekhar: Radiative Transfer. Dover, New York,1960

[2] A. Ishimaru, "Diffusion of a pulse in densely distributed scatterers," *Journal of the Optical Society of America* **68**, 1045-1050 (1978).

[3] K. Furutsu, "On the diffusion equation derived from the space-time transport equation," *Journal of the Optical Society of America* **70**, 360-366 (1980).

[4] S.A. Prahl, M. Keijzer, S.L. Jacques, A.J. Welch, "A Monte Carlo model of light propergation in tissue," *SPIE Institute Series* **IS5**, 102-111 (1989).

[5] L.H. Wang, S.L. Jacques, L.Q. Zheng, "MCML - Monte Carlo modeling of light transport in multi-layered tissues," *Comput Methods Programs Biomed* **47**(2), 131-146 (1995).

[6] R. Arridge, M. Cope, DelpyDT, "The theoretical basis for the determination of optical pathlengths in tissue: temporal and frequency analysis," *Physics in medicine and biology* **37**, 1531-1560 (1992).

[7] B. Chance, J.S. Leigh, H. Miyake, D.S. Smith, S. Nioka, R. Greenfeld, M. Finander, K. Kaufmann, W. Levy, M. Young, "Comparison of time-resolved and -unresolved measurements of deoxyhemoglobin in brain," *Proc Natl Acad Sci U S A* **85**(14), 4971-4975 (1988).

[8] D.T. Delpy, M. Cope, der Zee P. van, S.R. Arridge, S. Wray, J. Wyatt, "Estimation of optical pathlength through tissue from direct time of flight measurement," *Physics in medicine and biology* **33**, 1433-1442 (1988).

[9] B. Wilson, Y. Park, Y. Hefetz, M. Patterson, S. Madsen, S. Jacques, "The potential of time-resolved reflectance measurements for noninvasive determination of tissue optical properties," *Proc Soc Phot-Opt Instrum Eng* **1064**, 97-106 (1989).

[10] Y. Nomura, O. Hazeki, M. Tamura, "Exponential attenuation of light along nonlinear path through the biological model," *Advances in experimental medicine and biology* **248**, 77-80 (1989).

[11] M.S. Patterson, B. Chance, B.C. Wilson, "Time resolved reflectance and transmittance for the non-invasive measurement of tissue optical properties," *Applied optics* **28**, 2331-2336 (1989).

[12] Y. Hasegawa, Y. Yamada, M. Tamura, Y. Nomura, "Monte Carlo simulation of light transmission through living tissues," *Applied optics* **30**(), 4515-4520 (1991).

[13] S.L. Jacques, "Time resolved propagation of ultrashort laser pulses within turbid tissues," *Applied optics* **28**, 2223-2229 (1989).

[14] R.A.J. Groenhuis, H.A. Ferwerda, J.J.T. Bosch, "Scattering and absorption of turbid materials determined from reflection measurements. 1: Theory," *Appl Opt* **22**(16), 2456-2462 (1983).

[15] R.A.J. Groenhuis, J.J.T. Bosch, H.A. Frewerda, "Scattering and absorption of turbid materials determined from reflection measurements. 2: Measuring method and calibration," *Applied optics* **22**, 2463-2467 (1983).

[16] J.M. Schmitt, G.X. Zhou, E.C. Walker, R.T. Wall, "Multilayer model of photon diffusion in skin," *Journal of the Optical Society of America* **A7**, 2141-2153 (1990).

[17] B.C. Wilson, T.J. Farrell, M.S. Patterson, "An optical fiber-based diffuse reflectance spectrometer for non-invasive investigation of photodynamic sensitizers in vivo," *Proc SPIE* **IS6**, 319-231 (1990).

[18] T.J. Farrell, M.S. Patterson, B. Wilson, "A diffusion theory model of spatially resolved, steady-state diffuse reflectance for the noninvasive determination of tissue optical properties *in vivo*," *Med Phys* **19**(4), 879-888 (1992).

[19] R.A. Bolt, Bosch J.J. ten, "Measuring position-dependent volume reflection," *Applied optics* **32**, 4641-4645 (1993).

[20] R.A. Bolt, Bosch J.J. ten, "On the determination of optical parameters for turbid materials," *Wave Random Media* **4**, 233-242 (1994).

[21] S.L. Jacques, A. Gutsche, J. Schwartz, L. Wang, F.K. Tittel: Video reflectometry to specify optical properties of tissue *in vivo*. SPIE Optical Engineering Press, Bellingham, WA 211-226,1993

[22] R. Splinter, G.A. Nanney, L. Littmann, C.H. Chuang, R.H. Svenson, J.R. Tuntelder, "Monitoring tissue optical characteristics in situ using a CCD camera," *Laser Life Sci* **6**, 15-25 (1994).

[23] M. Dogariu, T. Asakura, "Reflectance properties of finite-size turbid media," *Waves Random Media* **4**, 429-439 (1994).

[24] A. Kienle, L. Lilge, M.S. Patterson, R. Hibst, R. Steiner, B.C. Wilson, "Spatially resolved absolute diffuse reflectance measurements for noninvasive determination of the optical scattering and absorption coefficients of biological tissue," *Applied optics* **35**, 2304-2314 (1996).

[25] B.L. Diffey, R.J. Oliver, P.M. Farr, "A portable instrument for quantifying erythema induced by ultraviolet radiation," *Br J Dermatol* **111**, 663-672 (1984).

[26] J.B. Dawson, D.J. Barker, D.J. Ellis, E. Grassam, J.A. Cotterill, G.W. Fisher, J.W. Feather, "A theoretical and experimental study of light absorption and scattering by in vivo skin," *Phys Med Biol* **25**(4), 695-709 (1980).

[27] D.K. Harrison, S.D. Evans, N.C. Abbot, J.S. Beck, P.T. McCollum, "Spectrophotometric measurements of haemoglobin saturation and concentration in skin during the tuberculin reaction in normal human subjects," *Clin Phys Physiol Meas* **13**(4), 349-363 (1992).

[28] R. Marchesini, M. Brambilla, C. Clemente, M. Maniezzo, A.E. Sichirollo, A. Testory, D.R. Venturoli, N. Cascinelli, "In vivo spectrophotometric evaluation of neoplastic and non-neoplastic skin pigmented lesions-I.Reflectance measurement," *Photochemistry and photobiology* **53**, 77-84 (1991).

[29] R. Marchesini, N. Cascinelli, M. Brambilla, C. Clemente, L. Mascheroni, E. Pignoli, A. Testori, D.R. Venturoli, "In vivo spectrophotometric evaluation of neoplastic and non-neoplastic skin pigmented lesions-II. Discriminant analysis between nevus and melanoma," *Photochemistry and photobiology* **55**, 515-522 (1992).

[30] V.P. Wallace, D.C. Crawford, P.S. Mortimer, R.J. Ott, C.B. Bamber, "Spectrophotometric assessment of pigmented skin lesion: methods and feature selection for evaluation of diagnostic performance," *Physics in medicine and biology* **45**, 735-751 (2000).

[31] M. Shimada, Y. Masuda, Y. Yamada, M. Itoh, M. Takahashi, T. Yatagai, "Explanation of human skin color by multiple linear regression analysis based on the modified Lambert-Beer law," *Optical Review* **7**(4), 348-352 (2000).

[32] M. Shimada, Y. Yamada, M. Itoh, T. Yatagai, "Melanin and blood concentration in human skin studied by multiple regression analysis: experiments," *Phys Med Biol* **46**, 2385-2395 (2001).

[33] M. Shimada, Y. Yamada, M. Itoh, T. Yatagai, "Melanin and blood concentration in human skin studied by multiple regression analysis: assessment by Monte Carlo simulations," *Physics in medicine and biology* **46**, 2397-2406 (2001).

[34] N. Tsumura, H. Haneishi, Y. Miyake, "Independent-component analysis of skin color image," *Journal of the Optical Society of America* **A16**, 2169-2176 (1999).

[35] K. Uludag, M. Kohl, J. Steinbrink, H. Obrig, A. Villringer, "Cross talk in the Lambert-Beer calculation for near-infrared wavelengths estimated by Monte Carlo simulations," *J Biomed Opt* **7**(1), 51-59 (2002).

[36] N. Okui, E. Okada, "Wavelength dependence of crosstalk in dual-wavelength measurement of oxy- and deoxy-hemoglobin," *J Biomed Opt* **10**(1), 011015 (2005).

[37] J.M. Kainerstorfer, F. Amyot, M. Ehler, M. Hassan, S.G. Demos, V. Chernomordik, C.K. Hitzenberger, A.H. Gandjbakhche, J.D. Riley, "Direct curvature correction for noncontact imaging modalities applied to multispectral imaging," *Journal of biomedical optics* **15**(4), 046013 (2010).

[38] E. Claridge, S. Cotton, P. Hall, M. Moncrieff, "From colour to tissue histology: physics-based interpretation of images of pigmented skin lesions," *Medical Image Analysis* **7**(4), 489-502 (2003).

[39] S. Prigent, X. Descombes, D. Zugaj, P. Martel, J. Zerubia, "Multi-spectral image analysis for skin pigmentation classification," *Image Processing (ICIP) , 2010 17th IEEE International Conference on, Hong Kong*, 3641-3644 (2010).

[40] I. Nishidate, Y. Aizu, H. Mishina, "Estimation of melanin and hemoglobin in skin tissue using multiple regression analysis aided by Monte Carlo simulation," *J Biomed Opt* **9**(4), 700-710 (2004).

[41] I. Nishidate, A. Wiswadarma, Y. Hase, N. Tanaka, T. Maeda, K. Niizeki, Y. Aizu, "Noninvasive spectral imaging of skin chromophores based on multiple regression analysis aided by Monte Carlo simulation," *Opt Lett* **36**(16), 3239-3241 (2011).

[42] N. Tsumura, N. Ojima, K. Sato, M. Shiraishi, H. Shimizu, H. Nabeshima, S. Akazaki, K. Hori, Y. Miyake, "Image-based skin color and texture analysis/synthesis by extracting hemoglobin and melanin information in the skin," *ACM Transactions on Graphics 22* **(3)**(Proceedings of ACM SIGGRAPH 2003), 770-779 (2003).

[43] J. Sun, M. Smith, "Multidimensional imaging for skin tissue surface characterization," *Computers in industry* **64**(9), 1383-1389 (2013).

[44] T.T.A. Nguyen, H.N.D. Le, M. Vo, Z. Wang, L. Luu, J.C. Ramella-Roman, "Three-dimensional phantoms for curvature correction in spatial frequency domain imaging," *Biomedical optics express* **3**(6), 1200-1214 (2012).

[45] T. Sand, T. Gambichler, G. Moussa, F.G. Bechara, D. Sand, P. Altmeyer, K. Hoffmann, "Evaluation of the epidermal refractive index measured by optical coherence tomography," *Skin Res Technol* **12**(2), 114-118 (2005).

[46] G.J. Tearney, M.E. Brezinsky, J.F. Southern, B.E. Bouma, M.R. Hee, J.G. Fujimoto, "Determination of the refractive index of highly scattering human tissue by optical coherence tomography," *Opt Lett* **20**(21), 2258-2260 (1995).

[47] J.J.J. Dirckx, L.C. Kuypers, W.F. Decraemer, "Refractive index of tissue measured with confocal microscopy," *J Biomed Opt* **10**(4), 044014 (2005).

[48] Q.W. Song, C.Y. Ku, C. Zhang, R.B. Gross, R.R. Birge, R. Michalak, "Modified critical angle method for measuring the refractive index of bio-optical materials and its application to bacteriorhodopsin," *J Opt Soc Am B* **12**(5), 797-803 (1995).

[49] W. Leupacher, A. Penzkofer, "Refractive-index measurement of absorbing condensed media," *Appl Opt* **23**(10), 1554-1558 (1984).

[50] H. Li, S. Xie, "Measurement method of the refractive index of biotissue by total internal reflection," *Appl Opt* **35**(10), 1793-1795 (1996).

[51] J. Lai, Z. Li, C. Wang, A. He, "Experimental measurement of the refractive index of biological tissues by total internal reflection," *Appl Opt* **44**(10), 1845-1849 (2005).

[52] J.C. Lai, Y.Y. Zhang, Z.H. Li, H.J. Jiang, A.Z. He, "Complex refractive index measurement of biological tissues by attenuated total reflection ellipsometry," *Appl Opt* **49**(16), 3235-3238 (2010).

[53] H. Ding, J.Q. Lu, K.M. Jacobs, X.H. Hu, "Determination of refractive indices of porcine skin tissues and Intralipid at eight wavelengths between 325 and 1557 nm," *J Opt Soc Am A* **22**(6), 1151-1157 (2005).

[54] H. Ding, J.Q. Lu, W.A. Wooden, P.J. Kragel, X.H. Hu, "Refractive indices of human skin tissues at eight wavelengths and estimated dispersion relations between 300 and 1600 nm," *Phys Med Biol* **51**(6), 1479-1489 (2006).

[55] P.J. Caspers, G.W. Lucassen, E.A. Carter, H.A. Bruining, G.J. Puppels, "*In vivo* confocal Raman microspectroscopy of the skin: noninvasive determination of molecular concentration profiles," *J Invest Dermatol* **116**(3), 434-442 (2001).

[56] T. Richter, C. Peuckert, M. Sattler, K. Koenig, I. Riemann, U. Hintze, K.P. Wittern, R. Wiesendanger, R. Wepf, "Dead but highly dynamic - the stratum

corneum is divided into three hydration zones," *Skin Pharmacol Physiol* **17**(5), 246-257 (2004).

[57] G. Ackermann, M. Hartmann, K. Scherer, E.W. Lang, U. Hohenleutner, M. Landthaler, W. Bäumler, "Correlations between light penetration into skin and the therapeutic outcome following laser therapy of port-wine stains," *Lasers Med Sci* **17**(2), 70-78 (2002).

[58] J.L. Solan, K. Laden, "Factors affecting the penetration of light through stratum corneum," *J Soc Cosmet Chem* **28**(3), 125-137 (1977).

[59] R.R. Anderson, J.A. Parrish, "The optics of human skin," *J Invest Dermatol* **77**(1), 13-19 (1981).

[60] K. Hashimoto, "New methods for surface ultrastructure: comparative studies of scanning electron microscopy, transmission electron microscopy and replica method," *Int J Dermatol* **13**(6), 357-381 (1974).

[61] V. Tsenova, E. Stoykova, "Refractive index measurement in human tissue samples," *Proc SPIE* **5226**, 413-417 (2003).

[62] L. Wang, S.L. Jacques, "Use of a laser beam with an oblique angle of incidence to measure the reduced scattering coefficient of a turbid medium," *Appl Opt* **34**(13), 2362-2366 (1995).

[63] T. Nakai, G. Nishimura, K. Yamamoto, M. Tamura, "Expression of optical diffusion coefficient in high-absorption turbid media," *Phys Med Biol* **42**(12), 2541-2549 (1997).

[64] N. Komeda, N. Ojima, K. Okuzumi, J. Okada, K. Fukuda, K. Hori, "Analysis of skin appearance based internal scattering of light," *18th IFSCC International Conference Proceedings*, *Florence*, *Italy*, 201-207 (2005).

[65] A. Matsubara, "Skin translucency: what is it and how is it measured?," *24th IFSCC Congress Abstracts (Oral Session)*, *Osaka*, *Japan*, 92-93 (2006).

[66] T. Weyrich, W. Matusik, H. Pfister, B. Bickel, C. Donner, C. Tu, J. McAndless, J. Lee, A. Ngan, H.W. Jensen, M. Gross, "Analysis of human faces using a measurement-based skin reflectance model," *ACM Transactions on Graphics (TOG) - Proceedings of ACM SIGGRAPH 2006* **25**(3), 1013-1024 (2006).

[67] H.W. Jensen, S.R. Marschner, M. Levoy, P. Hanrahan, "A practical model for subsurface light transport," *International Conference on Computer Graphics and Interactive Techniques;Proceedings of the 28th annual conference on Computer graphics and interactive techniques*, 511-518 (2001).

[68] W.F. Cheong, S.A. Prahl, A.J. Welch, "A review of the optical properties of biological tissues," *IEEE Journal of Quantum Electronics* **26**(12), 2166-2185 (1990).

[69] S. Nickell, M. Hermann, M. Essenpreis, T.J. Farrell, U. Kramer, M.S. Patterson, "Anisotropy of light propagation in human skin," *Phys Med Biol* **45**, 2873-2886 (2000).

[70] Z.X. Jiang, P.D. Kaplan, "Point-spread imaging for measurement of skin translucency and scattering," *Skin Res Technol* **14**, 293-297 (2008).

[71] S.H. Tseng, P. Bargo, A. Durkin, N. Kollias, "Chromophore concentrations, absorption and scattering properties of human skin in-vivo," *Opt Express* **17**(17), 14599-14617 (2009).

[72] R.H. Wilson, K. Vishwanath, M.A. Mycek, "Combined Monte Carlo and path-integral method for simulated library of time-resolved reflectance curves from layered tissue models," *Proc. of SPIE* **Vol.7175**, 717518 (2009).

[73] M.G. Nichols, E.L. Hull, T.H. Foster, "Design and testing of a white-light, steady-state diffuse reflectance spectrometer for determination of optical properties of highly scattering systems," *Appl Opt* **36**(1), 93-104 (1997).

[74] D. Yudovsky, A.J. Durkin, "Hybrid diffusion and two-flux approximation for multilayered tissue light propagation modeling," *Applied optics* **50**(21), 4237-4245 (2011).

[75] E. Alerstam, S. Andersson-Engels, T. Svensson, "White Monte Carlo for time-resolved photon migration," *J Biomed Opt* **13**(4), 04304 (2008).

[76] A. Pifferi, P. Taroni, G. Valentini, S. Anderson-Engels, "Real-time method for fitting time-resolved reflectance and transmittance measurements with a Monte Carlo model," *Appl Opt* **37**(13), 2774-2780 (1998).

[77] A. Kienle, M.S. Patterson, "Determination of the optical properties of turbid media from a single Monte Carlo simulation," *Phys Med Biol* **41**, 2221-2227 (1996).

[78] S. Yamamoto, I. Fujiwara, M. Yamauchi, N. Tsumura, K. Ogawa-Ochiai, "Optical path-length matrix method for estimating skin spectrum," *Optical Review* **19**(6), 361-365 (2012).

[79] M. Martinelli, A. Gardner, D. Cuccia, C. Hayakawa, J. Spanier, V. Venugopalan, "Analysis of single Monte Carlo methods for prediction of reflectance from turbid media," *Opt Express* **19**(20), 19627 (2011).

[80] A. Sassaroli, C. Blumettti, F. Martelli, L. Alianelli, D. Contini, A. Ismaelli, G. Zaccanti, "Monte Carlo procedure for investigating light propagation and imaging of highly scattering media," *Appl Opt* **37**(31), 7392-7400 (1998).

[81] H. Shimizu, "Textbook of modern dermatology 2nd edtion (*Atarashii Hifu Kagaku*)," Nakayama Shoten, 2011 [in Japanese]

[82] S. Yamazaki and K. Goto, "*Shoukai Denjikigaku Enshuu*," Kyoritsu Shuppan Co. Ltd., 1970 [in Japanese]

[83] P. Chylek, G. Videen, D.J.W. Geldart, J.S. Dobbie, H.C.W. Tso, "Effective medium approximations for heterogeneous particles," *Academic Press, San Diego*, (2000).

[84] K. Yoshida, M. Miyaki, N. Ojima, K. Iwata, "Relationship between microstructure of the skin surface and surface reflection based on geometric optics," *J Dermatol Sci* **66**, 225-232 (2012).

[85] S. Kinoshita, "*Seibutsu Nanofotonikusu - Kouzoushoku Nyuumon - Shiriizu Seimei Kinou 1,*" Asakura Shoten, 2010 [in Japanese]

[86] P. Välisuo, I. Kaartinen, V. Tuchin, J. Alander, "New closed-form approximation for skin chromophore mapping," *J Biomed Opt* **16**(4), 046012 (2011).

[87] T. Maeda, N. Arakawa, M. Takahashi, Y. Aizu, "Monte Carlo simulation of spectral reflectance using a multilayered skin tissue model," *Optical Review* **17**(3), 223-229 (2010).

[88] S.L. Jacques, R. Samatham, N. Choudhury, "Rapid spectral analysis for spectral imaging," *Biomedical Optics Express* **1**(1), 157-164 (2010).

[89] S.L. Jacques, D.J. McAuliffe, "The melanosome: threshold temperature for explosive vaporization and internal absorption coefficient during pulsed laser irradiation," *Photochem Photobiol* **53**(6), 769-775 (1991).

[90] S.A. Prahl, "Optical Absorption of Hemoglobin", http://omlc.ogi.edu/spectra/hemoglobin/index.html (1999).

[91] S.L. Jacques: Origins of tissue optical properties in the UVA, Visible, and NIR regions. Optical Society of America (OSA), Washington, DC:364-369,1996

[92] M.J.C. van Gemert, S.L. Jacques, H.J.C.M. Sterenborg, W.M. Star, "Skin optics," *IEEE Trans Biomed Eng* **36**(12), 1146-1154 (1989).

[93] S.L. Jacques, "Skin optics summary," *OMLC news Jan 1998*, (1998).

[94] I. Nishidate, Y. Aizu, H. Mishina, "Estimation of Absorbing Components in a Local Layer Embedded in the Turbid Media on the Basis of Visible to Near-Infrared(VIS-NIR) Reflectance Spectra," *Optical Review* **10**(5), 427-435 (2003).

[95] M. Oren, S.K. Nayer, "Generalization of Lambert's Reflectance Model," *SIGGRAPH '94 Proceedings of the 21st annual conference on Computer graphics and interactive techniques*, 239-246 (1994).

[96] T. Frost, C. Hohberg, E. Tarakci, S. Forst, P. Kann, A. Pfützner, "Reliability of lightguide spectrophotometry (O2C®) for the investigation of skin tissue microvascular blood flow and tissue oxygen supply in diabetic and nondiabetic subjects," *Journal of Diabetes Science and Technology* **2**(6), 1151-1156 (2008).

[97] B. Jung, B. Choi, A.J. Durkin, K.M. Kelly, J.S. Nelson, "Characterization of port wine stain skin erythema and melanin content using cross-polarized diffuse reflectance imaging," *Lasers in surgery and medicine* **34**(2), 174-181 (2004).

[98] N. Ojima, S. Akazaki, K. Hori, N. Tsumura, Y. Miyake, "Application of image-based skin chromophore analysis to cosmetics," *Journal of Imaging Science And Technology* **48**(3), 222-226,236-238 (2004).

[99] S. Gioux, A. Mazhar, D.J. Cuccia, A.J. Durkin, B.J. Tromberg, J.V. Frangioni, "Three-dimensional surface profile intensity correction for spatially modulated imaging," *Journal of biomedical optics* **14**(3), 034045 (2009).

[100] G.H. Meeten. Refractive Index Measurement. In: J.G. Webster, editors. The Measurement, Instrumentation, and Sensors Handbook Chap. 61. CRC Press, Boca Raton, FL; (1999).

[101] C.W. Blichmann, J. Serup, "Assessment of skin moisture. Measurement of electrical conductance, capacitance and transepidermal water loss," *Acta Derm Venereol* **68**(4), 284-290 (1988).

[102] A.O. Barel, P. Clarys, "In vitro calibration of the capacitance method (Corneometer CM 825) and conductance method (Skicon-200) for the evaluation of the hydration state of the skin," *Skin Res Technol* **3**(2), 107-113 (1997).

[103] T. Miyahara, A. Murai, T. Tanaka, S. Shiozawa, M. Kameyama, "Age-related differences in human skin collagen: solubility in solvent, susceptibility to pepsin digestion, and the spectrum of the solubilized polymeric collagen molecules," *J Gerontol* **37**(6), 651-655 (1982).

[104] M. Egawa, H. Tagami, "Comparison of the depth profiles of water and water-binding substances in the stratum corneum determined *in vivo* by Raman spectroscopy between the cheek and volar forearm skin: effects of age, seasonal changes and artificial forced hydration," *Br J Dermatol* **158**(2), 251-260 (2008).

[105] G.H. Meeten, "Refractive index errors in the critical-angle and the Brewster-angle methods applied to absorbing and heterogeneous materials," *Meas Sci Technol* **8**(7), 728-733 (1997).

[106] L. Salomon, F. DeFornel, J.P. Goudonnet, "Sample-tip coupling efficiencies of the photon-scanning tunneling microscope," *J Opt Soc Am A* **8**(12), 2009-2015 (1991).

[107] R.A. Bolt, Bosch J.J. ten, J.C. Coops, "Influence of window size in small-window colour measurement, particularly of teeth," *Phys Med Biol* **39**(7), 1133-1142 (1994).

[108] H. Takiwaki, Y. Miyaoka, N. Skrebova, H. Kohno, S. Arase, "Skin reflectance-spectra and colour-value dependency on measuring-head aperture area in ordinary reflectance spectrophotometry and tristimulus colourimetry," *Skin Res Technol* **8**(2), 94-97 (2002).

[109] Y.K. Lee, B.S. Lim, C.W. Kim, "Influence of illuminating and viewing aperture size on the color of dental resin composites," *Dent Mater* **20**, 116-123 (2004).

[110] W.M. Johnston, N.S. Hesse, B.K. Davis, R.R. Seghi, "Analysis of edge-losses in reflectance measurements of pigmented maxillofacial elastomer," *J Dent Res* **75**(2), 752-760 (1996).

[111] H. Yanagisawa, A. Ito, M. Nakamura, T. Ohyama, A. Kobayashi, "Application of computer color matching for facial prosthetics. Part II: Translucency of human skin and concentrations of pigments," *Gaku Ganmen Hotei (Maxillofacial Prosthetics)* **19**(1), 54-61 (1996).

[112] E.H. Rugh, W.M. Johnston, N.S. Hesse, "The relationship between elastomer opacity, colorimeter beam size, and measured colorimetric response," *Int J Prosthodont* **4**(6), 569-576 (1991).

[113] J.T. Atkins, Jr. F.W. Billmeyer, "Edge-loss errors in reflectance and transmittance measurement of translucent materials," *Materials Research & Standards* **6**, 564-569 (1966).

[114] Y.K. Lee, H. Lu, J.M. Powers, "Measurement of opalescence of resin composites," *Dent Mater* **21**(11), 1068-1074 (2005).

[115] G. Imokawa, S. Akasaki, A. Kawamata, S. Yano, N. Takaishi, "Water-retaining function in the stratum corneum and its recovery properties by synthetic pseudoceramides," *J Soc Cosmet Chem* **40**, 273-285 (1989).

[116] W. Westerhof, O. Estevez-Uscanga, J. Meens, A. Kammeyer, M. Durocq, "The relation between constitutional skin color and photosensitivity estimated from UV-induced erythema and pigmentation dose-response curves," *J Invest Dermatol* **94**(6), 812-816 (1990).

[117] G.J. Clydesdale, G.W. Dandie, H.K. Muller, "Ultraviolet light induced injury: Immunological and inflammatory effects," *Immunol Cell Biol* **79**, 547-568 (2001).

[118] I. Nishidate, Y. Aizu, H. Mishina, "Estimation of Bluish Appearance of Veins in Skin Tissue Using Spectrocolorimetry," *Optical Review* **9**(6), 269-276 (2002).

[119] H. Takiwaki. "Measurement of erythema and melanin indeces," In: J. Serup, G.B.E. Jemec, G.L. Grove, editors. *Handbook of Non-Invasive Methods and the Skin 2nd Ed*. Chap. 77. *CRC Press*, *Boca Raton*, *FL*: p. 665-671 (1995)

[120] S.A. Prahl, "The Adding-Doubling Method," *Optical-Thermal Response of Laser-Irradiated Tissue*, 101-129 (1995).

List of papers by the author

Peer-reviewed journal

1. K. Yoshida, N. Komeda, N. Ojima, K. Iwata, “Simple and effective method for measuring translucency using edge loss: optimization of measurement conditions and applications for skin”, J Biomed Opt 16:117003. 2011
2. K. Yoshida, M. Miyaki, N. Ojima, K.Iwata, “Relationship between microstructure of the skin surface and surface reflection based on geometric optics”, J Dermatol Sci 66:225-32. 2012
3. K. Yoshida, K. Ohkubo, N. Ojima, K. Iwata, “Application of the critical angle method to refractive index measurement of human skin in vivo under partial contact”, J Biomed Opt 18:037002. 2013
4. K. Yoshida, I. Nishidate, N. Ojima, K. Iwata, “Reduction of shading-derived artifacts in skin chromophore imaging without measurements or assumptions about the shape of the subject”, J Biomed Opt 19:16009. 2014